ADVANCED ENERGY MATERIALS
www.advenergymat.de

The Role of Dimensionality on the Optoelectronic Properties of Oxide and Halide Perovskites, and their Halide Derivatives

Robert L. Z. Hoye, Juanita Hidalgo, Robert A. Jagt, Juan-Pablo Correa-Baena, Thomas Fix,* and Judith L. MacManus-Driscoll**

Halide perovskite semiconductors have risen to prominence in photovoltaics and light-emitting diodes (LEDs), but traditional oxide perovskites, which overcome the stability limitations of their halide counterparts, have also recently witnessed a rise in potential as solar absorbers. One of the many important factors underpinning these developments is an understanding of the role of dimensionality on the optoelectronic properties and, consequently, on the performance of the materials in photovoltaics and LEDs. This review article examines the role of structural and electronic dimensionality, as well as form factor, in oxide and halide perovskites, and in lead-free alternatives to halide perovskites. Insights into how dimensionality influences the band gap, stability, charge-carrier transport, recombination processes and defect tolerance of the materials, and the impact these parameters have on device performance are brought forward. Particular emphasis is placed on carrier/exciton-phonon coupling, which plays a significant role in the materials considered, owing to their soft lattices and composition of heavy elements, and becomes more prominent as dimensionality is reduced. It is finished with a discussion of the implications on the classes of materials future efforts should focus on, as well as the key questions that need to be addressed.

1. Introduction

Perovskite refers to a family of compounds with the chemical formula ABX_3.[1–5] In the perovskite crystal structure, the B-site cation is octahedrally coordinated, and the $[BX_6]^{n-}$ octahedra form a corner-sharing network.[4] Perovskites were first discovered nearly 200 years ago in a chlorite-rich skarn by Gustav Rose, but did not rise to prominence until the 1940s when their suitability for electronic applications was realized.[2] Historically, perovskite research has focused on oxide compounds, such as $CaTiO_3$ (discovered by Rose in 1839 and named after Lev Perovskiy),[2] $BaTiO_3$, $PbTiO_3$, $SrTiO_3$, $BiFeO_3$, and others.[1,2] Beyond these single perovskites, two different A-site cations or B-site cations with different formal charges can be used, giving rise to double perovskites with the formulae $A'A''B_2O_6$ or $A_2B'B''O_6$, respectively. Furthermore, a variety of A- and B-site formal charge combinations can be used, provided they equal to +6 for single oxide perovskites and +12 for double oxide perovskites. There is therefore wide flexibility in the composition of oxide perovskites, and only a fraction of all possible compounds has been synthesized so far.[3] Historically, oxide perovskites have been used in ferroelectric, piezoelectric and pyroelectric applications.[1] They have also found applications in photovoltaics (PVs), but the wide band gap of typical perovskite oxides >2.5 eV has historically limited efficiencies to below 1.25%.[6] More recently, the performance of oxide perovskite solar absorbers was rapidly superseded by lead-halide perovskites (LHPs).[5,7] From an initially reported PV efficiency of 3.8% (using methylammonium lead iodide, or $MAPbI_3$) in 2009,[1,8] LHP photovoltaics have achieved a certified efficiency of 25.5% in 2020.[9,10] The learning rate demonstrated is higher than in other commercialized absorbers,[11] and is due to a variety of factors, including narrow band gaps (e.g., 1.55 eV for $MAPbI_3$),[12] high absorption coefficients $\approx 10^5$ cm^{-1},[13] long diffusion lengths >1 µm,[14] defect tolerance,[15] low Urbach energies,[16] and high photoluminescence quantum efficiencies (PLQEs).[16,17] But while lead-halide perovskites have the advantages of

Dr. R. L. Z. Hoye
Department of Materials
Imperial College London
Exhibition Road, London SW7 2AZ, UK
E-mail: r.hoye@imperial.ac.uk

The ORCID identification number(s) for the author(s) of this article can be found under https://doi.org/10.1002/aenm.202100499.

DOI: 10.1002/aenm.202100499

J. Hidalgo, Prof. J.-P. Correa-Baena
School of Materials Science and Engineering
Georgia Institute of Technology
Atlanta, GA 30332, USA

R. A. Jagt, Prof. J. L. MacManus-Driscoll
Department of Materials Science and Metallurgy
University of Cambridge
27 Charles Babbage Road, Cambridge CB3 0FS, UK
E-mail: jld35@cam.ac.uk

Dr. T. Fix
ICube Laboratory
CNRS and University of Strasbourg
Strasbourg, France
E-mail: tfix@unistra.fr

processability at low temperature (with typical processing temperatures of 100 °C)[10] and exceptional optoelectronic properties, they are limited by their composition of toxic lead and limited environmental and thermal stability without encapsulation.[18] By contrast, oxide perovskites are more environmentally and thermally stable, but require high processing temperatures.[19,20] Recently, a breakthrough in the efficiency of oxide perovskite photovoltaics was achieved. The band gap of Bi_2FeCrO_6 thin films was reduced to 1.4 eV through Fe/Cr cation disorder and strain relaxation, and 8.1%-efficient photovoltaics were achieved, although processing temperatures were relatively high, at 600 °C. The efficiency achieved is the highest (along with Cu_2O) for oxide-based photovoltaic absorbers.[6] In inorganic oxide perovskites, efficiencies reaching 20% may be achievable, based on the detailed balance limit and spectroscopically limited maximum efficiency, reinstating this class of materials as potentially viable commercial solar absorbers. The perovskite family therefore demonstrates substantial versatility in composition, properties, and processability, with significant promise for photovoltaic applications.

Next-generation thin film solar cells are critically required for sustainable energy harvesting on the utility scale to provide renewable energy. Currently, 94.5% of the photovoltaics market is based on silicon solar cells,[21] but the silicon-based module itself only contributes to a minority of the total cost of the solar panel.[22] Increasing the efficiency beyond the radiative limit for single-junction silicon solar cells is therefore important for reducing the levelized cost of electricity (LCOE). This has already been achieved by monolithically integrating a lead-halide perovskite top-cell with a silicon bottom-cell, and technoeconomic analyses predict that these tandem devices have lower LCOE than silicon single-junction devices, assuming a tandem module lifetime of 20 years, with a degradation rate of 1%.[23] Lower LCOEs can also be achieved through all thin-film tandems, in which a lead-halide perovskite top-cell is combined with a near-infrared absorbing thin film bottom cell,[23] such as a mixed lead-tin halide perovskite,[12,24] but the material requirements for efficient solar absorbers overlap with the requirements for a wide range of other electronic applications, including light-emitting diodes (e.g., for ultrahigh definition displays),[17] photoelectrodes (for water splitting to produce solar fuels),[25–27] photodetectors,[28,29] and radiation detectors.[30] As such, the development of perovskite thin films for photovoltaics can also have a significant impact across the broader electronics application space.

The performance and stability of both halide and oxide perovskites are essential factors in their development in electronic devices. Although these are commonly tuned through the composition and processing, tuning the dimensionality also plays an important role. Dimensionality includes the crystal structure (3D, 2D, 1D, and 0D), electronic dimensionality, and form factor (thin film, 2D electron gas, nanoplatelet, or nanocrystal), as illustrated in **Figure 1**. Historically, 3D perovskites have been considered, but reducing the structural dimensionality can lead to improvements in the stability (environmental and thermal), as well as confinement of charge-carriers to increase the PLQE. On the other hand, lowering the dimensionality lowers the mobility in one or more crystallographic directions and makes it more likely that charge-carriers couple to phonons, forming polarons that further reduce the mobility. Beyond changing the dimensionality of the material, reducing the form factor dimensionality from bulk thin films to nanoplatelets (2D) or quantum dots (0D) can also open up new opportunities, such as blue-shifting the band gap for light emission applications through quantum confinement rather than changing the composition (which could introduce deeper trap states). In addition to performance and stability, the toxicity of the perovskite compound is also a critical consideration in applications for electronic devices, especially since the Regulation of Hazardous Substances directive (RoHS) limits the Pb content in electronic devices to 0.1 wt% (although outdoor PVs are currently exempt).[31] As such, there has been an emphasis on the development of lead-free and low-toxicity oxide, sulfide, and selenide perovskites, as well as the design of lead-free materials which are identified through "inspiration" from the defect tolerance of the lead-halide perovskites (i.e., perovskite-inspired materials or PIMs).[32,33] In the development of these lead-free materials, dimensionality plays a critical role in their selection and optimization.

This review examines the role of dimensionality on the performance and stability of perovskite compounds and their derivatives, and the scope of this review is illustrated in Figure 1. In particular, we draw together insights into three broad families of materials: 1) inorganic oxide, sulfide, and selenide perovskites; 2) lead-halide perovskites; and 3) lead-free perovskite-inspired materials. We discuss how the structural and electronic dimensionality, as well as the form factor, influences the optoelectronic properties of these materials, and the impact on device performance and stability. Photovoltaics are primarily focused on, but comparisons are also drawn with light-emitting diodes. This review shows the new opportunities enabled by controlling dimensionality in these classes of materials, but also the challenges. We finish by suggesting how these challenges could be overcome, which could inform future materials design and engineering efforts.

2. The Role of Dimensionality on the Functionality of Inorganic Oxide and Chalcogenide Perovskites

Although oxide perovskites were the first class of perovskites investigated, they have only recently gained interest for photovoltaics. In particular, oxide perovskites can provide important advantages over lead halide perovskites in terms of lower toxicity and improved thermal and environmental stability. Oxide perovskites are also processable by a wide range of methods. In this section, we will describe the different forms of inorganic oxide-, sulfide-, and selenide-based perovskites, and the role of dimensionality on the optoelectronic properties. We note that perovskite nitrides (ABN_3) or oxynitrides ($ABO_{3-x}N_x$) may also be interesting but have not shown promising optoelectronic properties yet, although $LaWN_3$ has been predicted to be semiconducting and ferroelectric with an indirect bandgap of 1.98 eV and a direct bandgap of 2.23 eV,[37] and $LaTiO_2N$ has a bandgap of 2.1 eV.[38] Dimensionality can be understood at many levels: the geometry of the crystal structure (e.g., 3D as in single perovskites or 2D as in layered perovskites), the geometry of the devices, or the

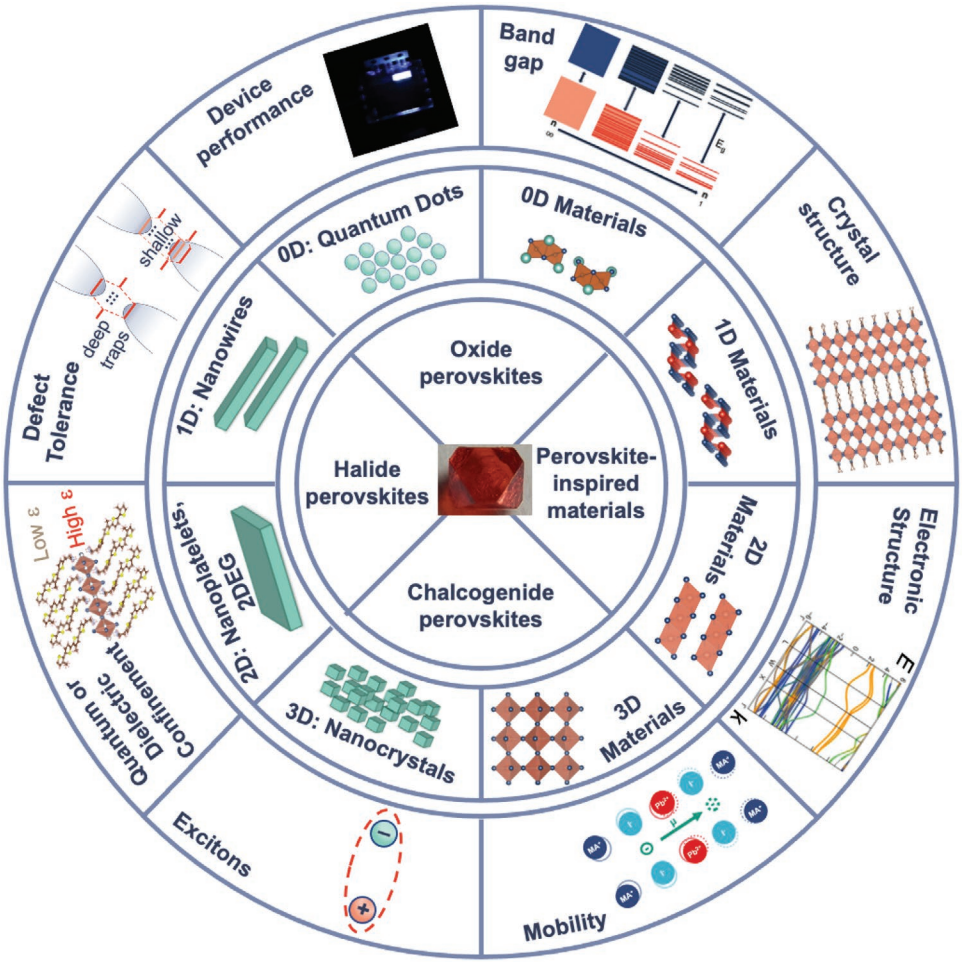

Figure 1. Scope of this review, including the materials covered and their dimensionalities, as well as the properties discussed. Center photograph of double perovskite single crystal: Reproduced with permission.[34] Copyright 2016, American Chemical Society. Electronic structure: Reproduced with permission.[35] Published 2020 by the Royal Society of Chemistry. Device performance: Reproduced under the terms of CC-BY license.[36] Copyright 2019, American Chemical Society.

shape of the materials (e.g., 2D layers, nanowires). The main aim of this section is to review the current status of inorganic perovskites for optoelectronics and the role of dimensionality on performance.

2.1. Evolution of Oxide Perovskites for Photovoltaics

While lead-halide perovskites are now studied by hundreds of groups worldwide, inorganic perovskites based on oxides, sulfides, and selenides are being studied for their optoelectronic properties by a smaller, but growing, community. The principal challenge is their significantly higher melting points compared to LHPs, and so if they are processed at practical temperatures of 500 °C or lower (i.e., at temperatures compatible with FTO-coated conducting glass), their defect concentrations would be high. Historically, oxide perovskites have been widely studied for their unique ferroelectric properties. $PbTiO_3$, $BaTiO_3$, and $BiFeO_3$ are typical examples. The first solar cells based on such ferroelectric oxide perovskites were already being investigated in the 1980s but the field emerged from 2010, as shown in **Figure 2**. While many publications report solar cell efficiencies well below 1%, as noted above, a solar cell efficiency of 8.1% was reported in the ferroelectric double perovskite Bi_2FeCrO_6.[6] Such an efficiency competes with the world record among oxide solar cells of 8.1% in Na-doped Cu_2O solar cells.[39] To date no other oxide rivals these two examples.[40]

2.2. Single ABO_3 Perovskites (3D)

Here, we review the optoelectronic properties of single ABO_3 perovskites that can be described as 3D. Most single oxide perovskites have a wide band gap above 3 eV due to the large difference in electronegativity between the oxygen and metal atoms. The ideal band gap for a single band gap solar cell is 1.34 eV according to the detailed balance limit.[42] For two-terminal tandem solar cells with a c-Si bottom cell, the ideal top cell bandgap is approximately 1.72 eV.[43] Wider band gaps are more suitable for water splitting, but even in this case, the optimal band gap of 2.03 eV is below the band gap of typical single oxide perovskites.[44]

For example, titanates such as $PbTiO_3$ (PTO) and $BaTiO_3$ (BTO) are well known for their ferroelectric properties. However, their band gaps are higher than 3 eV which makes them poor solar absorbers. Strategies to reduce this band gap involve alloying. For example, the band gap of PTO films was reduced from 3.35 to 2.86 eV by forming $PbTi_{0.7}Ni_{0.3}O_3$.[45]

Other examples of single perovskites investigated for their optoelectronic properties include tantalates, nickelates, niobates, ferrites, manganates, and chromates. However, most of these materials have not yet been explored for PV applications. Out of these, currently the ferrites have been explored the most for PV applications, and these are described in Section 2.3.

$SrTiO_3$ has also been proposed for use in LHP solar cells as a mesoporous electron-transporting layer.[46,47] By replacing the commonly used TiO_2 with $SrTiO_3$, the open circuit voltage was increased up to 1.01 V, which was 25% higher than the value of 0.81 V obtained using the conventional mesoporous TiO_2 electron transport layer.[46] This was attributed to favorable band alignment and improved surface coverage of the LHP thin film. LHP solar cells are often unstable under ultraviolet irradiation and this is partly due to the photocatalytic degradation of the LHP by TiO_2. A La-doped $BaSnO_3$ perovskite was proposed to replace the TiO_2 and it was found that the solar cells retained 93% of their initial performance in a nitrogen-filled glovebox after 1000 h of 1-sun illumination, whereas the solar cell with TiO_2 completely degraded after 500 h.[48]

Another category of oxide perovskites are Mott insulators. Mott insulators should be conductive according to conventional band theory but are experimentally found to be insulators. These materials become conductive due to a variety of factors, such as strain, defects, or impurities. Interestingly, Mott insulator perovskites can present low band gaps compatible with the solar spectrum. They include $LaVO_3$ (optical bandgap 1.1 eV), $YTiO_3$ (0.6 eV), YVO_3 (1.6 eV), $LaMnO_3$ (1.03 eV), and $SrMnO_3$ (0.64 eV).[49–52] The band gap originates from the correlation-induced electron-electron repulsion leading to a filled lower Hubbard band and unfilled upper Hubbard band (these bands are described in the frame of the Hubbard model).[53] However, in the case of $LaVO_3$, it was shown that it provides a carrier density that is too high for solar cell applications and that it is a poor charge-transport medium.[52] In the case of $LaMnO_3$, it was shown that the minority carrier diffusion length is rather short, in the nanometer range, whereas LHPs have diffusion lengths in the micron range.[49]

Single perovskites have also been widely investigated for photocatalysis (PC), where electrocatalysts are deposited on a solar absorber material and immersed in an electrolyte.[38] In general, for all material types the factors limiting photocatalytic performance are similar to PVs, such as limited absorptance, high electron-hole pair recombination, and limited stability. Of course, stability is not a major concern for inorganic perovskites. The main concerns are that many single perovskites have a large band gap and are only capable of absorbing in the UV part of the solar spectrum. Also, the presence of high defect concentrations in high melting point materials processed at relatively low temperatures leads to unwanted non-radiative recombination. Therefore, the search for low band gap, lower melting point inorganic perovskite-like systems is of interest for both photocatalysis and PV.

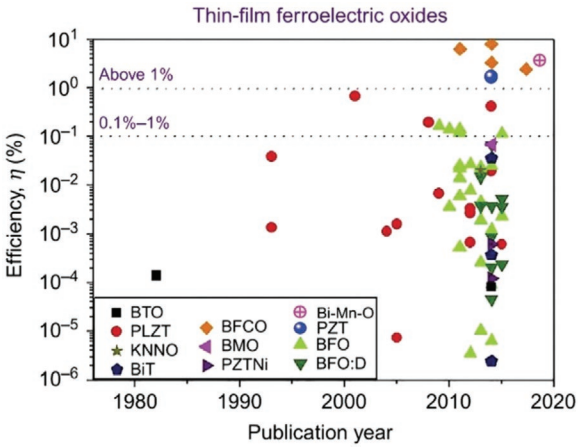

Figure 2. Timeline plot for the reported PV device efficiencies of thin-film single layer ferroelectric oxides. Reproduced with permission.[3] Copyright 2019, The Royal Society of Chemistry. Reproduced with permission.[41] Copyright 2018, Elsevier.

The use of inorganic perovskites in PV can strongly benefit from the positive and negative learnings gained from their implementation in photocatalytic devices, such as the impact of processing and defects on performance. More than 200 perovskite-related structures have already been reported as photocatalysts by 2016.[38] Single perovskites, such as $SrTiO_3$, $NaTaO_3$, $AgNbO_3$, $KNbO_3$, $NaNbO_3$, and $BiFeO_3$ have been investigated, and dopants have been introduced to narrow their band gaps.[3] In particular, Ru-doping enabled the band gap of $SrTiO_3$ to be reduced from 3.2 to 2.0 eV.[54]

2.3. Ferroelectric ABO_3 Perovskites

The ferroelectric photovoltaic effect was demonstrated in 1956 in barium titanate.[55] However, dedicated efforts to exploit this effect in devices only began in 2010. The ferroelectric photovoltaic effect results in the creation of a photogenerated current under short-circuit conditions parallel to the direction of the ferroelectric polarization axis. Sometimes an open circuit voltage much higher than the band gap of the material is obtained, as explained in the next paragraph. There are several mechanisms involved and these are still not completely understood. Ferroelectric solar cells do not require a *p-n* junction, as in conventional solar cells, and charge separation can originate from the polarization-induced internal electric field. Such solar cells necessitate what is called a ferroelectric semiconductor.

$BiFeO_3$ is the most studied ferroelectric material for photovoltaic applications.[56] It has a relatively high direct band gap of ≈2.7 eV.[20] Most devices based on $BiFeO_3$ provide low conversion efficiency;[40] however, in the case of planar configurations such solar cells can provide open circuit voltages higher than a dozen volts.[20] **Figure 3** shows such a planar configuration with $BiFeO_3$ grown epitaxially on single-crystalline (110) $DyScO_3$. The photovoltaic properties are present only when the current flows perpendicular to the domain walls, as if each domain wall was contributing a small value to the open-circuit voltage.[20] Photoelectrochemical cells of $BiFeO_3$–$SrTiO_3$ have

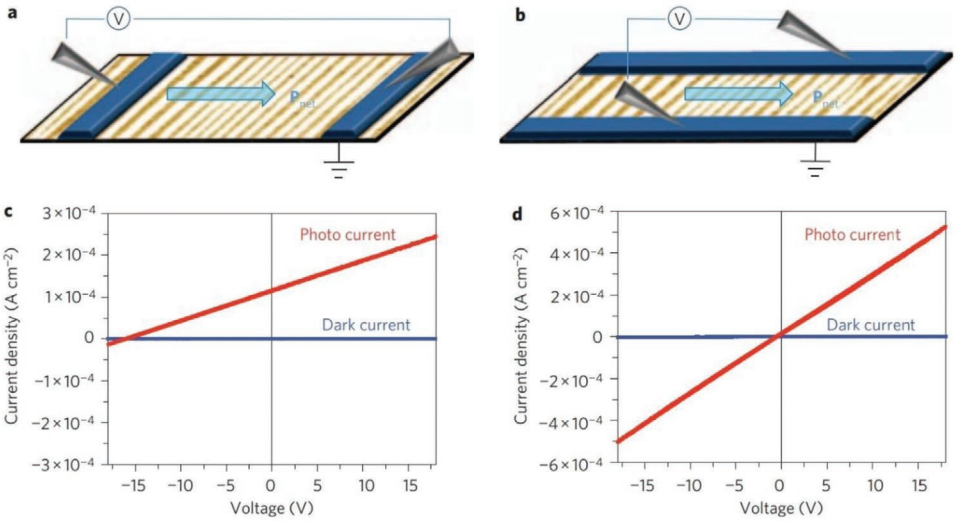

Figure 3. Schematics and *I–V* measurements of the $BiFeO_3$ photovoltaic devices where the current flows a,c) in a perpendicular direction to the domain walls and b,d) in a parallel direction to the domain walls. Reproduced with permission.[20] Copyright 2010, Springer Nature.

also been successfully demonstrated and in solid solution films the positive role of trap states has been shown, namely that fast electron–hole recombination is suppressed and photocurrent density in the visible-light region improved.[27]

Another material of interest is $BiMnO_3$, which has a direct bandgap of about 1.2 eV.[57] Such a low band gap is appealing for single-junction PV. However, for ferroelectric PV applications the remnant polarization of $BiMnO_3$ is ten times lower than that of $BiFeO_3$,[40] which makes it less efficient at carrier extraction. Recently solar cells with a conversion efficiency of 4.2% were obtained with films of mixed $BiMnO_3$ and $BiMn_2O_5$.[57] This was shown in high temperature-grown epitaxial films. $BiMnO_3$ has also been investigated in photoelectrochemical solar cells in the form of thin films and nanostructures.[58]

Other types of ferroelectric perovskite materials for optoelectronics include the single-phase oxide solution $[KNbO_3]_{1-x}[BaNi_{1/2}Nb_{1/2}O_{3-\delta}]_x$ (KBNNO) that can provide tunable direct band gaps down to 1.39 eV, much lower than the 3.8 eV for single $KNbO_3$.[19] The absorption coefficient at 885 nm wavelength is 2.5×10^4 cm^{-1}, which is comparable to CdTe and GaAs.[19] High solar cell conversion efficiencies with such materials have not been demonstrated yet. The limiting factor for ferroelectric PV is to find high polarization ferroelectric semiconductors with resistivities that are not too high, and with low band gaps close to the optimum for single-junction (1.34 eV) or top-cells (1.72 eV) applications and reduced melting points.

It should be noted that there are recent studies that incorporate ferroelectric perovskite oxides as interfacial layers in lead-halide perovskite solar cells (similar to the work described earlier with $SrTiO_3$), enhancing the open-circuit voltage. The idea is to benefit from the ferroelectric polarization-induced internal electric field to enhance charge separation and charge transfer in the structure. In this way, a high solar cell efficiency of 16.37% has been obtained in LHP solar cells that do not have a hole transport layer, and which incorporate an ultrathin $PbTiO_3$ layer made by solution processing.[59,60] This was more efficient than the reference devices without $PbTiO_3$, which was only 13.81% efficient.[59,60] The device structure was glass/F:SnO_2/TiO_2/$PbTiO_3$/$CH_3NH_3PbI_3$/carbon nanotubes.

2.4. Oxide Double Perovskites

Double perovskites are derived from single perovskites with the A or B site occupied by two types of cations, giving either an $A'A''B_2O_6$ (double A-site) or $AB'B''O_6$ (double B-site) structure. Oxide double perovskite can give enhanced optoelectronic properties compared to their oxide single perovskite counterparts. In the case of ferroelectric Bi_2FeCrO_6, two groups have independently demonstrated that the band gap could be varied from about 2.6 to 1.9 eV by increasing the Fe/Cr cationic order in the structure.[6,61] The ferroelectricity originates from Bi^{3+} ions at A sites, as in the case of $BiFeO_3$ and $BiMnO_3$. The band gap is tuned by the interaction between Fe and Cr at the B site, via O. Using a tandem Bi_2FeCrO_6 absorber with three different band gaps, a solar cell conversion efficiency of 8.1% was demonstrated (**Figure 4**).[6]

Other double perovskite systems are being investigated for their photovoltaic properties, such as A-site ordered $CaMnTi_2O_6$ (predicted band gap of 1.7–2.9 eV),[62] $Ba_2SbV_{1-x}Ta_xO_6$ (1.0–1.6 eV band gap),[60] $KBaTeBiO_6$ (1.88 eV band gap),[63] Ln_2NiMnO_6 (Ln = La, Eu, Dy, Lu) (1.08–1.19 eV band gap).[64]

2.5. Layered Oxide Perovskites

Brownmillerites ($A_2B_2O_5$ or $A_2B'B''O_5$) are polymorphs of the perovskite structure where 1/6th of the oxygen atoms are removed, thus reducing the crystal symmetry. The structure is composed of alternating BO_6 octahedral and BO_4 tetrahedral layers (**Figure 5**). Reducing the oxygen coordination is a promising strategy to reduce the band gap.[65] A recent example is the multiferroic brownmillerite $KBiFe_2O_5$ that has a direct bandgap of 1.6 eV and a theoretical maximum efficiency of

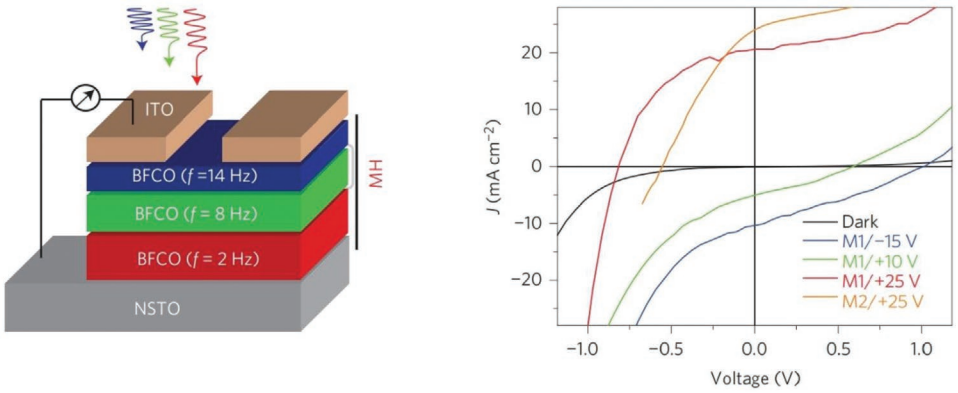

Figure 4. Left: Schematic of a multilayered Bi_2FeCrO_6 (BFCO) solar cell (Nb:$SrTiO_3$ (001)/BFCO (2 Hz, band gap 1.4 eV)/BFCO (8 Hz, band gap 1.8 eV)/BFCO (14 Hz, band gap 2.2 eV)/Sn-doped indium oxide [ITO]). Different PLD laser repetition rates for BFCO layers result in a variable band gap. Right: *J–V* characteristics of two devices M1 and M2 after poling with a high voltage pulse. Reproduced with permission.[6] Copyright 2014, Springer Nature.

30%.[65] Epitaxial thin films of such materials have recently been obtained, however solar cell short-circuit current densities were in the same range as $BiFeO_3$.[66]

The Aurivillius phase $(Bi_2O_2)(A_{n-1}B_nO_{3n+1})$ and the Ruddlesden–Popper (RP) phase $(A_{n+1}B_nO_{3n+1}$, or more generally $A_2'A_{n-1}B_nO_{3n+1})$ are 2D compounds homologous to single perovskites and are two prototypical examples of layered perovskites. The RP phase is well-known among halide perovskites as a 2D perovskite and is discussed in more detail later.[68] In this phase, A, A′, and B are cations and n is the number of the layers of BO_6 octahedra in the perovskite-like stack. In the Aurivillius phase, a number n of pseudo-perovskite layers are sandwiched between layers of $[Bi_2O_2]^{2+}$ (Figure 5). Examples of the Aurivillius phase are ferroelectric $n = 1$ Bi_2WO_6 (band gap of 2.82 eV),[69] Bi_2MoO_6 (band gap of 2.5–2.8 eV),[70] or $n = 2$ $PbBi_2Nb_2O_9$ (band gap of 2.88 eV).[71] Examples of the RP phase are Sr_2SnO_4 (band gap of 4.6 eV)[72] and $Li_2CaTa_2O_7$ (band gap of 4.36 eV).[73] All these materials have been studied for photocatalysis and many provide high photocatalytic activity.[38] However, these band gaps are too high for PV applications. Such structures can lead to ferroelectric properties due to a non-centrosymmetric structure caused by octahedral rotations and distortions. Another layered perovskite example is $La_2Ti_2O_7$, studied as a visible light photocatalyst, and its band gap was decreased from 3.28 to 2.51 eV through N-doping.[74] While 2D layered perovskites have been thoroughly studied in the field of halide perovskites for photovoltaics (see Section 3.2), as of today, inorganic layered perovskites (which are commonly studied for ferroic, superconducting, ionic, and dielectric behavior) are not very well established for optoelectronic applications.

2.6. 2D Oxide Perovskites

Following the discovery by Ohtomo and Hwang in 2002 that the interface between two band insulators, $SrTiO_3$ and $LaAlO_3$, can become conductive and provide a quasi 2D-electron gas (a high mobility electron gas mostly free to move in two dimensions),[75,76] a similar kind of oxide heterostructure based on $LaVO_3$, $LaFeO_3$, and $SrTiO_3$ was proposed by Assmann et al.[77] It was mentioned earlier that $LaVO_3$ has a direct bandgap of 1.1 eV, which is highly suitable for single-junction photovoltaics. $LaVO_3$ grown on $SrTiO_3$ has an internal potential gradient that can help to separate the photogenerated electron-hole pairs. Such oxide multi-layered heterostructures have not been implemented in solar cell architectures yet, likely because of fabrication complexities, in which there is monolayer by monolayer growth alternating between two different materials.

One interesting recent development with 2D oxide perovskites is the achievement of freestanding $SrTiO_3$ and $BiFeO_3$ ultrathin crystalline films down to a thickness of 1–4 unit cells,[78] thanks to the use of a sacrificial buffer layer of $Sr_3Al_2O_6$.[79] The freestanding crystalline films can be transferred to other substrates such as Si.[80] While the outcomes in terms of optoelectronics are unknown, these systems have the potential to rival other 2D materials such as graphene and transition-metal dichalcogenides because they can provide multifunctional properties, such as semiconducting properties, superconductivity, ferroelectricity, and colossal magnetoresistance. However, it is important to note that metal oxides possess strong interlayer ionic bonds and thus in their 2D form there are dangling bonds that induce surface instability.[81] It is clear that the nature of oxide surfaces and their reconstructions impact their performance.[82] The nature of the surfaces of 2D oxides requires a much deeper understanding.

2.7. 1D Oxide Perovskite Nanowires

Oxide perovskites in 1D form are not very common for optoelectronics, as compared to thin films, but examples of 1D oxide perovskites that have been synthesized and investigated include $BaMnO_3$ nanorods, $La_{0.5}Sr_{0.5}MnO_3$ (LSMO) nanowires, $La_{0.8}Sr_{0.2}MnO_3$ nanofibers, and $La_{0.7}Ca_{0.3}MnO_3$ and $La_{0.325}Pr_{0.300}Ca_{0.375}MnO_3$ nanotubes.[83] While such structures have been used in transistors and spintronics, applications in optoelectronics are scarce. **Figure 6** shows transmission electron microscopy (TEM) images of LSMO manganite nanowires fabricated by hydrothermal synthesis, showing that the nanowires are single crystalline.[84]

Nanowire oxide perovskite solar cells can be envisaged as a tool to remedy a low minority carrier diffusion length as

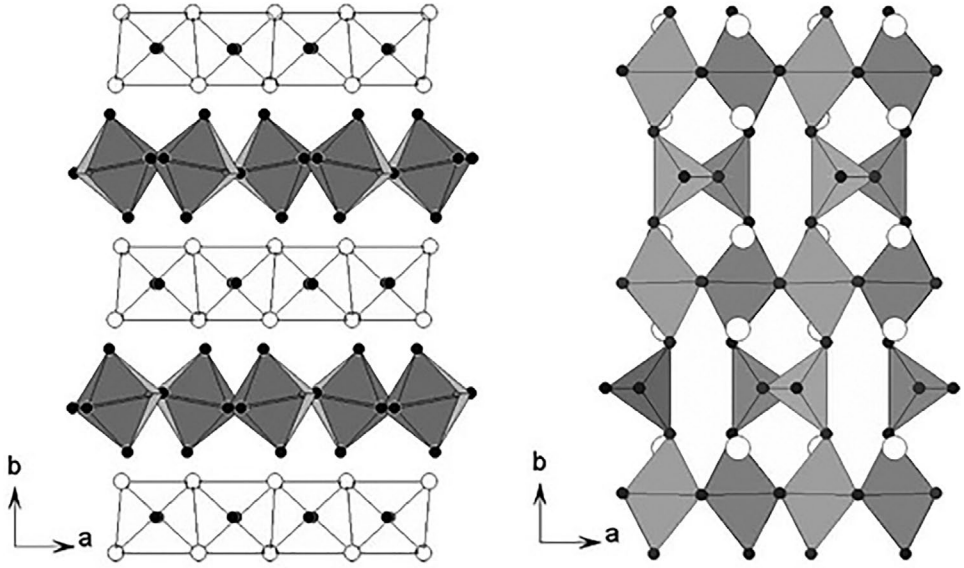

Figure 5. Idealized crystal structures of (left) Aurivillius (e.g., Bi_2WO_6: Bi_2O_2—tetrahedra; WO_6—octahedra) and (right) brownmillerite perovskites (e.g., $Ba_2In_2O_5$: Ba—open circles, InO_6—octahedra; InO_4—tetrahedra). Reproduced under the terms of the CC-BY license.[67] Copyright 2006, Springer-Verlag.

observed in some single perovskite oxides. ZnO nanowires have already been used to fabricate all-oxide, ZnO/Cu_2O, and $ZnO/TiO_2/Cu_2O$ solar cells, albeit with limited conversion efficiency.[85,86] It is expected that in the future all-oxide perovskite nanowire-based solar cell will emerge. In addition, nanowires are promising for photocatalytic applications because of the high surface area to volume ratio.

2.8. Inorganic Sulfide and Selenide Perovskites

Unlike oxides, inorganic sulfide and selenide perovskites have not been exploited in PV devices yet because their potential is only just starting to be discovered. Compared to sulfides and selenides, oxide perovskites are easy to manufacture as they do not usually require toxic precursors and post-growth oxidation can easily occur. However, as already mentioned, oxide perovskite thin films are usually grown far below their high melting points. The defect formation energies are low, and many defects are present (including point defects, e.g., oxygen vacancies) and they play an important role in the properties of the films. Some new methods can greatly improve the perfection of oxide thin films, nevertheless lower melting point temperature systems would be highly beneficial for enabling the growth of perovskites with low structural defect density at practical deposition temperatures.[87] Of course, not only is achieving low defect density within grains important, so is achieving lower intergrain defect density. This can be achieved by growing larger grains, thereby reducing the density of grain boundaries. According to the structure zone model, materials with lower melting points can achieve larger grains at the same growth temperature because the deposition temperature would represent a larger homologous temperature. In this regard, sulfides (and selenides, which are chemically similar to sulfides) are appealing because they have melting points approximately half of that of oxides.[88] Hence, for many of these chalcogenide perovskites, there is the potential of growing at 600 °C or below without suffering from large defect densities of nanoscale grain sizes, as would be the case for most oxides grown at similar temperatures.

Only very few chalcogenide ABS_3 perovskites have been reported so far, although $BaZrS_3$ was already synthesized in 1957.[89] This material is an ionic semiconductor with an experimental direct band gap of 1.73 eV, which is significantly lower than the 5 eV band gap of the oxide $BaZrO_3$ counterpart.[90] Furthermore, the band gap of $BaZr(O_xS_{1-x})_3$ is tuneable from 1.73 eV (x = 0.24) to 2.87 eV (x = 0.95). This low and adjustable band gap is due to the fact that the valence band of these perovskites is mainly formed by p states of O and S, while S 2p states are higher in energy than the O 2p states and thus the former narrows the band gap by reducing the ionization potential.[90] Also, $CaZrS_3$ has a band gap of 1.90 eV.[90] Thus, this class of materials has potential for photovoltaics and constitutes a strong opportunity for original research because the optoelectronic properties of these materials are largely unexplored. Chalcogenide perovskites promise enhanced stability compared to halides because the Coulomb interaction in chalcogenides is much larger than in the halides.[91] Thin films of $BaZrS_3$ have been obtained by sputtering at ambient temperature, followed by annealing at temperatures ranging from 650 to 1000 °C. While diffraction peaks were obtained in films annealed at 650 °C, good crystallization required rapid thermal annealing at approximately 900 °C.[92] Another route to growing $BaZrS_3$ is through pulsed laser deposition of $BaZrO_3$ followed by sulfurization at 900–1050 °C.[93] $LaYS_3$ was also proposed with a direct bandgap of about 2 eV, but its integration into solar cells is difficult due to the high sulfurization temperature of 1000 °C.[94] Formation of the sulfide phases during growth at moderate temperatures is an important goal for future work. There is promise in this direction, since $BaZrS_3$ has been fabricated

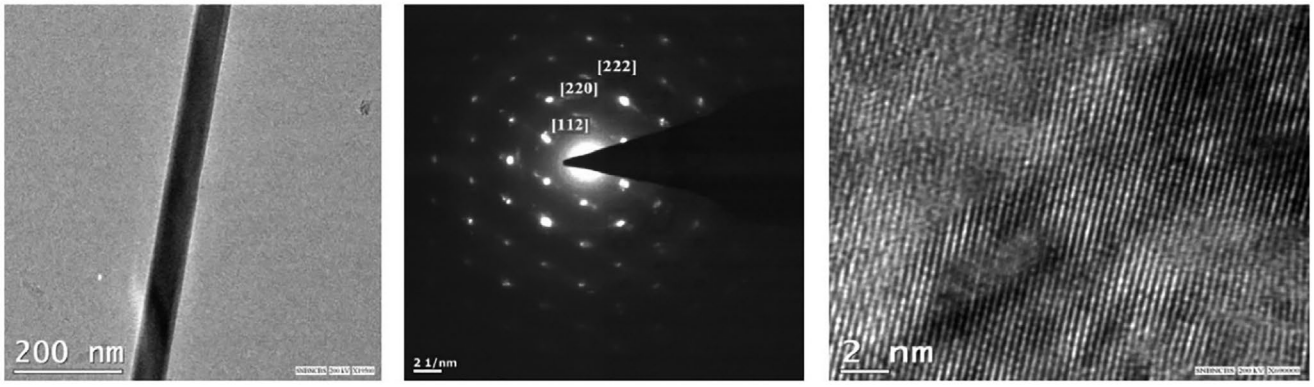

Figure 6. a) TEM image of a single LSMO nanowire of diameter around 45 nm; b) selected area diffraction pattern; c) high-resolution TEM showing the crystalline nature of the LSMO nanowires. Reproduced under the terms of the CC-BY license.[84] Copyright 2013, Hindawi Ltd.

with near unity yield at temperatures between 550–600 °C by direct reaction of barium sulfide powder with Zr.[95,96]

Some other compounds have provided a needle-like phase, with a structure different from the perovskite structure, such as $SrTiS_3$, $SrZrS_3$, $CaZrS_3$, $BaZS_3$, $CaHfS_3$, $SrHfS_3$, and $BaHfS_3$.[60,97]

Similar to oxide perovskites, derived phases are also present in chalcogenide perovskites. For example, RP-type layered chalcogenide perovskites were obtained, such as $Ba_3Zr_2S_7$, which is a $n = 2$ RP phase of the sulfide perovskite $BaZrS_3$, with a bandgap of 1.28 eV.[98] Such 2D layered structures that are derived from the perovskite structure can present interesting properties due to octahedral rotations and distortions. These materials can also be considered in comparison to the world of 2D materials such as graphene, MoS_2, silicene, and germanene. The zero band gap of graphene limits its use in the semiconductor industry while no 2D semiconductor with linear electronic dispersion and ultrahigh carrier mobility as in graphene has been found experimentally yet. In contrast to metal oxides, the bonding character in sulfides and selenides is more covalent than in the oxides and hence 2D materials are more easily formed. A solution could emerge from the 2D RP chalcogenide perovskite semiconductor $Ca_3Sn_2S_7$ that presents, from first-principles calculations, a graphene-like linear electronic dispersion, a direct bandgap of 0.5 eV, and a carrier density of 6.7×10^4 $cm^2V^{-1}s^{-1}$ at room temperature.[99]

Also, chalcogenide double perovskites are predicted to provide bandgaps suitable for photovoltaics such as Sr_2SbTaS_6, Ba_2SbTaS_6, Sr_2BiNbS_6, Ba_2BiNbS_6, Sr_2BiTaS_6, Ba_2BiTaS_6, Ba_2SbTaS_6, Ba_2BiNbS_6, and $Ba_2BiTaSe_6$.[91]

3. From 3D to 0D: Effect of Dimensionality on Recombination and Charge-Carrier Transport in Lead-Halide Perovskites

LHPs have outstanding optoelectronic properties, namely high charge-carrier mobilities, long diffusion lengths, tunable band gaps, long charge carrier lifetimes, and high absorption coefficients.[14,100–104] In particular, LHPs have been found to be defect tolerant (**Figure 7**a).[105–108] This has been key in enabling LHP thin films to be grown by simple solution- and vapor-based methods at low temperatures (typically at 100–150 °C) while achieving high efficiencies surpassing those of other thin film and multicrystalline silicon solar cells.[109] To a large extent, the beneficial properties of the LHPs can be attributed to the presence of Pb (and in analogous form Sn in Sn-based perovskites). The s and p orbitals of the Pb^{2+} cations hybridize with the p orbitals of the I^- anions to form an electronic structure that is conductive to traps being shallow rather than deep (refer to Figure 7a; further details in Section 4.2).[15,106,110] In addition, owing to Pb^{2+} being a heavy metal cation, there is strong spin-orbit coupling, leading to smaller band gaps, which also favors shallow trap formation.[106] The high Born effective charge results in LHPs exhibiting high dielectric constants, which leads to smaller capture cross-sections of charged defects.[15,106] Together, these effects result in low non-radiative recombination rates despite high densities of points defects.

Initially, the focus for perovskite photovoltaics was on LHPs with 3D structural dimensionality. However, due to its challenges in stability, low exciton binding energies, as well as interface and surface recombination, lower dimensional halide perovskites have gained increasing attention. These properties are important for photovoltaic, light-emitting diode (LED) and other optoelectronic applications. Changing the dimensionality also influences the band gap (Figure 7b) and band dispersion (Figure 7c), which affects the performance of these materials in devices. By engineering the composition, crystal structure, and dimensionality of these materials, it is possible to tune their optoelectronic properties to the optimal values for the desired application. Understanding the role of dimensionality on the optoelectronic and materials properties is therefore essential to achieving devices with improved efficiency and stability and is therefore the focus of this Section. A summary table of the key optoelectronic properties of LHPs with different dimensionalities is displayed in **Table 1**.

3.1. Bulk Perovskites

Bulk LHPs, with a 3D crystal structure and processed as thin films, have shown excellent transport properties, and have

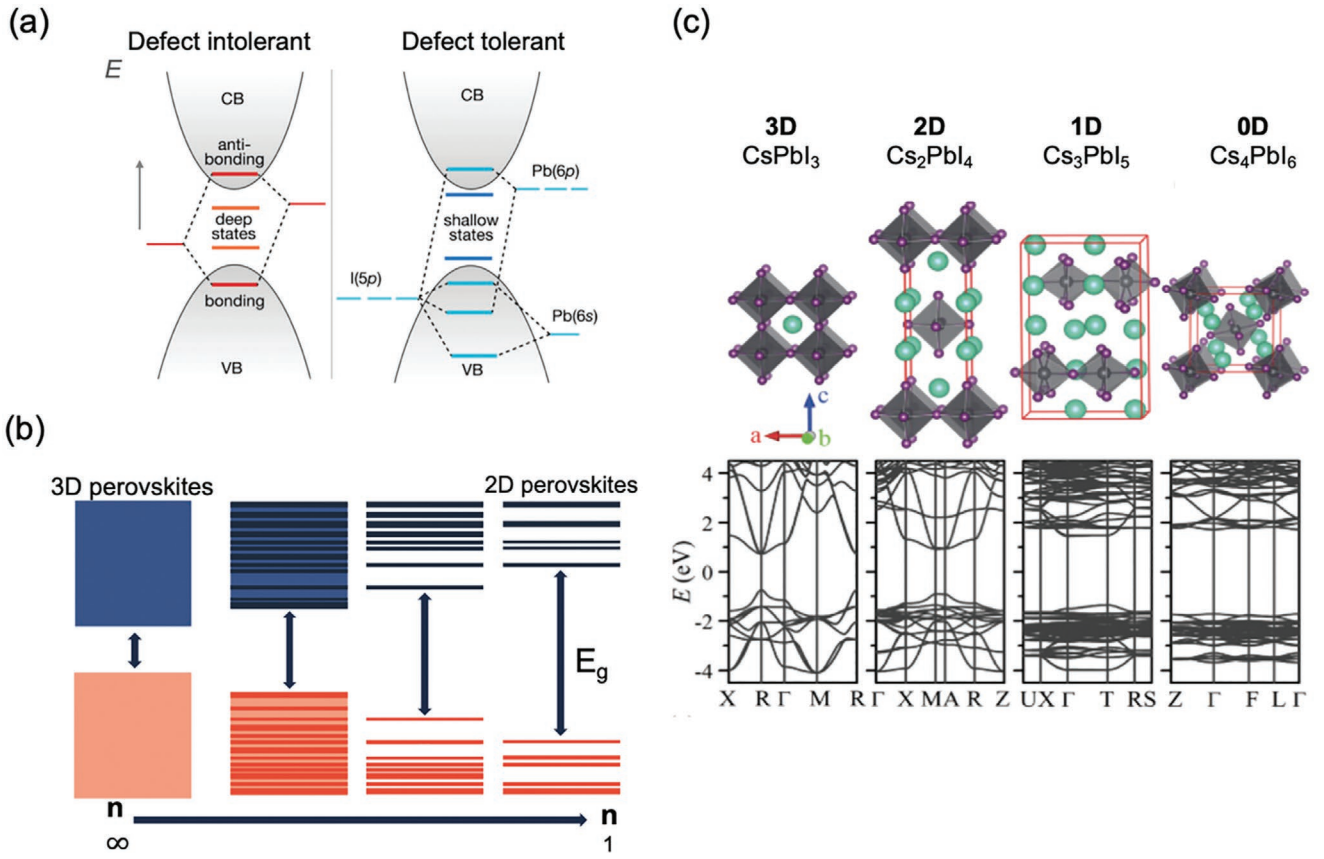

Figure 7. a) Comparison of the electronic structure of defect sensitive (left) and defect tolerant (right) materials. Reproduced with permission.[15] Copyright 2017, American Chemical Society. Illustration of the effect of structural dimensionality on the b) band gap and c) electronic structure and band dispersion. Part (c) reproduced with permission.[111] Copyright 2017, Published by the Royal Society of Chemistry. N.B.: in Part (b), *n* refers to the number of inorganic layers between organic ligands (e.g., in Ruddlesden–Popper or Dion–Jacobson perovskites), with $n = \infty$ referring to a 3D perovskite.

consistently led to perovskite photovoltaics with the certified highest efficiency throughout its decade of development.[9]

3.1.1. Crystal Structure

Bulk 3D LHPs have the same crystal structure as the oxide and chalcogenide perovskites described in Section 2, but in this case, lead cations are octahedrally coordinated with halides (I, Br, or Cl), and the lead-halide octahedra form a corner-sharing array, giving rise to a cubic, tetragonal or orthorhombic unit cell. The cuboctahedral cavities (voids between octahedra) are occupied by the A-site cation, which needs to fall within a narrow range of ionic radii in order for the perovskite phase (denoted α-phase) to be achieved. This can be quantitatively described by the Goldschmidt tolerance factor, which is defined as $t = (r_A + r_X) / [\sqrt{2}\,(r_B + r_X)]$, in which $r_{A,B,X}$ are the ionic radii of the A-, B-, and X-site as shown in **Figure 8**a.[112,113] The required values for the tolerance factor in order to stabilize the α-phase have been empirically found to be between 0.8 and 1.0.[114] Thus, for lead-iodide-based LHPs, methylammonium (MA, $CH_3NH_3^+$) is a suitable A-site cation because it results in a tolerance factor of 0.93. Other options for the A-site cation include Cs or formamidinium (FA, $CH(NH_2)_2^+$). The size of the cation in the A-site will determine the perovskite's dimensionality (Figure 8b), phase, and stability.

3.1.2. Stability

Stability has been a major challenge for bulk LHPs, limiting their commercial and long-term potential. LHPs are highly sensitive to temperature, UV-light, applied voltage bias, and moisture. The stability challenge has been addressed through the use of 1) mixed A-site cations (as described above), 2) encapsulation of perovskite modules (e.g., with glass and ethylene-vinyl acetate),[115] 3) 2D perovskite passivation layers,[10] and 4) atomic layer deposited oxide encapsulation layers.[116,117] As a result, perovskite devices with stable operation for >1000 h that can pass the IEC 61215 stability protocols have now been achieved.[115] More details on 2D perovskite passivation is given in Section 3.3.1.

3.1.3. Optoelectronic Properties

Band Gap: Although LHPs exhibit a direct band gap on average, within the lattice, the bandstructure is highly dynamic

Table 1. Properties of lead-halide perovskites discussed in Section 3.

Material	Space group	Band gap [eV]	Exciton binding energy [meV]	Effective mass/m_0	Mobility [$cm^2\ V^{-1}\ s^{-1}$]	Ref.
			Structurally 3D Materials			
$MAPbI_3$	$I4/mcm_{(RT)}$	1.6	16	0.25 (m_e)	35 (TF)	[388]
				0.19 (m_h)	27 (TF)	
$FAPbI_3$	$Pm\bar{3}m_{(RT)}$	1.5	14	0.23 (m_e)	–	[128,389–391]
	$\alpha-phase$			0.18 (m_h)		
$MAPbBr_3$	$Pm\bar{3}m_{(RT)}$	2.3	25	0.117 (m_e)	–	[128]
$MAPbCl_3$	$Pm\bar{3}m_{(RT)}$		–	–	42 (SC)	[392]
$CsPbI_3$	$Pnma_{(RT)}$	1.73	–	–	–	[127,389,393]
$FAPbBr_3$	$Pm\bar{3}m$	2.2	24	0.11 (m_e)	–	[127,389]
$MAPbI_{3-x}Cl_x$	–	1.6	14	0.105 (m_e)	47 (TF)	[127]
			Structurally 2D and quasi-2D Materials			
$(PEA)_2PbI_4$ (monolayer)	–	2.34	498.1	0.38 (m_e)	459 (μ_e)	[129,394,395]
				0.64 (m_h)	241 (μ_h)	
$(PEA)_2PbI_4$ (bilayer)	–	–	288	0.4 (m_e)	766 (μ_e)	[395]
				0.61 (m_h)	363 (μ_h)	
$(PEA)_2PbI_4$ (trilayer)	–	–	210	0.35 (m_e)	731 (μ_e)	[395]
				0.57 (m_h)	301 (μ_h)	
$(PEA)_2(MA)Pb_2I_7$	–	2.09	291	–	–	[129]
$(PEA)_2(MA)_2Pb_3I_{10}$	–	1.94	195.6	–	–	[129]
$(PEA)_2(MA)_3Pb_4I_{13}$	–	1.78	143.4	–	–	[129]
$(PEA)_2PbBr_4$	–	2.99	752.3	–	–	[129]
$(PEA)_2(MA)Pb_2Br_7$	–	2.77	345.9	–	–	[129]
$(PEA)_2(MA)_2Pb_3Br_{10}$	–	2.56	218.5	–	–	[129]
$(BA)_2PbI_4$	–	–	–	0.082 (m_e)	–	[395]
				0.144 (m_h)		
$(BA)_2(MA)Pb_2I_7$	–	2.43	467	–	–	[138,166]
$(BA)_2(MA)_2Pb_3I_{10}$	$Cc2m$	2.17	251	–	–	[138,166]
$(BA)_2(MA)_3Pb_4I_{13}$	$C2cb$	2.03	177	0.097 (m_e)	–	[138,140,166]
				0.141 (m_h)		
$(BA)_2(MA)_4Pb_5I_{16}$	$Cc2m$	1.91	157	0.094 (m_e)	–	[2,165]
				0.153 (m_h)		
$(BA)_2(MA)_5Pb_6I_{19}$	–	–	125	–	–	[138,166]
$(3AMP)PbI_4$	$P21/c$	2.23	–	–	–	[396]
$(3AMP)(MA)Pb_2I_7$	Ia	2.02	–	–	–	[396]
$(3AMP)(MA)_2Pb_3I_{10}$	Pa	1.92	–	–	–	[396]
$(3AMP)(MA)_3Pb_4I_{12}$	Ia	1.87	–	–	–	[396]
$(4AMP)PbI_4$	Pc	2.38	–	–	–	[396]
$(4AMP)(MA)Pb_2I_7$	Ia	2.17	–	–	–	[396]

RT, room temperature; SC, single crystal; PC, polycrystalline sample; TF, a thin film.

for $MAPbI_3$. It has been shown that the rotations of the MA cations result in a multi-bandgap material with combined direct and indirect band gap sub-structures (**Figure 9**). The fast rotation of MA in the perovskite cuboctahedral vacancies at room temperature or above makes the molecule behave as a single particle and the overall band structure that results is a combination of band structures, with the band gap being direct overall. The energy band structure for the 3D $MAPbI_3$ is illustrated

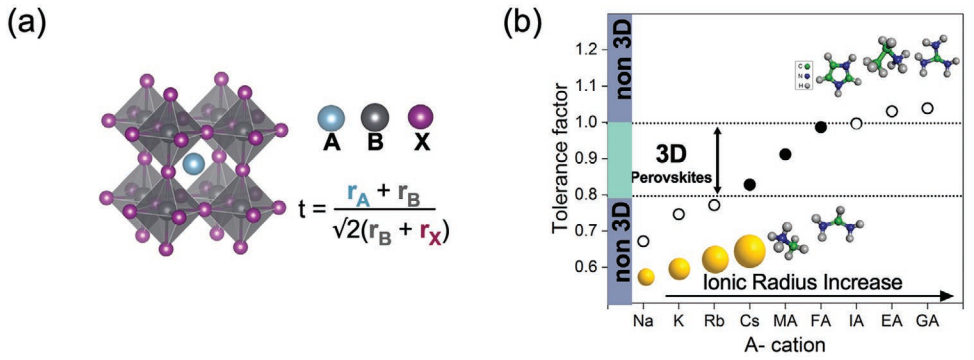

Figure 8. a) Lead halide perovskite structure and definition of the Goldschmidt tolerance factor t for an ABX_3 structure and b) the effect of the ionic radius size of the A-site cation on the tolerance factor.

for a cubic (Figure 9a) and tetragonal (Figure 9b) lattice.[118] Through first principles calculations, Zunger et al. have shown that organic–inorganic hybrid perovskites form a "polymorphous" network.[119] This happens because of a minimization of the internal energy, in which a distribution of low-symmetry motifs such as tilting, rotations, and B-atom displacements are observed.[119]

Charge-Carrier Mobilities: In 3D LHPs, the atomic orbitals (Pb 6s and I 5p in the valence band maximum; Pb 6p and I 5p in the conduction band minimum) connect three dimensionally. This results in a 3D electronic dimensionality that matches the 3D structural dimensionality (refer to Section 4.1.4). High electronic dimensionality is important for ensuring a small band gap that is suitable for single-junction devices, but is also important for achieving isotropic, high mobilities. The charge-carrier mobility (μ) is a critical factor in semiconductors used for photovoltaics, light-emitting diodes, photoelectrodes, and other applications for which charge transport is critical to operation. This is because the mobility directly affects the diffusion length (in the presence of a chemical potential gradient) and drift length (in the presence of an electric field). The mobility depends on a range of extrinsic and intrinsic factors. The extrinsic factors include grain boundaries, energetic disorder and impurities, and their detrimental effect on mobility can be minimized through careful materials processing.[100] The intrinsic factors, on the other hand, cannot be overcome for a

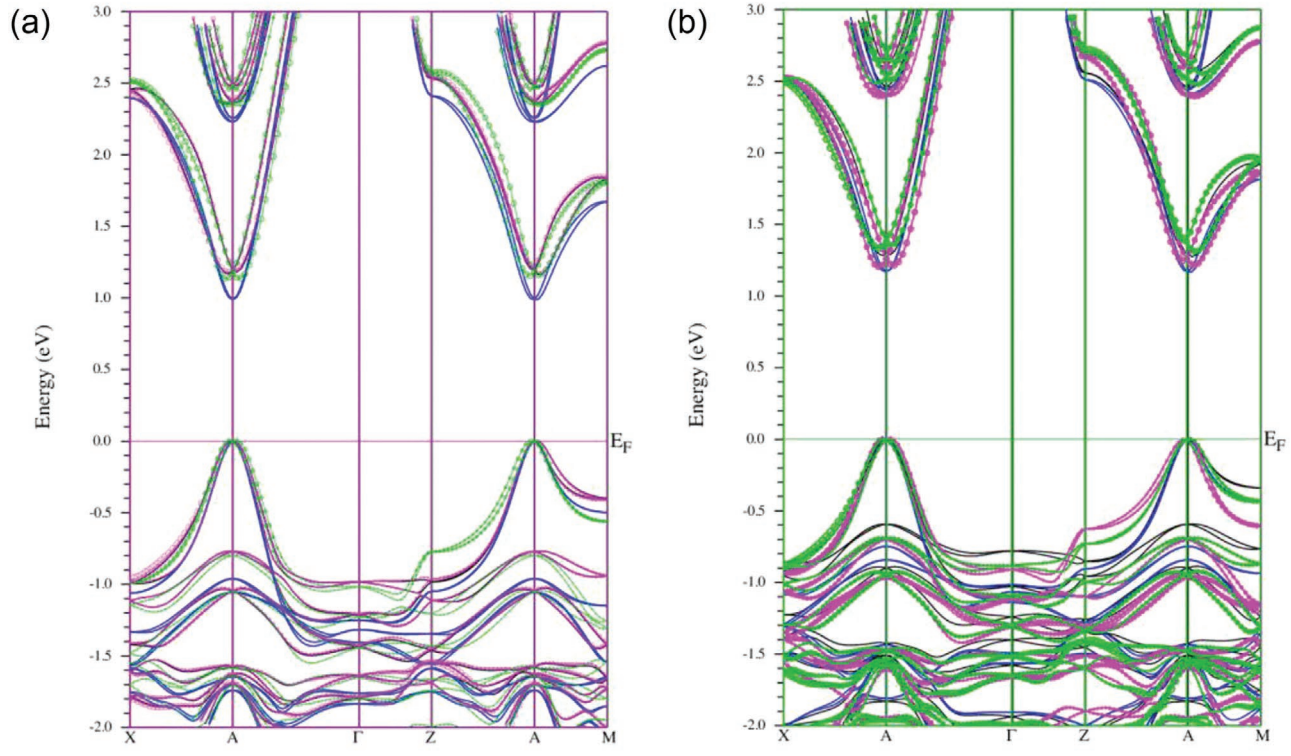

Figure 9. Band structure of a) cubic $Pm\bar{3}m$ and b) tetragonal $P4mm$ $MAPbI_3$ calculated by density functional theory (DFT) that combines the band structures with different MA orientations (represented by the different color lines). Reproduced under the terms of the CC-BY license.[118] Copyright 2019, Springer Nature.

particular material without changing the electronic structure or composition.[100] One of the key intrinsic factors is the carrier effective mass (m^*). This can be seen from Equation (1).[100]

$$\mu = \frac{q\tau}{m^*} \quad (1)$$

Equation (1) gives the Drude model for mobility, which applies when carriers are not affected by scattering by extrinsic factors, and shows the mobility to be inversely proportional to the effective mass of electrons or holes. In Equation (1), q is the fundamental charge and τ the momentum relaxation time.[100] The value of τ could be reduced by carrier-phonon interactions (refer to Section 5).[120] Bulk LHP effective masses have been calculated from first-principles calculations of the band structure,[100,121–124] as well as from experimental techniques, such as magneto-absorption measurements.[125–127] For $MAPbI_3$, the effective masses of holes and electrons are similar, at around 0.1 and 0.2 of the free electron mass (m_0). These values can be tuned by compositional variations, leading to band curvature changes that alter the effective mass, and therefore affect the charge-carrier mobilities.[123,128]

3.1.4. Applications

Despite the extrinsic (e.g., grain boundaries) and intrinsic (e.g., polarons—refer to Section 5) factors that limit charge-carrier mobilities, the mobilities achievable in polycrystalline thin films (in combination with low non-radiative recombination rates) are sufficient for enabling diffusion lengths exceeding a micron.[14] 3D LHPs have therefore been widely used as the absorber layer in planar or meso-superstructured solar cells and have yielded the highest-efficiency halide perovskite devices.[9] Nowadays, laboratory-scale power conversion efficiency values exceed those of multi-crystalline crystalline silicon, and are close to the record efficiency for monocrystalline silicon under 1-sun illumination without concentration.[129] However, bulk LHP solar cells face major challenges that hinder their application. First, LHP PVs have not yet matched the 25- or 30-year lifetime of Si-based technologies, even though encapsulated perovskite devices with more stable compositions than $MAPbI_3$ (e.g., FA-Cs perovskites) have passed industry-standard degradation tests according to the IEC 61215 protocol.[116] Second, most work on LHP photovoltaics is still on the lab scale with device areas <1 cm^2, although there are an increasing number of efforts to manufacture perovskite solar cells at the module scale.[130,131] Third, as the perovskite devices are a stack of different organic and inorganic layers, interfaces between layers play a major role in determining charge transport. Design and modification of interfaces is paramount to enhance the performance of both PVs and LEDs.[17,132] Finally, due to their low exciton binding energies, bulk LHPs are well suited as solar absorbers, but less well suited to achieving efficient performance in LEDs, which benefit from strong coupling between injected electrons and holes. These four key challenges (stability, scalability, interface recombination, and low exciton binding energy), among others, motivate the development of lower dimensional counterparts to improve the suitability of halide perovskites for stable photovoltaics, as well as other optoelectronic applications.

3.2. 2D Perovskites

Pure 2D halide perovskites comprise a monolayer of inorganic corner-sharing lead-halide octahedra sandwiched between organic ligands both above and below the monolayer. By contrast, quasi-2D perovskites have n number of inorganic monolayers between the organic ligands. Thus, increasing the value of n from 1 to ∞ tunes the structural dimensionality of the perovskite from 2D to 3D. In doing so, the band gap (Figure 7b), exciton binding energy, and thermal and environmental stability can be tuned over a wide range. Tuning the dimensionality from pure 3D through quasi-2D, through to 2D is achieved by changing the ratio of the long and short A-site cations, since the long A-site cations act as the ligands sandwiching the inorganic layers.

3.2.1. Crystal Structure

The exploration of lower dimensionality halide perovskites has followed the path taken by the original oxide materials (see Section 2). One of the most widely explored classes of 2D or quasi-2D halide perovskites is the Ruddlesden–Popper (RP) family of perovskites (**Figure 10**a). The general formula is $R_2A_{n-1}Pb_nX_{3n+1}$, where R is the bulky monovalent organic cation that sandwich the inorganic layers, n the number of PbX_6 layers between the R ligands, A is the small A-site cation that can fit within the cuboctahedral voids of the inorganic layers (usually Cs, FA, or MA), and X is a halide. The bulky organic cations used to form the RP phase in LHPs are typically alkyl chains or phenyl groups. Two of the most common R-site cations are

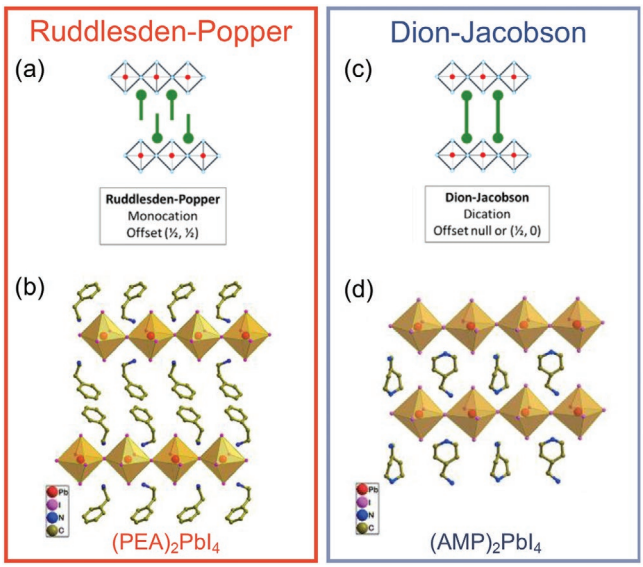

Figure 10. 2D perovskites in the a,b) Ruddlesden–Popper and c,d) Dion–Jacobson phases. a,c) A structural comparison of the two phases. Reproduced with permission.[139] Copyright 2019, American Chemical Society. b,d) Examples of RP and DJ perovskites, in which the R-site cation is PEA (phenethylamine, $C_6H_5C_2H_4NH_3^+$) (b) for the RP phase, and AMP (4- (aminomethyl) piperidinium) (d) for the DJ phase. Reproduced with permission.[134] Copyright 2019, American Chemical Society.

phenylethylammonium (PEA), as shown in Figure 10b, and butylammonium (BA).

Another low-dimensional halide perovskite phase that has been gaining attention is the Dion–Jacobson (DJ) family of perovskites. The key difference between the RP and DJ perovskites is that the DJ perovskites only have one layer of organic cations between the inorganic layers (whereas the RP perovskites have two long organic ligands between the inorganic layers), as illustrated in Figure 10a versus Figure 10c.[133] Furthermore, to maintain charge neutrality, the long-chain cation in DJ perovskites needs to be divalent, whereas in RP perovskites the long-chain cation is monovalent. DJ perovskites can form a stack with either a perfect alignment or a minor displacement depending on the steric demands of the spacer cation.[134] The general formula of DJ perovskites is $RA_{n-1}Pb_nX_{3n+1}$.[133] The most common long-chain R cations used in the DJ perovskites are 4-(aminomethyl)piperidinum (AMP or 4AMP; illustrated in Figure 10d), 3AMP, 1,4-phenylendimethanammonium (PDMA), and others.[135] These low-dimensional perovskites can offer several advantages over their 3D counterparts, in terms of improved environmental stability, increased exciton binding energy, and tunability in the band gap, but fully harnessing these advantages to achieve more efficient and stable solar cells and LEDs requires an understanding of how dimensionality affects these properties, the trade off with other optoelectronic properties (e.g., mobility), and how the materials can be grown with controlled preferred orientation.[129] Compared to the RP phase, the DJ phase of LHPs has shorter I...I interlayer distances, for example, ≈4.0 Å for (3AMP) $MA_{n-1}Pb_nI_{3n+1}$)[136,137] compared to ≈8.0 Å for the RP perovskite $(BA)_2PbI_4$ ($n = 1$).[137,138]

Structural order is an important parameter in 2D LHPs since it determines the mobility and exciton binding energy, as observed in different examples shown in **Figure 11**. For perovskites with low structural dimensionality, the crystallographic orientation is important since it will determine the diffusion and drift lengths of carriers in the plane connecting the two electrodes.[111] In particular, charge movement in 2D LHPs is restricted between layers, owing to the lower band dispersion between layers than within the planes of the inorganic layers.[103] It is therefore essential to control the preferred orientation, for example, to achieve efficient charge-carrier extraction in photovoltaics. Tsai et al. developed a hot casting deposition method for tuning the preferred orientation of Ruddlesden–Popper perovskites with $n = 4$ ($BA_2MA_3Pb_4I_{13}$), such that films with a (101) preferred orientation (vertically-aligned inorganic layers) gave 12.5%-efficient photovoltaic devices.[140] Importantly, ageing tests showed that encapsulated and unencapsulated Ruddlesden–Popper perovskites demonstrated improved stability over their 3D counterparts, showing the advantage of the RP phase.[140] Another method to grow vertically oriented 2D perovskites, developed by Chen et al., was achieved by the nucleation and growth of a 2D $BA_2MA_3Pb_4I_{13}$ perovskite from the liquid–gas interface to form a solid top-layer with strong vertical orientation.[141] Grazing-incidence wide-angle x-ray scattering (GIWAXS) measurement results showed different degrees of preferential vertical orientation, where the film highly oriented shows the highest power conversion efficiency (Figure 11).

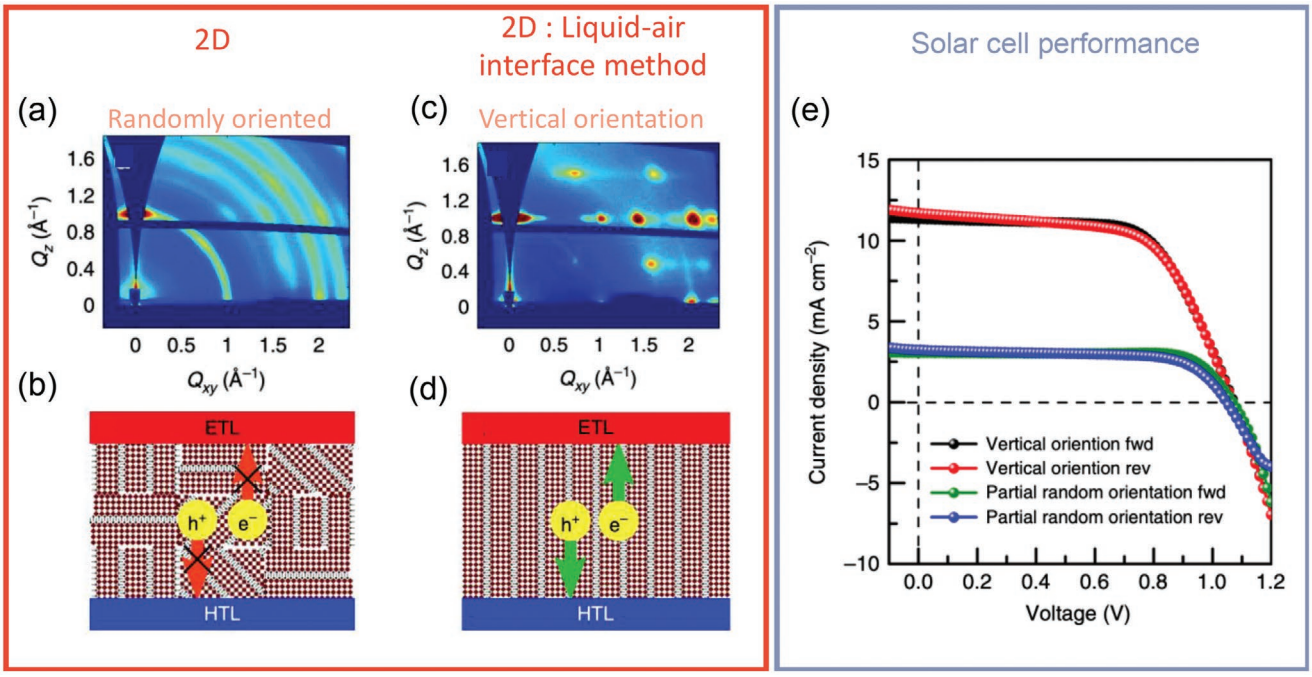

Figure 11. The importance of controlling preferred orientation in solar cells based on RP perovskites. a) grazing incidence wide-angle x-ray scattering (GIWAXS) measurements of 2D perovskite that nucleates in the solvent or solvent/substrate interface and the b) proposed random orientation of the perovskite grains. c) GIWAXS measurements of a 2D perovskite that nucleates from the liquid–air interface, and d) the proposed vertical orientation of the perovskite grains. e) Comparison of the photovoltaic performance of the 2D perovskites with a random versus vertical preferred orientation. Reproduced under the terms of the CC-BY license.[141] Copyright 2018, Springer Nature.

3.2.2. Stability

The replacement of 3D perovskites with 2D analogues has led to enhanced moisture stability due to the hydrophobic side chains of the long chained organic cations.[103,142] For example, Smith et al. used PEA as a moisture barrier for 2D-RP LHP layers, obtaining films that did not decompose over the entire 46-day stability test in ambient air with 52% relative humidity. $MAPbI_3$, by contrast, started degrading to PbI_2 within 4 days under the same conditions.[143] Liao et al. also achieved improved stability over $MAPbI_3$ by using a low-dimensional BA-Cs based RP LHP (where BA is *n*-butylammonium, $C_4H_9NH_3^+$).[144] In general, perovskites with PEA or BA cations exhibit stronger anisotropic absorption and emission, and improved chemical stabilities.[129,145,146] Apart from acting as moisture barriers, these alkylammonium organic cations lack a specific functionality, and do not directly contribute to the optoelectronic properties, other than indirectly through modifying the crystal structure or sometimes by modifying the exciton binding energy (refer to Section 3.2.3).[142] The improvements in environmental stability could be taken advantage of either by using the 2D/quasi-2D LHPs with controlled preferred orientation as the active layer in devices, or by coating 3D perovskites with the 2D/quasi-2D perovskites to protect the underlying 3D perovskite from moisture-induced degradation.

DJ perovskites have also been shown to be more stable than 3D $MAPbI_3$ perovskites. In particular, the stability of DJ perovskites is enhanced by the long-chain R cations being hydrogen bonded on both sides to inorganic layers. In RP perovskites, by contrast, the R cation is only hydrogen bonded to the inorganic lattice on one side. Enhanced structural stability is linked with enhanced device stability. Shang et al. performed density functional theory (DFT) calculations to compare DJ and RP perovskites.[147] 1,4-bis(aminomethyl)benzene (BAB) molecules were used as the bridging ligands for the DJ perovskite, and the typical PEA ligand was used for the RP phase. Firstly, it was found that the distance between the PbI_6 octahedra was shorter for the DJ perovskite (1.15 nm) compared to the RP perovskite (1.65 nm).[147] The binding energy of the long-chain R cation with the inorganic layer was calculated (note: this is not the same as the exciton binding energy), and these results are shown in **Figure 12**a. From these results, it can be seen that the binding energies for the DJ and RP perovskites are very similar, but as discussed earlier, a key difference between these two phases is that the RP perovskite has a dissociation energy that is half of that of the DJ perovskite (Figure 12), owing to the weak van der Waals interactions between the pairs of long-chain organic ligands, whereas the interlayer ligands in DJ perovskites are more strongly bound to the inorganic lattice with hydrogen bonds. This shows the DJ perovskite to be more stable.[147]

3.2.3. Optoelectronic Properties

Excitons: Beyond free electrons and holes, band-edge excitations can also result in coulombically bound electron–hole pairs, which have a neutral charge and behave as quasi-particles known as excitons.[103,148] Excitons are especially prevalent in

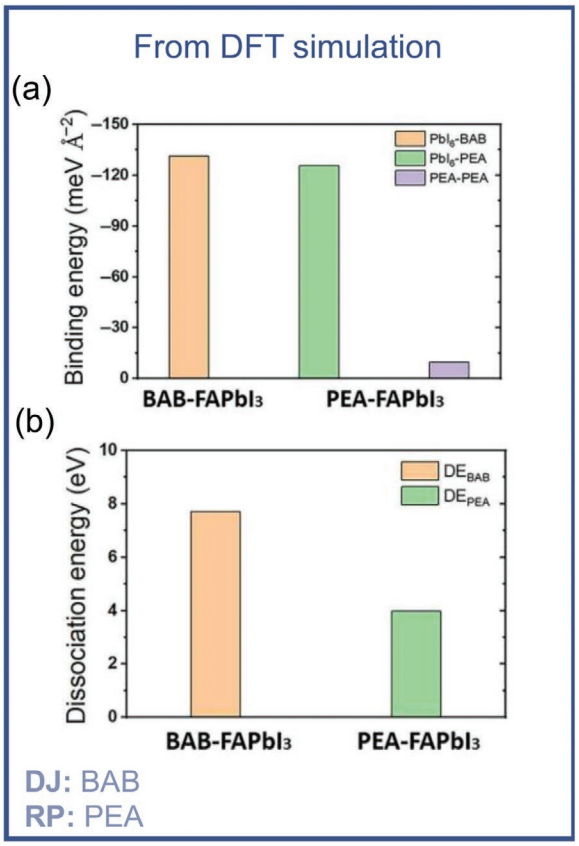

Figure 12. DFT simulations to compare between a Dion–Jacobson (DJ) phase and a Ruddlesden–Popper (RP) 2D perovskite. a) Calculated binding energies between PbI_6-BAB (1,4-bis(aminomethyl)benzene), PbI_6-PEA (phenylethylamine), and PEA-PEA, and the b) calculated molecule dissociation energy of the perovskites based on BAB (DJ phase) and PEA (RP phase). Reproduced with permission.[147] Copyright 2019, The Authors.

low-dimensional perovskites. In photovoltaics and other devices generating current from photon absorption (e.g., photodetectors or radiation detectors), excitons need to be dissociated into free carriers in order to extract the electrons and holes in separate electrodes.[149,150] By contrast, LEDs require electrons and holes to recombine radiatively, and often the injected electrons and holes would first form an exciton.[148] A critical parameter is the exciton binding energy (E_b), which is the difference between the energy of the excitonic state and the electronic band gap of the material.[151] If E_b is comparable to or smaller than kT, the exciton could be readily dissociated to free carriers through thermal energy, and this occurs in 3D LHPs, as well as a range of inorganic materials (e.g., silicon) at room temperature.[126,127,149] While low E_b is desirable for photovoltaics, efficient LEDs often require strategies to increase electron–hole confinement. On the other hand, in materials with high exciton binding energies, photovoltaics require structures (e.g., heterojunctions) that introduce a driving force for exciton dissociation.[150,152] Accounting for the E_b of the active material is therefore critical in designing the optimal device structure for the desired application.

Excitons can be classified as low E_b Wannier–Mott excitons (or free excitons, which are free to move in the crystal) and

high E_b (typically 100 to 1000 meV) Frenkel excitons (which are confined within a unit cell).[103,148,149,153] Wannier–Mott excitons can be described with a hydrogen model, and the E_b can be calculated from Equation (2), in which μ_{ex} is the exciton reduced mass ($1/\mu_{ex} = 1/m_h + 1/m_e$), n is the principal quantum number (i.e., 1st excitonic level, 2nd excitonic level, etc.), m_h the hole effective mass relative to the free electron mass m_0, m_e the electron effective mass relative to the free electron mass m_0, ε_{eff} the effective dielectric constant, and R_y the hydrogen Rydberg constant (13.6 eV).[148,149]

$$E_b = \frac{\mu_{ex}}{n^2 \varepsilon_{eff}^2} R_y \tag{2}$$

In LHPs, Pb and I are heavy elements, which contribute to large dielectric constants of ≈30 (static) and ≈5 (high-frequency).[106,149,154] Although this would lead to lower E_b values if Wannier–Mott excitons were present, high dielectric constants do not guarantee that Frenkel excitons do not occur instead. Furthermore, lowering the dimensionality of the perovskites through the formation of RP or DJ phases, or through quantum confinement in perovskite nanoplatelets, leads to higher E_b values.

Due to their high exciton binding energies, numerous studies into 2D LHPs focus on understanding the exciton characteristics for property tunability and parameter optimization for different applications such as PVs versus LEDs. For example, Li et al. investigated the exciton anisotropy to understand the behavior of excitons in 2D $(BA)_2PbI_4$ RP perovskites through polarization-resolved reflection, and PL and photoconductivity measurements. These showed that there was anisotropy for both free and self-trapped excitons in this system. Notably, they found that free and self-trapped excitons displayed opposite polarization-dependent behavior in the PL and photoconductivity measurements, which was attributed to the optical selection rules for free versus self-trapped excitons being different. These results could contribute to the development of polarization resolved optoelectronic devices.[155]

Further investigations have been made into the role of charge-transfer excitons in 2D LHPs. These excitons are those that form in the interlayer between two adjacent materials with different electronegativities and local energies. Also known as interlayer excitons, they are important to study and understand how to enhance charge transfer between molecules and different heterostructures, which is especially important for improving the performance of solar cells and LEDs.[156,157] Zhang et al. proposed two methods to show the presence of charge-transfer excitons and interface excitons in a heterostructure of two 2D perovskites (PEA_2PbI_4 and PEA_2SnI_4).[156] One method was by mixing two precursor solutions, and the other was introducing a new mechanical "hand-finger pressing method". They show that charge transfer excitons are formed at the PEA_2PbI_4/PEA_2SnI_4 interface and led to a broad, sub-bandgap peak in the photoluminescence spectrum. Transient absorption spectroscopy measurements showed that the charge transfer excitons are rapidly formed within 3 ps and become metastable states. Furthermore, these charge transfer excitons can give rise to sub-bandgap photocurrent and are also formed following charge injection, making them important considerations when optimizing the performance of PVs and LEDs.[156]

Quantum Confinement: The higher exciton binding energies of 2D LHPs compared to 3D LHPs comes from quantum confinement effects, which also affect the band gap. In 2D LHPs, the long-chain R group has a low dielectric constant of ≈2.4, while the inorganic lead-halide octahedra layer has a higher dielectric constant of over 6.[158] The array of inorganic layers sandwiched between organic ligands therefore creates a periodic array of barriers (from the organic ligands) and quantum wells within the inorganic layers (**Figure 13**a). This gives rise to quantum confinement. The exciton binding energy of the low-dimensional perovskite ($E_{b,n}$) can be calculated from Equation (3).[159]

$$E_{b,n} = \left(\frac{2}{\alpha - 1}\right)^2 E_b \tag{3}$$

In Equation (3), α is the dimensionality (3 for 3D; 2 for 2D) and E_b is the exciton binding energy for the bulk 3D, non-confined perovskite.[159,160] It can be seen that a 2D perovskite would have an exciton binding energy four times that of a 3D perovskite.[159] However, in most cases, the exciton binding energy of 2D LHPs is larger than this, usually ranging from 190 to 400 meV for pure 2D LHPs. Furthermore, the exciton binding energy values of quasi-2D perovskites vary with the number of *n*-layers, as well as the length of the organic cation used,[158,161–163] with typical values of approximately 80 meV.[103,142,164–167] This is due to the dielectric confinement effect and occurs when the dielectric constant of the inorganic layer is larger than the dielectric constants of the neighboring organic layer, as occurs in the case of 2D and quasi-2D perovskites. In the inorganic layer, the electrostatic forces between electrons and holes are increased because the electric field lines between the charges extend into the organic layers, where they are less effectively screened, resulting in stronger attraction between the carriers. Larger differences in dielectric constant result in increased exciton binding energy, as well as increases in the electronic band gap owing to larger changes in the energy levels as the electrostatic forces change.[159] Figure 13b illustrates the effect of structural dimensionality, quantum confinement and a combination of quantum and dielectric confinement on the E_b value for the $(decyl\text{-}NH_3)_2PbI_4$ perovskite.

Strategies to Overcome High Exciton Binding Energies: The presence of excitons strongly affects charge carrier transport. If the binding energy is high (>50 meV), the exciton may become localized to a unit cell, that is, becomes a Frenkel exc iton.[148,159,169,170] However, investigations into Ruddlesden–Popper perovskites have mostly concluded that the excitons have Wannier–Mott character, owing to the Bohr radii extending over several unit cells,[153,159] but excitons could also exist in the organic ligands, and these likely have Frenkel character. It has been shown that organic-inorganic hybrid systems can form Frenkel–Wannier hybrid excitons due to the coupling between the Wannier excitons in the inorganic layer and the Frenkel excitons in the surrounding organic layers,[169] and these hybrid excitons have been proposed to occur in lead-based 2D perovskites.[170]

Another strategy to reduce the effects of Frenkel excitons in 2D perovskites involves changes in the perovskite electronic structure by introducing functional organic molecules as strong electron donors or acceptors.[140] The work done by

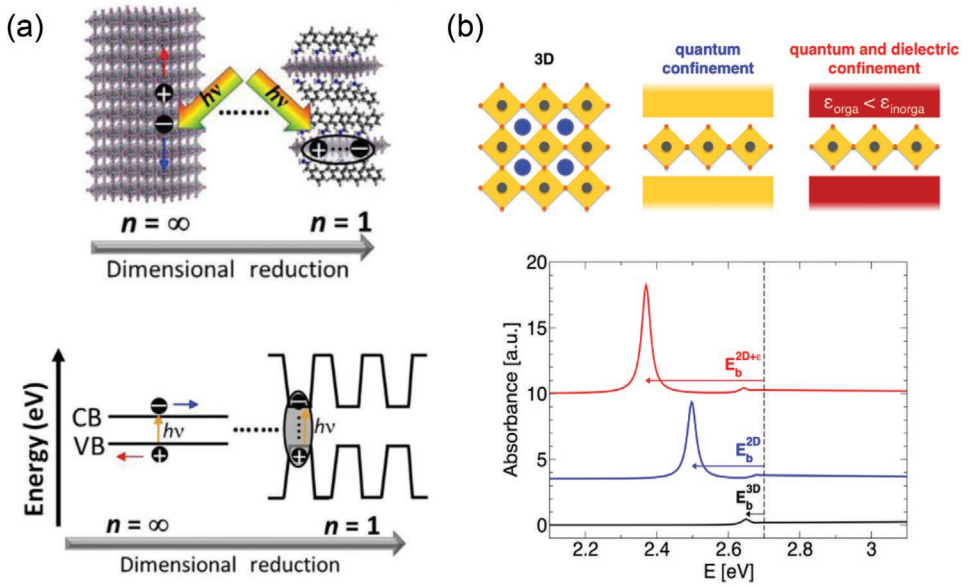

Figure 13. The role of dimensionality on confinement effects. a) How dimensionality (different n values) affects the generation and recombination of charge carriers and the corresponding energy bands scheme for $n = \infty$ (3D perovskites) and $n = 1$ (2D perovskites) to illustrate the effect of quantum confinement in the dissociation (3D) or binding (2D) of the electron hole pair. Reproduced with permission.[129] Copyright 2020, American Chemical Society. b) Schematic of the hypothetical 3D (decyl-NH_3)$_2$$PbI_4$ perovskite (black), 2D perovskite with only quantum confinement (blue) and 2D perovskite with quantum dielectric confinement (red) with its corresponding optical absorption calculated using a k.p/BSE approach. Reproduced with permission.[168] Copyright 2016, American Chemical Society.

Gelvez-Rueda et al. achieved efficient charge separation in quantum and dielectrically confined 2D perovskite materials by incorporating a strongly electron accepting moiety of perylene diimide organic chromophores on the surface of a bi-layered lead bromide-based perovskite nanoplatelet.[140] This strategy presented a possible method to achieve efficient formation of mobile free charge carriers. Carrier lifetimes were improved to tens of microseconds, which is two orders of magnitude longer than without the organic moiety.[140]

Band Gap: RP and DJ perovskites have the advantage of band gap tunability through not only the composition but also the structural dimensionality.[129] 2D LHPs exhibit larger optical band gaps compared to the 3D LHPs (Figure 7b), due to quantum confinement effects, as explained above.[103,110,111,153,171] Furthermore, the band gap of a single layered perovskite ($n = 1$) can be tuned by controlling the interlayer spacing and the structural distortion in the perovskite layer.[111,142,172,173] The interlayer spacing can be modified by increasing or decreasing the length of the organic molecular cation R, in which an increase in cation length will lead to wider band gaps.[111] For this reason, since DJ perovskites have lower interlayer spacing, they have also demonstrated narrower band gap than the RP phases.[137] In iodide-based RP perovskites, the band gap can be modulated from 1.59 to 2.36 eV by controlling the number of inorganic layers between the organic ligands (i.e., the n value), as shown in **Figure 14**.[129,158,174] For example, Cho et al. showed that the band gap of PEA-MA RP perovskites blue-shifted when the ratio of PEA:MA increased and the parameter n decreased (Figure 14a).[129] Similar results were obtained with BA-MA RP perovskites (Figure 14b),[138] as well as with DJ perovskites (Figure 14c,d).[172,175] Moreover, theoretical studies by ab initio molecular dynamics (AIMD) calculated the dynamic electronic structures in 2D perovskites.[137] It was shown that the DJ phase (3AMP) has a lower band gap than the RP phase and with a narrower distribution in the VBM and CBM (Figure 14e). The narrower distribution in band-edge positions is due to reduced thermal broadening, and this is attributed to a higher equatorial Pb-I-Pb angle in the DJ phase which makes the PbI_6 octahedra less distorted, causing a red-shift in the electronic band gap. Less distortion also leads to less thermal motions. This was shown by calculating and comparing the thermal broadening in the VBM and CBM between the RP and DJ phases (Figure 14f).[137]

3.2.4. Applications

In photovoltaics, the power conversion efficiency of RP perovskites has increased from 4.74% in 2014 to 18% in 2020. This rapid progress has been achieved through band gap optimization, controlling the preferred orientation, compositional engineering, and through the optimal use of mixed phases (detailed in Section 3.3). Moreover, DJ perovskites have recently attracted increasing attention for applications in photovoltaics due to their improved phase stability and electronic properties over RP perovskites. Record efficiency values of RP and DJ are similar; however, a steeper increase is observed for the new DJ-phase as shown in **Figure 15**a.[135] In addition, Ahmad et al. found that while RP perovskites (PA-MA, $n = 4$) exhibited improved environmental, thermal, and photostability than 3D $MAPbI_3$ perovskites in solar cells, DJ perovskites (PDA-MA, $n = 4$) demonstrated a further improvement in stability, as shown in Figure 15c–f.[175]

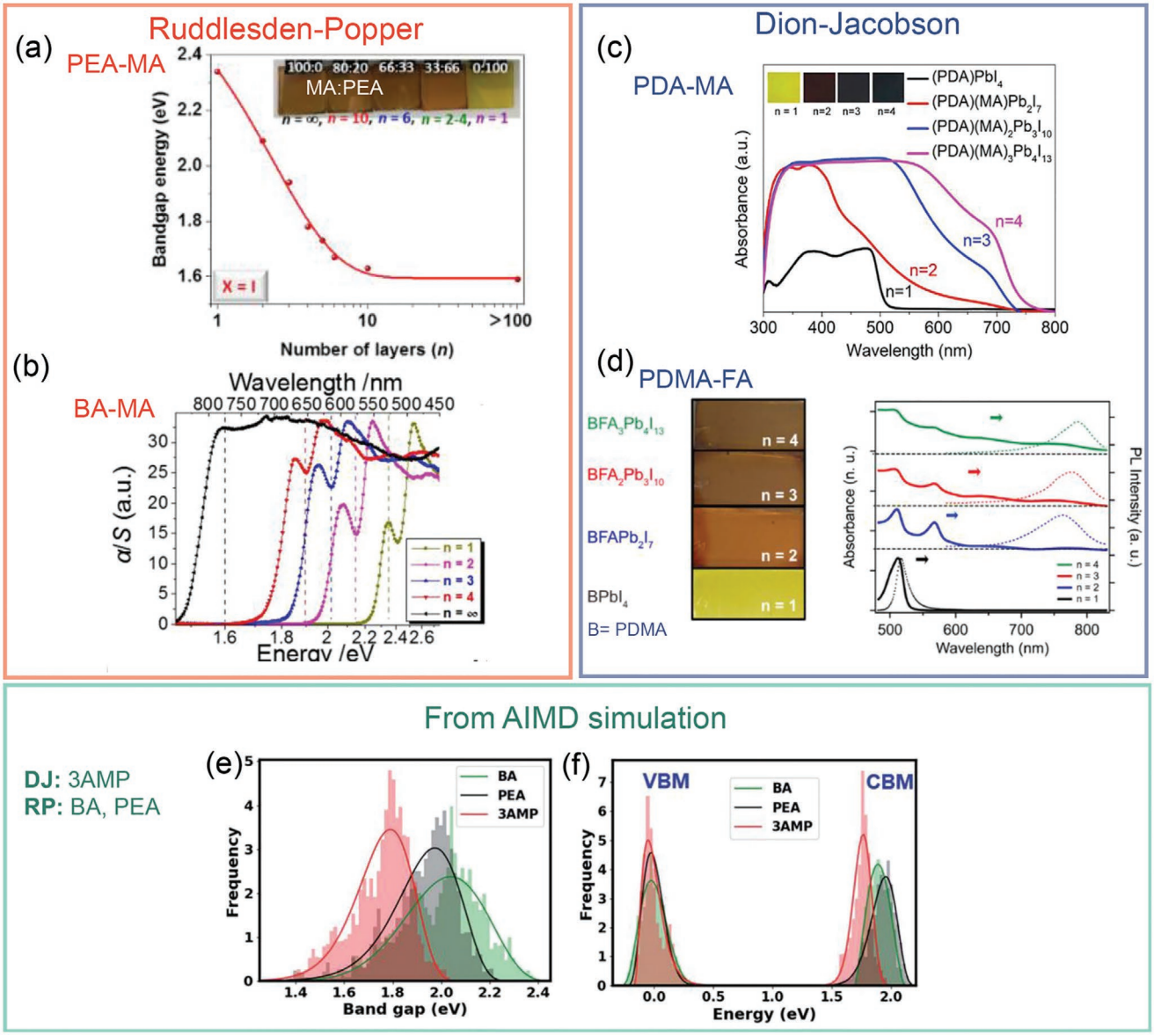

Figure 14. Effect of dimensionality, *n*, on the band gap of RP and DJ perovskites. a) $(PEA)_2(MA)_{n-1}Pb_nI_{3n+1}$ and b) $(BA)_2(MA)_{n-1}Pb_nI_{3n+1}$. a) Reproduced with permission.[129] Copyright 2020, American Chemical Society. b) Reproduced with permission.[138] Copyright 2016, American Chemical Society. Note that in part (b), the band gap was determined from diffuse reflectance measurements converted with the Kubelka–Munk function, in which $\alpha/S = (1-R)^2/(2R)$. Effect of dimensionality on the band gap of DJ perovskites (c) $(PDA)(MA)_{n-1}Pb_nI_{3n+1}$ and (d) $(PDMA)(FA)_{n-1}Pb_nI_{3n+1}$. c) Reproduced with permission.[175] Copyright 2019, Cell Press. d) Reproduced with permission.[172] Copyright 2019, American Chemical Society. All inset panels of (a,c,d) show photographs of films for the different *n* values. e,f) Theoretical comparison of band gaps through ab initio molecular dynamics (AIMD) calculations of the dynamic electronic structures of the 2D-perovskites RP: $(BA)_2PbI_4$, $(PEA)_2PbI_4$, and DJ: $(3AMP)PbI_4$. e) The histogram distribution of band gaps along the AIMD trajectories, and f) the thermal broadening in the VBM and CBM states. Reproduced with permission.[137] Copyright 2020, Royal Society of Chemistry.

3.3. Multi-Dimensional Perovskites

Multi-dimensional perovskites refer to thin films that incorporate a mixture of different dimensionalities, for example, Ruddlesden–Popper perovskites with different *n* values mixed together. This can be achieved by mixing all phases together into the bulk of the thin film, or by having perovskites of a different dimensionality only at surfaces and interfaces. The mixture of different phases could either be random or ordered (**Figure 16**). In the latter case, the 2D LHP layer when mixed with 3D phases can form an interspersed layered structure,[171,176] as shown in Figure 16a, as a lower dimensional capping layer on the surface of the perovskite thin film (Figure 16b), or as an interface passivation layer (Figure 16e).[171] For example, 2D LHPs have been used to create a moisture-barrier on the surfaces of 3D bulk perovskites as capping layers (Figure 16b), as well as to passivate the interface with the hole/electron transport layer (Figure 16e). PEA and BA have been the most popular long-chain R cations used to form multidimensional 2D-3D structures for the Ruddlesden–Popper hybrid perovskites.[171]

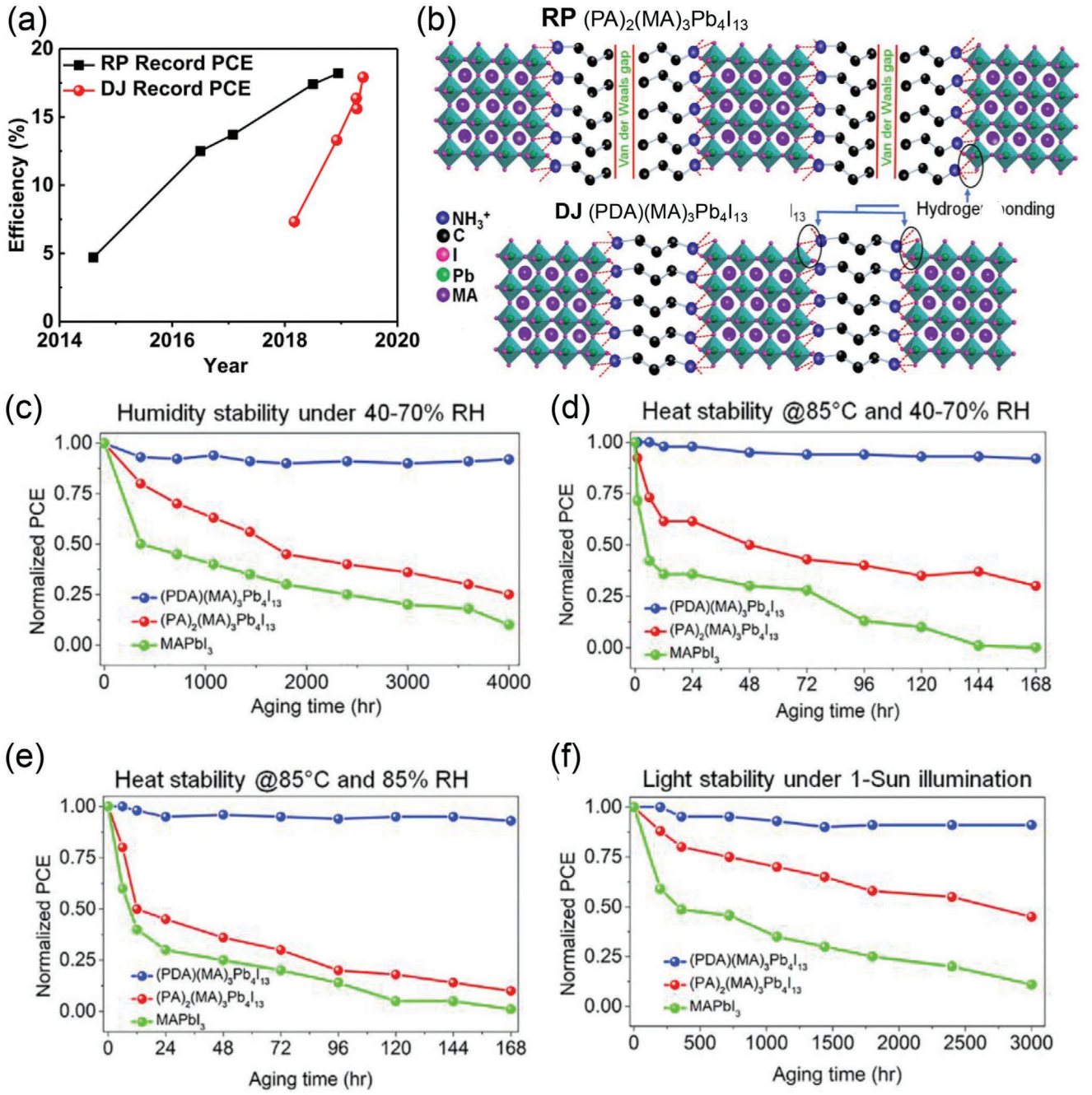

Figure 15. Comparison of Ruddlesden–Popper (RP) versus Dion–Jacobson (DJ) perovskites in solar cells and their power conversion efficiency (PCE). a) Evolution of the record PCE for layered RP and DJ perovskite solar cells. Reproduced with permission.[135] Copyright 2019, American Chemical Society. b) Schematic illustration of the RP $(PA)_2(MA)_3Pb_4I_{13}$ (n = 4), and DJ $(PDA)(MA)_3Pb_4I_{13}$ (n = 4) perovskites. The performance of these perovskites in solar cells is given in (c–f). Stability test of RP, DJ, and 3D $MAPbI_3$ perovskite-based devices in c) ambient air, d) under damp heat stress (85 °C, 40–70% RH), e) under damp heat stress (85 °C, 85% RH), f) under 1-sun illumination. Reproduced with permission.[175] Copyright 2019, Cell Press.

3.3.1. Stability

By forming a "capping layer" of 2D LHP on a 3D LHP bulk, as shown in Figure 16b, the environmental stability can be improved.[171] In 2017, Grancini et al. fabricated 3D $MAPbI_3$ films where the surface was capped by a 2D perovskite synthesized using aminovaleric acid iodide $HOOC(CH_2)_4NH_3PbI_4$ (AVAI).[177] To analyze the effect of the 3D/2D interface on the electronic properties, they used first principles calculations to determine the local density of states (Figure 16c). From the calculations, they observed that the formation of the mixed 3D/2D perovskite widened the band gap of the 3D material in the interface region, which could form a barrier to reduce electron recombination. Solar

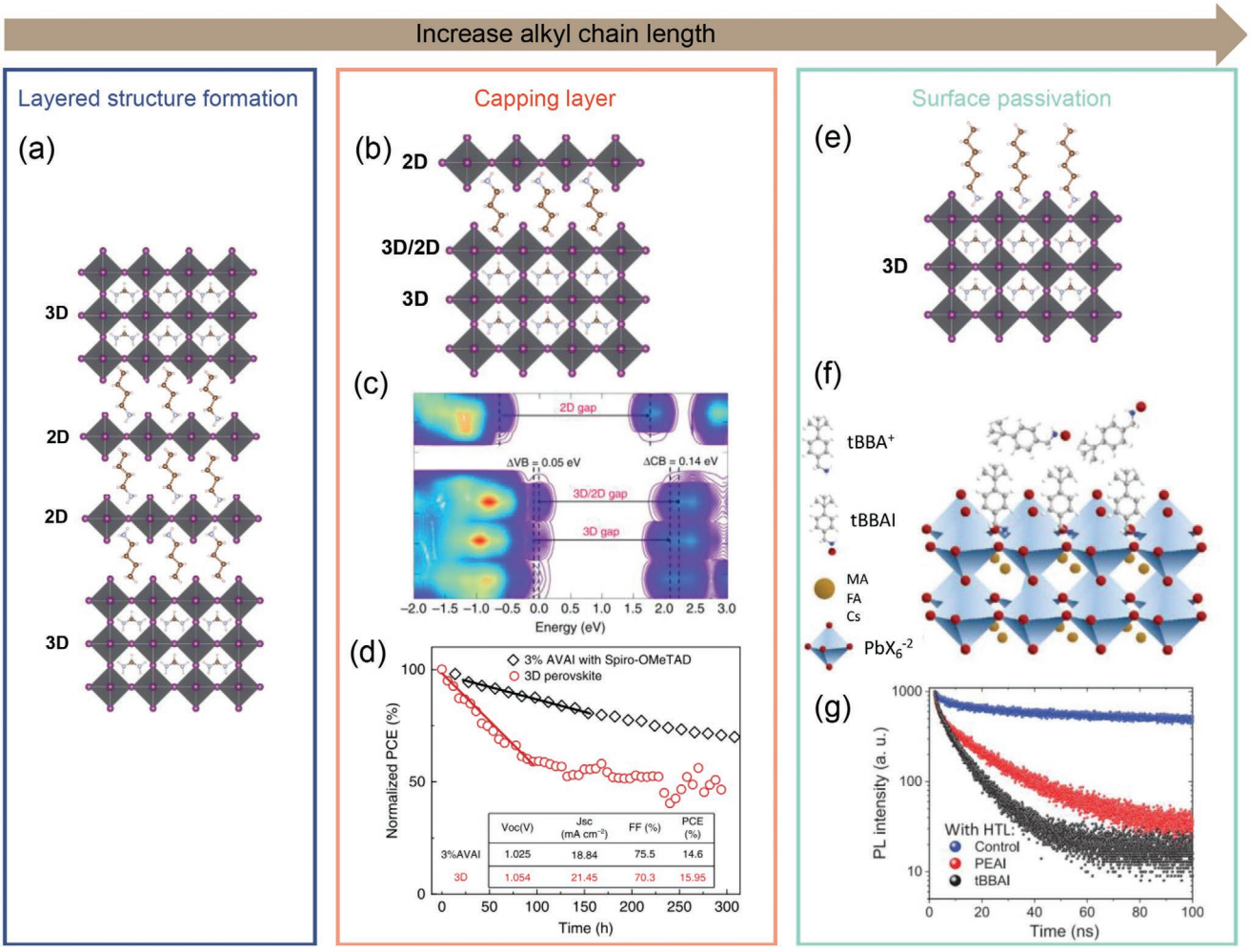

Figure 16. Mixing 2D–3D perovskites to for a) layered structured formation with randomly positioned 2D and 3D domains, b) capping layer mode with a 2D structure on top of the 3D perovskite domain, and an example of c) local density of states (DOS) of the 3D/2D interface in the work by Grancini et al.[177] and its corresponding d) normalized PCE as a function of time for the 2D-3D perovskite with AVAI with spiro-OMeTAD (black) versus the 3D perovskite (red). Reproduced under the terms of the CC-BY license.[177] Copyright 2017, Springer Nature. e) Surface passivation mode of 2D–3D multidimensional perovskite with an example of structure for f) perovskite structure passivated by tBBAI, and the corresponding g) time-resolved photoluminescence for the layer structure glass/FTO/mp-Al_2O_3/perovskite/without surface layer (control, blue), with PEAI (red), and tBBAI (black). Reproduced under the terms of the CC-BY license.[180] Copyright 2020, Wiley. Schematic and categories on three types of mixed dimensioned perovskites reproduced under the terms of the CC-BY license.[171] Copyright 2018, Springer Nature. Reproduced with permission.[181] Copyright 2020, Royal Society of Chemistry.

cells with this 3D/2D perovskite were fabricated in two architectures: 1) devices with a carbon-based top electrode, which had a maximum of 12.9% power conversion efficiency, and 2) standard mesoporous n-i-p structure with 14.6% power conversion efficiency. The power conversion efficiency of the 3D/2D fabricated devices was lower than the pristine 3D; however, the multidimensional perovskites were more stable (Figure 16d). In addition, the carbon-based architecture was scaled up to a 10 × 10 cm^2 module, where no performance losses were seen after 10 000 h. Ma et al. also demonstrated an improvement in device stability by capping the 3D $MAPbI_{3-x}Cl_x$ with an organic layer of cyclopropylammonium iodide (CAI) on top (i.e., CA_2PbI_4/ $MAPbI_{3-x}Cl_x$).[178] The hybrid composition was stable for 40 days compared to 8 days of the pristine 3D material.[178]

3.3.2. Surface Passivation

Even if bulk LHPs are defect-tolerant, the surface is the place where defects are easily formed, and passivating these defects has been shown to be essential to achieve the highest efficiencies in solar cells or LEDs.[179] For example, Jiang et al. used an organic halide salt of PEAI on FA-MA LHP thin films.[179] The PEAI formed on the perovskite surface, enhancing the power conversion efficiency of solar cell devices up to 23.32%. The authors found that adding the PEAI layer improved the charge-carrier lifetime (from transient photovoltage and photocurrent measurements) from 8.8 µs (control) to 138.8 µs (PEAI).[179] 4-tert-butyl-benzylammonium iodide (tBBAI) was also investigated as a passivating agent for the surface of perovskite thin films, as illustrated in Figure 16f.[180] Using tBBAI led to a

substantial increase in the PL lifetime (Figure 16g). The reduction in non-radiative recombination compared to the control sample was greater than achieved when using PEAI as the passivation agent (Figure 16g). Furthermore, tBBAI was found to improve charge extraction from the perovskite to the hole transport layer (spiro-OMeTAD), and this led to the power conversion efficiency increasing from ≈20% (no tBBAI) to 23.5% (with tBBAI).[180] In a separate work, Yoo et al. introduced a "selective precursor dissolution" strategy to deposit a 2D perovskite capping layer on the 3D perovskite without disrupting the lattice structure of the 3D phase.[10] This was achieved by depositing linear alkyl ammonium bromides dissolved in chloroform on the 3D perovskite film. With the capping layer, the charge-carrier lifetime was prolonged, and V_{OC} increased. Certified 23.4%-efficient solar cells were thus achieved. In general, amine additives have been proven to be effective in passivating crystallographic defects and increase power conversion efficiencies in solar cells. The length of the linear alkyl chain core is a critical factor that determines the effectiveness in passivating surface defects, as demonstrated by Feng et al.[181] It is proposed that the alkyl chain length is correlated to its function and passivation role as shown overall in Figure 16.

3.4. Perovskite Nanocrystals, Quantum Dots, and Nanoplatelets

As discussed in the introduction, dimensionality refers to both the dimensionality in the crystal structure and the form factor of the materials. The structural dimensionality of 3D ABX_3 perovskites can be reduced to 1D and 0D lead-halide perovskites, but investigations into these materials have been limited compared to the other dimensionalities. Recent works on structurally 1D[182–184] and 0D[185–188] lead-halide perovskites have certainly shown their importance and capability in broadening the range of possible applications, but in this section, we will mainly focus on the effects of decreasing the size of the materials on the properties of the perovskite, that is, we will primarily focus on form factor dimensionality. The strong processing versatility of LHPs extends beyond thin films to nanocrystals (NCs), which are nanometer-sized particles typically on the order of 20 nm or smaller. Since the early demonstration of colloidally grown LHP nanocrystals in 2012–2014,[189–191] the research field focusing on this area has grown exponentially owing to the new features enabled by reducing the crystal size to the nanoscale, and the opportunities opened up.[192] These include tuning the band gap and exciton binding energy through the size of the nanocrystals, as well as a wide range of routes to passivate the surfaces to achieve near-unity PLQEs. LHP nanocrystals include 3D nanocubes, 2D nanoplatelets (NPls), 1D nanowires (NWs), and 0D quantum dots (QDs). While nanocubes have sizes larger than the Bohr radius, nanoplatelets, nanowires, and quantum dots have 1, 2, and 3 dimensions, respectively, smaller than the Bohr radius (7 nm for $CsPbBr_3$ and 6–12 nm for $CsPbI_3$)[190,193,194] and exhibit quantum confinement. As an example, the effect of the number of inorganic monolayers in 2D perovskite NPls on the band gap and PL peak position is shown in **Figure 17**, in which L represents the long-chain ligand (e.g., oleylamine and oleic acid) used to arrest growth along the thickness axis.[195] The crystal structure of perovskite nanocrystal materials is typically cubic

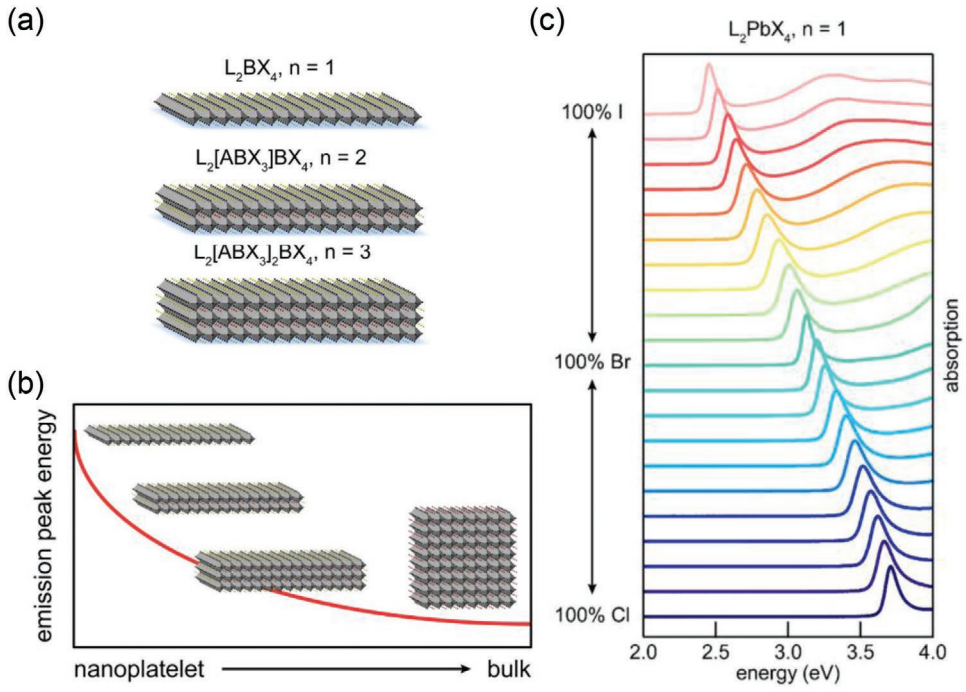

Figure 17. LHP nanoplatelet properties. a) Schematic of the nanoplatelet structure for different thicknesses (*n*-layers), b) correlation between the emission peak energy and the thickness of the nanoplatelet until it becomes a bulk perovskite. c) UV–vis absorption spectroscopy of the L_2PbX4 ($n = 1$) in toluene showing emission tunability as a function of the halide mixture composition (X = I, Br, Cl). a,b) Reproduced with permission.[195] Copyright 2017, American Chemical Society. c) Reproduced with permission.[449] Copyright 2016, American Chemical Society.

or orthorhombic. As with bulk perovskites, the perovskite phase could only be stabilized using smaller A-site cations (e.g., MA, FA, and Cs), according to the Goldschmidt tolerance factor.[110] Due to the high ionic bonding in LHPs, NCs can form rapidly at room temperature from a wide variety of precursors.[110,196,197] The form factor dimensionality can be simply tuned through the precursors used and their ratio. More details on LHP nanoplatelet properties and applications can be found in refs. [191,195] and [198].

3.4.1. Optoelectronic Properties

In many ways, LHP NCs demonstrate superior optoelectronic properties compared to their bulk counterparts,[199] due to: 1) the versatility of colloidal chemistry which allows the stabilization of cubic or orthorhombic phases at room temperature for a wider range of materials, including compounds that have high formation energies and are metastable at room temperature;[35,200] 2) the passivation of surface defects with a wide range of possible ligands, thus giving rise to substantial increases in the PLQE that can reach up to 100%;[192] and 3) the surface ligand layer surrounding individual NCs that can block ionic diffusion to improve the stability upon applied bias. The lattice of QDs also has a high plasticity, which enables anion and cation exchange, where the A-site can by partially or fully exchanged.[110] In contrast to structurally 3D QDs, the crystal structure of 0D non-perovskites, such as Cs_4PbBr_6, is resistant to anion exchange due to the inaccessibility of the isolated $[PbBr_6]^{4-}$ octahedron.[186]

Beyond simply being able to tune the band gap through the composition, the band gap can also be tuned through the size of the nanocrystals as well as the ligands used, that is, by a combination of quantum and dielectric confinement.[201–205] This allows the band gap to be blue-shifted while avoiding the challenges when changing the halide composition, namely phase-segregation under illumination (e.g., with I-Br perovskites) or the introduction of deep traps when alloying Cl into Br-based perovskites.[36,193,206–208] For example, with perovskite nanoplatelets, it is possible to tune the thickness down to a monolayer (Figure 17a), thus blue-shifting the PL of green-emitting $CsPbBr_3$ nanocubes to the deep-blue ($\lambda < 450$ nm), while maintaining high PLQEs.[195] Combined with the passivation of the NPl surfaces, substantially higher PLQEs >50% can be achieved for blue-emitting pure-bromide perovskites, whereas blue-emitting Cl-Br perovskite nanocrystals have PLQEs <10% reported.[36,193,198,209–211] Equally, 1D perovskite nanowires are widely considered to be effective nanomaterials due to their remarkable optoelectronic properties.[184] Zhu et al. found that these 1D nanowires have higher absorption coefficients than their counterpart 3D $MAPbI_3$ perovskites.[212] They found that nanowires can significantly increase the optical path length and therefore also increase the absorption of light.

3.4.2. Stability

Despite their outstanding optoelectronic properties, there are still challenges in the stability of perovskite NCs to environmental factors, such as air, moisture, temperature, and light.[195] 1D lead-halide perovskites have shown improved ambient stability compared to their analogous 3D counterparts.[212] Superior stability is attributed to a higher crystalline structure, unique 1D enclosing surfaces, and fewer grain boundaries. In addition, LHP NCs have low mobilities because of the use of long-chain insulating ligands.[213] Challenges also arise in the colloidal stability of nanoplatelets, nanosheets, and nanowires which can be fully stable in solution after synthesis but easily revert to cuboidal or irregular shapes, or recrystallize to the bulk material, after isolation and purification. For example, perovskite nanowires have only been found to be satisfactorily durable when their diameter is between 10–200 nm. Growing nanowires or other types of nanocrystals with sizes <10 nm and which are stable has been challenging for halide perovskites.[110] The use of polymer encapsulation has been found to be effective in stabilizing some NCs in colloidal solution, and has therefore been proposed for the stabilization of perovskite NPls.[195] There are numerous other strategies to improve the stability of perovskite nanocrystals, and these include compositional engineering, surface engineering (by designing organic ligands that can more effectively bind to the surface to stabilize the NCs),[202] as well as the encapsulation of the perovskite NCs in a matrix of a stable material (e.g., glass matrices).[214]

3.4.3. Surface Ligands

There has been significant work on engineering the surface ligands as a strategy to improve stability and achieve improved efficiencies in PV/LED devices. Conventionally used oleylamine ligands result in low electrical conductivity and stability of perovskite NCs because of the long carbon chain, absence of conjugated bonds, and weak interactions with the surface of the LHP NCs.[213] As a result, there has been extensive work on developing alternative ligands, and some of the important properties are the length of the organic chain in the ligands and its bulkiness.[213] It was shown that quaternary ammonium bromide (QAB) ligands surrounded the surface of NCs more effectively than oleylamine, resulting in improved surface passivation. However, the effectiveness of these QAB ligands depended on its bulkiness: dioctyldimethyl, methyltrioctyl, and tetraoctyl ammonium bromide ligands were compared. The less bulky, dioctyldimethyl ammonium bromide (DOAB) showed improved optical properties and environmental stability, as shown in **Figure 18**a-i. However, bulky cations, such as tetraoctyl ammonium bromide (TeOAB), had worse performance than oleylamine (Figure 18a -ii). Less aggregation for the DOAB was also observed compared to bulky quaternary ammonium bromide ligands. Furthermore, it was found that the electrical properties of $CsPbBr_3$ NCs could be improved by tuning the chain length of these new ligands for a higher and balanced charge-carrier transport.[213] Kumar et al. investigated the effect of the hydrophobicity of the coordinating ligands on the performance of $FA_{0.5}MA_{0.5}PbBr_3$ NCs in LEDs.[199] The authors found that by increasing the hydrophobicity of the primary alkylamine ligands used in the synthesis of the NCs, they achieved a higher degree of quantum confinement by reducing the size of the NCs. Furthermore, a combination of a reduction

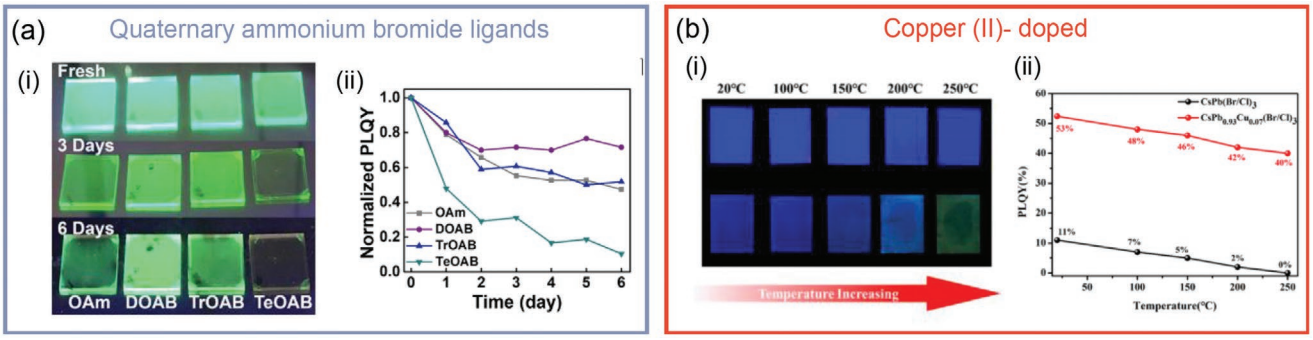

Figure 18. LHP NC and quantum dot stabilization methods by a) surface ligand engineering by quaternary ammonium bromide ligands with different bulkiness where OAm: oleylamine ligands, DOAB: dioctyldimethylammonium bromide, TrOAB: trioctylammonium bromide, TeOAB: tetraoctylammonium bromide. i) Photograph showing the green PL emission of $CsPbBr_3$ LHP NCs while being kept in air with relative humidity up to 60%, and ii) PLQEs of $CsPbBr_3$ NCs dispersed in hexane recorded as a function of time while being kept in air. Reproduced with permission.[213] Copyright 2019, American Chemical Society. b) Copper (II)-doped Cs LHPs QDs as a stabilization method: i) photographs showing blue emission when changing color with annealing temperature and ii) PLQEs of $CsPb_{0.93}Cu_{0.07}(Br/Cl)_3$ in red and $CsPb(Br/Cl)_3$ in black as a function of annealing temperature. Reproduced with permission.[215] Copyright 2019, American Chemical Society.

in NC size along with the dielectric confinement effect induced by the use of low-dielectric-constant ligands resulted in shorter exciton lifetimes that led to increased PLQEs, as well as lower refractive indices in NC thin films that enabled improved light outcoupling efficiency. Through ligand engineering, they fabricated a high-performance green LED with a maximum external quantum efficiency of 16.2%. In line with material modification for enhanced stability, Bi et al. doped mixed halide LHP QDs with divalent Cu^{2+} ions into the perovskite lattice to form $CsPb_{1-x}Cu_xX_3$ QDs.[215] Their measurements revealed that doping smaller Cu^{2+} guest ions induced a lattice contraction that eliminated halide vacancies, leading to increased lattice formation energy and improved short-range order of the doped perovskite QDs. In addition, an improvement in thermal stability was observed (Figure 18b), leading to blue emission with PLQEs reaching 80%. Recently, Dong et al. reported a surface treatment to stabilize $CsPbBr_3$ perovskite QDs by creating a bipolar QD shell.[216] This layer consisted of an inner anion layer and an outer layer of cations and polar solvent molecules. With this strategy, it was possible to achieve strongly confined QDs for improved carrier mobility, and trap density reduction compared to other low-dimensional perovskites. With the surface strategy, they fabricated blue-emitting LHP QD films with PLQEs exceeding 90%, and efficient $CsPbBr_3$ blue and green LEDs (12.3% and 22% external quantum efficiency, respectively).[216]

Fundamental studies have given important insights into how the interactions between surface ligands and NCs could lead to improved properties. Wheeler et al. used spectroscopic techniques to understand at a molecular level the surface chemistry ligand-exchange procedures in the synthesis of $CsPbI_3$ QDs,[217] which have been used in solar cells and LEDs.[218,219] A two-step solid state QD ligand exchange occurs. In this study of anionic (oleate) and cationic (oleylammonium) ligands, they first found that atmospheric moisture could aid the ligand-exchange process by the hydrolysis of methyl acetate, generating acetic acid and methanol. This acetic acid produced, then removed the oleate ligands, forming a QD surface that was bound to acetate and free of oleic acid. Second, they used formamidinium iodide (FAI) in ethyl acetate to remove the long oleylammonium ligands, which is important for improved performance in solar cells. Furthermore, Yoshimura et al. observed an in situ emission of a single $CsPbX_3$ (X = I, Br) QDs during the anion-exchange reaction, which is a unique strategy to control the band gap.[220] They performed photon-correlation measurements for the single NCs, and for the mixed halide NCs, which exhibited single-photon emission (photoluminescence spectrum of a single peak). These results suggested that mixed-halide NCs do not form any emission sites with different band gap energies, but rather form a uniform band gap as a result of quantum confinement. Utzat et al. synthesized individual colloidal LHP QDs with a highly efficient single-photon emission with long optical coherence times and large radiative lifetimes.[221] Different to other colloidal QD materials, LHP QDs could be used as building blocks in single photon sources, and present a low-cost and scalable alternative for quantum emitters. Their results show basic understanding of LHP QD design for fast emission, wide spectral tunability, and scalable production, which is a starting point for the application of LHPs as quantum emitters.[221]

3.4.4. Applications

LHPs overall, for all dimensionalities, have been shown to be ideal candidates for two major applications: solar cells and LEDs. In particular, LHP NCs have shown improved phase stability compared to bulk perovskites due to a reduction in the surface strain for smaller NCs.[222,223] NC perovskite solar cells, QDs in particular, have emerged as a new technology. In 2015, Mali et al. fabricated a $MAPbBr_3$ NC-based solar cell with a power conversion efficiency of 11.4%.[224] These devices were stable for up to 4 months. Later in 2016, Swarnkar et al. showed the phase stabilization of α-phase $CsPbI_3$ QDs, used for solar cells with a power conversion efficiency of 10.77%.[218] By contrast, $CsPbI_3$ cannot be stabilized in the perovskite phase at room temperature owing to the low Goldschmidt tolerance factor. $Cs_{1-x}FA_xPbI_3$ QDs have also recently been demonstrated in solar cells and achieved a power conversion efficiency of

16.6% by using an oleic acid ligand-assisted cation exchange strategy.[223,225] These devices were the certified highest-efficiency solar cells made from any quantum dot absorber in 2019.[9] The rapid increase in solar cell efficiency shows the importance of LHP QDs and their potential for photovoltaics. Detailed reviews on perovskite NCs for solar cells can be found in ref. [223,226].

Beyond the success of LHP in photovoltaics, LHPs have also shown great potential for other optoelectronic applications.[227] In particular, LHP nanoplatelets have recently gained substantial attention for LEDs, particularly blue LEDs, as discussed earlier in Section 3.4.1. It is more difficult to achieve perovskite QDs that are small enough to achieve similar blue-shifts in emission, while having similarly low polydispersity and high stability. In addition, it has been shown that the surface of perovskite nanoplatelets can be passivated to achieve near unity PLQEs.[198,228] However, a challenge with perovskite nanoplatelets is the anisotropic transition dipole moments, which necessitate careful orientation of the nanoplatelets to avoid limiting the outcoupling of the light generated.[201,229] By controlling the orientation of the perovskite NPls in thin films so that they were *c*-axis oriented (i.e., with the nanoplatelets lying face-down on the substrate), Cui et al. achieved optical transition dipole moments with an 84% contribution from the horizontal component. This led to an enhancement in the outcoupling, and the perovskite LEDs achieved an EQE of 23.6%, which was the highest for LHP LEDs at the time of publication in 2020.[230]

4. Electronic and Structural Dimensionality in Lead-Free Perovskite-Inspired Materials

Lead-halide perovskites defy conventional wisdom, in that they can achieve low non-radiative recombination rates and low open-circuit voltage losses in photovoltaic devices despite high defect densities of 10^{14}–10^{16} cm^{-3} in polycrystalline thin films.[107] By contrast, GaAs and silicon used in electronics have defect densities on the order of 10^{7}–10^{8} cm^{-3}.[107,231] This has prompted the question of whether such defect tolerance could be found in alternative classes of lead-free materials, or "perovskite-inspired" materials. The search for such materials could not only give rise to new insights into defect tolerance, but also yield defect-tolerant semiconductors that are non-toxic and stable without encapsulation, thus addressing two of the key challenges of lead-halide perovskites. Efforts to identify lead-free perovskite-inspired materials can be broadly classified into three strategies: 1) identification of chemically analogous materials (e.g., tin-based perovskites or bismuth-based defect-ordered perovskites); 2) identification of lead-free halides with a perovskite crystal structure (e.g., double cation perovskites and vacancy-ordered perovskites); 3) identification of materials that can mimic the defect tolerance of the lead-halide perovskites (e.g., bismuth oxyiodide or BiOI). Extensive reviews discussing the design rules, classes of materials grown, the processing strategies, and device structure have been written, and some examples are refs. [18,33,111,232–235], but a critical factor that has received less attention is the role of dimensionality in these materials. As stated in the Introduction, dimensionality encompasses the crystal and electronic structure, as well as form factor (i.e., thin films or nanocrystals). This section examines the role these parameters have on the optoelectronic properties (mobility, charge-carrier lifetime and exciton binding energy), defect tolerance, and performance of the perovskite-inspired materials in photovoltaics and light-emitting diodes. To illustrate these effects, a selection of perovskite-inspired materials is considered in order aid the discussion of the role of dimensionality. These materials are summarized in **Figure 19**. To provide context for the materials discussed, the toxicity of the constituent elements is given in **Figure 20**.

4.1. Dependence of Transport Properties on the Structural and Electronic Dimensionality

4.1.1. Role of Structural Dimensionality on Mobility

As explained in Section 3 (Equation (1)), the effective mass depends on the band curvature. This is strongly affected by the structural dimensionality, which affects the arrangement and degree of overlap of atomic orbitals, and therefore the degree of band dispersion.[232] 3D Sn- and Ge-based perovskites have demonstrated low effective masses similar to those of $MAPbI_3$, along with high electron and hole mobilities (**Table 2**). This is because these materials have disperse bands, as can be seen in **Figures 21**a,b.[239] The high dispersion in the valence band comes about from the Sn^{2+} and Ge^{2+} cations having filled valence *s* orbitals that can hybridize with the anion *p* orbitals to form a pair of bonding-antibonding states in the upper valence band. In addition, spin-orbit coupling further increases band dispersion, resulting in both a smaller band gap and lower effective masses for both electrons and holes.[106,123]

2D and quasi-2D Sn-based perovskites have been synthesized to improve the stability of the materials against moisture, similar to what has been done with LHPs (Section 3.2).[241] 2D Sn-based perovskites are achieved when a long-chain alkylammonium cation is used in the A-site, such as butylammonium (BA; $C_4H_9NH_3^+$)[241] or phenethylammonium (PEA; $C_6H_5C_2H_4NH_3^+$).[143,159] These disrupt the 3D perovskite crystal structure, resulting in layers of inorganic corner-sharing $[SnI_6]^{4-}$ octahedra alternating with layers of the alkylammonium cation. The long hydrophobic alkylammonium cation chains act as barriers against moisture ingress, protecting the inorganic layers from degradation.[143] When there is only one inorganic layer between a pair of organic layers, the perovskite is purely 2D. As with lead-based RP perovskites, the number of inorganic layers can be increased by mixing the long-chain alkylammonium cation (e.g., MA) with a small A-site cation that can fit within the perovskite lattice. Examples include $(BA)_2(MA)_{n-1}Sn_nI_{3n+1}$, in which n gives the number of inorganic layers between pairs of organic layers. That is $n = 1$ gives a 2D perovskite and $n = \infty$ a 3D perovskite; n between these extremes is a quasi-2D perovskite. The alkylammonium cations do not contribute to the energy states near the band-edges. Separating the inorganic tin-halide layers with the alkylammonium cation layers therefore disrupts the electronic connectivity of the inorganic lattice, resulting in regions in *k*-space with flat bands (Figure 21c). Computations of the band structure of quasi-2D Sn-based perovskites have therefore shown the bands to be flat between layers, but still

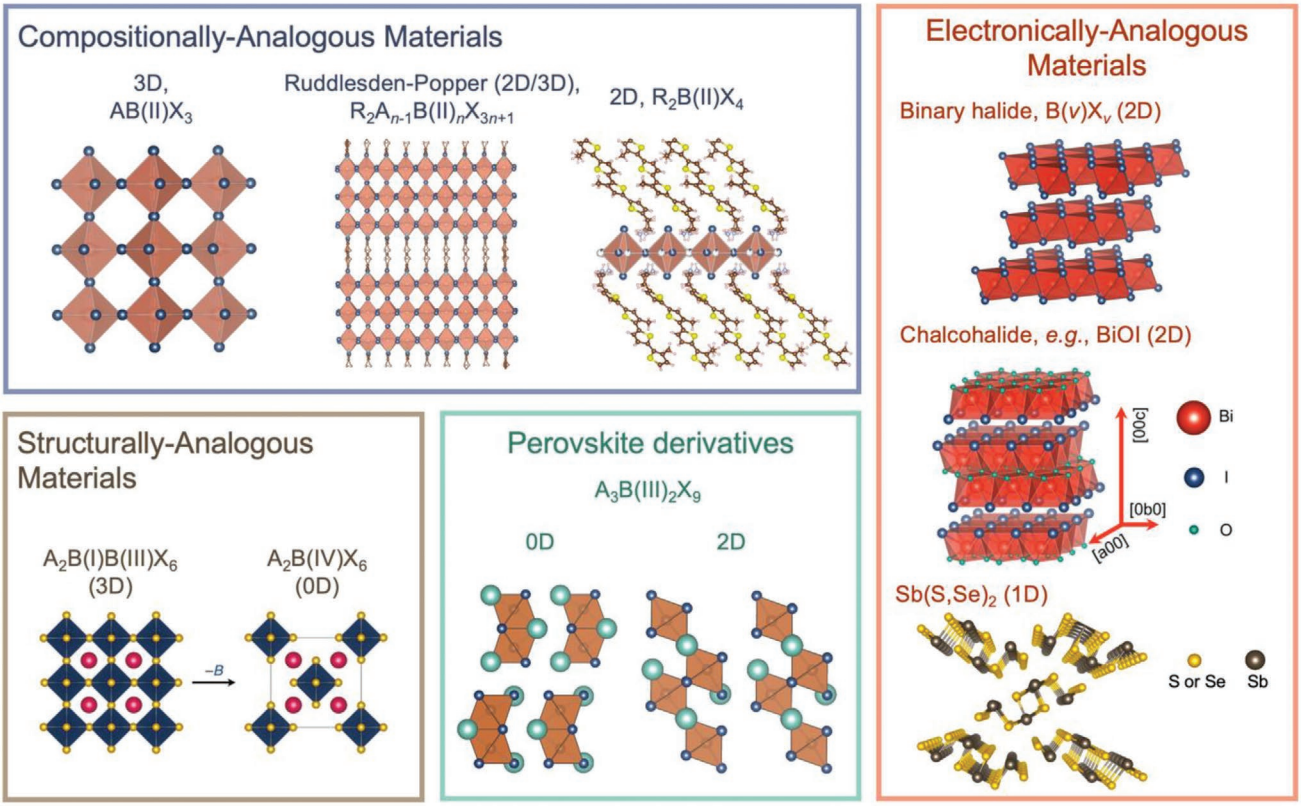

Figure 19. Overview of the classes of perovskite-inspired materials discussed in Section 4. The structural dimensionality of these materials is given. N.B., in the ABX_3 crystal structure, the A-site cation has been removed for clarity. The double and vacancy-ordered perovskite crystal structures are reproduced with permission.[236] Copyright 2019, American Chemical Society.

highly dispersive with low effective masses within inorganic layers (e.g., refer to Figure 21d for $(BA)_2(MA)_2Sn_3I_{10}$, in which $n = 3$).[241] Reducing the dimensionality of Sn-based perovskites to layered perovskites therefore results in significant anisotropy in the mobility, which necessitates careful control of the preferred orientation in order to achieve efficient charge-carrier extraction in devices with either out-of-plane (e.g., photovoltaics) or in-plane electrodes (e.g., thin film transistors). Similar

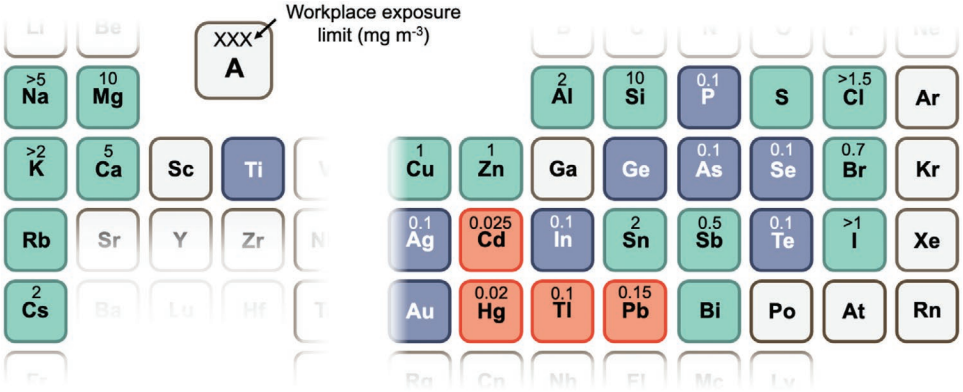

Figure 20. Toxicity of elements used in perovskite-inspired materials. The workplace exposure limits given for each element refer to the limit for an 8-h reference period for the element or compounds containing the element published by the UK Health and Safety Executive.[237,238] The workplace exposure limits for Cl and I are given for a 15-min reference period, and their values for an 8-h period are therefore estimated. Elements with workplace exposure limits of ≥0.5 mg m^{-3} are shaded green. Data is not published for all elements, in which case the potential toxicity of the element was evaluated based on the lethal dose that kills 50% of a test sample (LD_{50}) for the element, as compared to elements with ≥0.5 mg m^{-3} workplace exposure limits. The elements Cd, Hg, Tl and Pb are shaded red due to their high toxicity, low workplace exposure limits, and given the fact that the use of these elements in electronic products are controlled by safety regulations. The elements shaded blue have low workplace exposure limits (comparable to those of the toxic elements), or have low to moderate LD_{50} values associated with them. However, these data are insufficient to designate the element as toxic or non-toxic. We emphasize that the toxicity of the compound could be significantly different to that of the element.

Table 2. Properties of lead-free perovskite-inspired materials discussed in Section 4, and their performance in thin film photovoltaics.

Material	Space group	Band gap [eV]	Exciton binding energy [meV]	Effective mass[a)]/m_0	Mobility [$cm^2 V^{-1} s^{-1}$]	Highest PV PCE [%]	Ref.
			Structurally 3D materials				
$CsSnI_3$	*Pnma* (B-γ phase)	1.3	18	0.04 (m_e) 0.07 (m_h)	536 (μ_e; PC) 585 (μ_h; PC)	3.56	[100,260,397–399]
$MASnI_3$	*P4mm* (α phase)	1.3	8[a)]	0.05 (m_e) 0.08 (m_h)	2320 (μ_e; PC) 322 (μ_h; PC)	6.63	[260,265,400–403]
$FASnI_3$	*Amm*2 (α phase)	1.35–1.41	3.1	0.02 (m_e) 0.05 (m_h)	103 (μ_e; PC) 67 (μ_h; TF)	12.4[b)]	[260,265,327,402,404]
$CsGeI_3$	*R*3*m*	1.65	–	0.22 (m_e) 0.23 (m_h)	–	0.11	[405,406]
$CsSn_{0.5}Ge_{0.5}I_3$	*R*3*m*	1.50	–	–	974 (μ_e; TF) 213 (μ_h; TF)	7.11	[328]
$MAGeI_3$	*R*3*m*	2.0	–	0.27 (m_e) 0.29 (m_h)	–	0.40	[328,405,406]
$FAGeI_3$	*R*3*m*	2.3	–	0.66 (m_e) 0.76 (m_h)	–	–	[405,406]
$(FA_{0.9}EA_{0.1})_{0.98}EDA_{0.01}(Sn,Ge)I_3$	*Amm*2 (α phase)	1.42	–	–	–	13.2	[407]
$Cs_2AgBiBr_6$	$Fm\bar{3}m$	2.25 (TF) 2.0 (SC)	167[a)]	0.31 (m_e) 0.18 (m_h)	11.81 (SC) <1 (TF)	2.84	[35,368,377,408,334]
$Cs_2AgSbBr_6$	$Fm\bar{3}m$	2.18 (TF) 1.6 (SC)	124[a)]	0.26 (m_e) 0.15 (m_h)	–	–	[35,409]
			Structurally quasi-2D materials				
$(BA)_2(MA)_2Sn_3I_{10}$	*Cmca*	1.50	159[a)]	0.33 (m_e) 0.30 (m_h)	–	1.94	[324,245,410]
$(BA)_2(MA)_3Sn_4I_{10}$	*Cmca*	1.42	133[a)]	0.37 (m_e) 0.31 (m_h)	–	2.53	[324,245,410]
			Structurally 2D materials				
$(BA)_2SnI_4$	*Pbca*	1.8–2.0	286[a)]	0.33 (m_e) 0.28 (m_h)	–	–	[324,245,411]
$(PEA)_2SnI_4$	$P\bar{1}$	2.9–2.2	190	0.09 (m_e) 0.40 (m_h)	15 (TF)	–	[264,412–414]
$Cs_3Sb_2I_9$	$P\bar{3}m1$	2.05	100	0.44 (m_e) 0.60 (m_h)	6.81 (μ_h; TF)	1.49	[242,415,416]
$K_3Sb_2I_9$	$P\bar{3}m1$	2.02	120–137	3.15 (m_e) 1.83 (m_h)	–	0.07	[253]
$Rb_3Sb_2I_9$	$P2_1/n$	2.03–2.24	95–110	1.11 (m_e) 1.55 (m_h)	0.26 (TF)	1.37	[253,272,316,417]
$Cs_3Sb_2I_6Cl_3$	$P\bar{3}m1$	2.0–2.1	≈100	–	4.02–7.74 (μ_h; TF)	2.15	[259]
$Cs_3Bi_2I_6Br_3$	$P\bar{3}m1$	1.75	–	–	–	1.15	[376,258]
$Cs_3Bi_2I_6Cl_3$	$P\bar{3}m1$	2.07	70	0.39 (m_e) 0.41 (m_h)	–	–	[244,273]
$(NH_4)_3Bi_2I_9$	$P2_1/n$	2.05	–	–	213 (SC, //) 11 (SC, $\perp$)	–	[250,418]
InI	*Cmcm*	2.0	4.3	0.15 (m_e) 0.25 (m_h)	–	0.39	[15,106,419,420]
SbI_3	$R\bar{3}H$	2.1	–	2.12 (m_e) 9.57 (m_h)	–	–	[106,420,421]
BiI_3	$R\bar{3}H$	1.67 ± 0.09	160–180	1.85 (m_e) 10.39 (m_h)	600 (μ_e; SC) 20 (μ_h; SC)	1.21	[106,420,422–426]
BiOI	*P*4/*nmm*	1.93	–	0.2 (m_e) 0.2 (m_h)	14 (TF)	1.8	[300,427]

Table 2. Continued.

Material	Space group	Band gap [eV]	Exciton binding energy [meV]	Effective mass[a]/m_0	Mobility [$cm^2 V^{-1} s^{-1}$]	Highest PV PCE [%]	Ref.
			Structurally 1D materials				
Sb_2S_3	*Pnma*	1.5–2.2	≈100[b]	1.08 (m_e) ≈3 (m_h)	7.1 (TF)	7.5	[337,428–430]
Sb_2Se_3	*Pnma*	1.04–1.18	≈100[b]	0.67 (m_e) ≈3 (m_h)	≈10 (μ_e; TF)	9.2	[341,431–433]
SbSI	$Pna2_1$	1.8–2.15	–	0.21 (m_e) 0.27 (m_h)	–	3.05	[106,434–436]
BiSI	*Pnma*	1.56–1.59	–	0.30 (m_e) 0.61 (m_h)	–	1.32	[302,437]
BiSeI	*Pnma*	1.29–1.32	–	0.30 (m_e) 0.81 (m_h)	–	–	[302]
			Structurally 0D materials				
$Cs_3Sb_2I_9$	$P6_3/mmc$	2.43	170–180	1.40 (m_e) 1.55 (m_h)	3.14–4.92 (μ_h; TF)	0.84	[253,259,415,416,438]
$MA_3Sb_2I_9$	$P6_3/mmc$	2.20	54[a]	0.21 (m_e) 0.31 (m_h)	17 (SC)	2.04	[438–441]
$Cs_3Bi_2I_9$	$P6_3/mmc$	2.75–2.80	295	0.63 (m_e) 1.8 (m_h)	4.3 (μ_e; SC) 10^{-7} (TF)	3.2	[244,274,317,442]
$MA_3Bi_2I_9$	$P6_3/mmc$	2.1–2.6[c]	>300[d]	0.41 (m_e) 0.62 (m_h)	8×10^{-4} (TF) 30 (SC)	3.17	[248,271,332,441,443,444]
Cs_2SnI_6	$Fm\bar{3}m$	1.3	–	0.48 (m_e) 1.32 (m_h)	310 (μ_e; SC) 8.5 (μ_e; PC) 10.6 (μ_e; TF)	1.47	[236,278,326,445]
K_2SnI_6	$Fm\bar{3}m$	0.31[a]	8.9[a]	0.17 (m_e) 0.46 (m_h)	–	–	[261]
K_2SnI_6	$P2_1/n$	1.16[a]	15.3[a]	0.58 (m_e) 0.78 (m_h)	–	–	[261]
K_2SnBr_6	$Fm\bar{3}m$	1.65[a]	59[a]	0.33 (m_e) 0.83 (m_h)	–	–	[261]
K_2SnCl_6	$Fm\bar{3}m$	3.36[a]	110[a]	0.47 (m_e) 0.99 (m_h)	–	–	[261]
Cs_2TeI_6	$Fm\bar{3}m$	1.59	–	0.22 (m_e) 1.40 (m_h)	–	–	[236][278]
Cs_2TiI_6	$Fm\bar{3}m$	1.02	–	1.58 (m_e) 0.79 (m_h)	–	–	[446]
Cs_2TiBr_6	$Fm\bar{3}m$	1.8–1.9	–	1.79 (m_e) 0.9 (m_h)	–	3.3	[312,447]

The values tabulated were determined through measurements unless otherwise indicated. Note that effective masses change with k vector in anisotropic materials, and the values tabulated are the lowest values. SC, single crystal; PC, polycrystalline sample; TF, a thin film sample; //, in-plane; ⊥, out-of-plane. [a]Parameter determined through computations; [b]12.4%-efficient devices achieved using $PEA_{0.15}FA_{0.85}SnI_3$ perovskites[327]; [c]There is significant variability in the band gaps reported in the literature. $(MA)_3Bi_2I_9$ exhibits a strong excitonic peak at room temperature. Typically, the low energy edge of this is fitted in a Tauc plot, giving a band gap of ≈2.1 eV. This may be valid if the low-energy tail is due to the indirect transition. Otherwise, if the start of the continuum is taken to be the band gap, then this would be ≈2.6 eV. More detailed analysis of the band gap of $A_3B_2X_9$ materials (as has been done with $Cs_3Bi_2I_9$)[274] is needed; [d]While many groups have reported the exciton binding energy of $(MA)_3Bi_2I_9$ to be >300 meV,[271,332,443] other groups have reported values of 70 meV[448] and 210 meV.[444]

results are also predicted for 2D and quasi-2D Ge-based perovskites.[243]

Beyond Sn- and Ge-based perovskites, Bi- and Sb-based materials have also been extensively investigated owing to their lower toxicity than Pb (Figure 20), many of their compounds being phase-stable in air, and their stable valence s^2 electrons which can hybridize with halide anion orbitals to form a similar electronic structure as $MAPbI_3$ (refer to Figure 7a in Section 3).[15,33] However, these materials form a stable 3+ oxidation state and cannot directly substitute for Pb^{2+} in ABX_3. Instead, a defect-ordered perovskite ($A_3B_2X_9$) forms. This can be thought of as $A_3B_2\square X_9$, in which every third metal cation in ABX_3 is substituted for a vacancy (□). As a result, many $A_3B_2X_9$ compounds have 0D structural dimensionality comprising isolated bioctahedral $[B_2X_9]^{3-}$ groups that alternate with the A-site cations.[232,244,245] This leads to flat bands, and high effective masses occur in many compounds (Table 2). For example, Hall-effect measurements showed the hole mobility

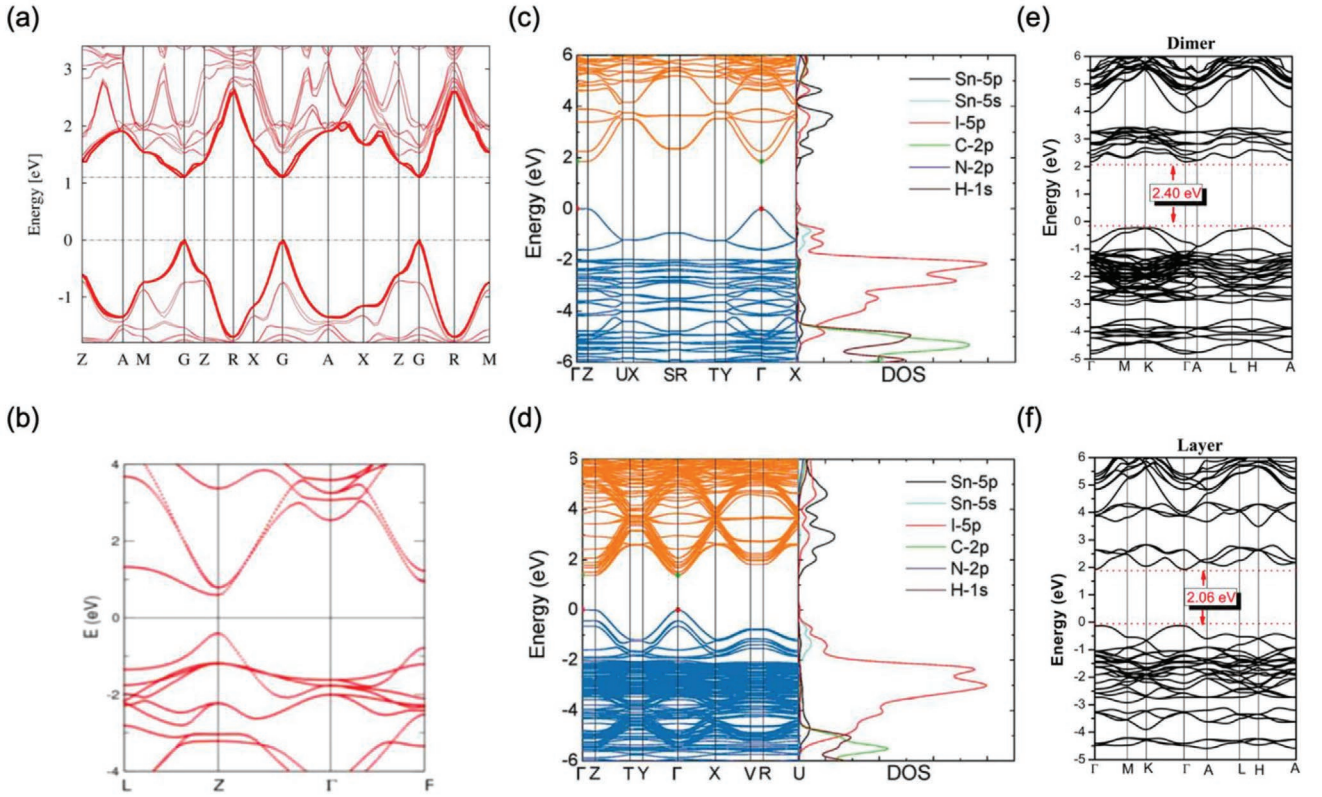

Figure 21. Calculated band structure of a) $MASnI_3$, b) $CsGeI_3$, c) 2D $(BA)_2SnI_4$, d) quasi-2D ($n = 3$) $(BA)_2(MA)_2Sn_3I_{10}$, e) 0D $Cs_3Sb_2I_9$, and f) 2D Cs_3SbI_9. a) Reproduced under the terms of the CC-BY license.[123] Copyright 2015, Springer Nature. b) Reproduced with permission.[240] Copyright 2015, American Chemical Society. c,d) Reproduced with permission.[241] Copyright 2018, Published by the Royal Society of Chemistry. e,f) Reproduced under the terms of the CC-BY license.[242] Copyright 2015, American Chemical Society.

of $MA_3Bi_2I_9$ single crystals to be 70 $cm^2\ V^{-1}\ s^{-1}$ at room temperature,[246] which is at least an order of magnitude lower than the mobility of Pb- and Sn-based perovskites.[100] Furthermore, the same group showed that the mobilities of $MA_3Bi_2I_9$ crystals from time-of-flight measurements were lower, in the range of 1–8 $cm^2\ V^{-1}\ s^{-1}$.[246] Mobility measurements of $Cs_3Bi_2I_9$ single crystals have reached 4.3 $cm^2\ V^{-1}\ s^{-1}$ at room temperature,[244] whereas $Cs_3Bi_2I_9$ polycrystalline thin films have room temperature mobilities down to 10^{-7} $cm^2\ V^{-1}\ s^{-1}$.[247] $A_3Sb_2X_9$ compounds that also have 0D structural dimensionality have similar effective masses and low mobilities (Table 2).

The effective masses of $A_3B_2X_9$ compounds can be reduced along certain crystallographic orientations by tuning the A-site or X-site ions to stabilize a 2D structure. In particular, it has been found for Sb- and Bi-based defect-ordered perovskites that using A-site cations with smaller radii favor the formation of the 2D phase over the layered phase.[232] Thus, $MA_3Bi_2I_9$ and $MA_3Sb_2I_9$ favor the 0D phase,[245,248,249] whereas $(NH_4)_3Bi_2I_9$, $Rb_3Bi_2I_9$, $(NH_4)_3Sb_2I_9$, $Rb_3Sb_2I_9$, and $K_3Sb_2I_9$ favor the 2D phase.[250–253] MA^+ has an ionic radius of 180 pm,[254] whereas NH_4^+, Rb^+, and K^+ have ionic radii of approximately 150 pm or smaller.[232,255] Cs^+ has an ionic radius of in between these two groups of 167 pm.[232] While $Cs_3Bi_2I_9$ tends to form the 0D phase, the 0D and 2D phases of $Cs_3Sb_2I_9$ have comparable formation energies and the polymorph formed is dependent on the synthesis conditions.[232,242,253] For example, in Figures 21e,f, it is shown that the 2D polymorph of $Cs_3Sb_2I_9$ has improved band dispersion over the 0D polymorph.[242] It has also been shown that the 2D phase for $MA_3Sb_2I_9$ can be stabilized by replacing the SbI_3 precursor with Sb-acetate, which may sterically allow larger A-site cations to be incorporated in the layered phase.[249] The layered phases of $A_3B_2I_9$ compounds have demonstrated lower effective masses and higher mobilities along the covalently bonded directions. For example, space-charge limited current density (SCLC) measurements of layered $(NH_4)_3Bi_2I_9$ single crystals demonstrated a mobility of 213 $cm^2\ V^{-1}\ s^{-1}$ along the covalently bonded direction and 11 $cm^2\ V^{-1}\ s^{-1}$ between layers.[250] In many cases, smaller and more direct band gaps have been reported in the 2D polymorph compared to the 0D phase.[242,249,250,253] All of these factors have contributed to the 2D polymorphs demonstrating improved performance in photovoltaics (Table 2).[242,253]

Beyond tuning the A-site cation, it has also been shown that the 2D polymorph of $A_3B_2X_9$ materials can be stabilized by alloying I with Br or Cl, resulting in each $[BX_6]^{3-}$ octahedron changing from being face-sharing (0D phase) to corner sharing (2D phase).[244,256,257] For example, a computational investigation into $Cs_3Bi_2(I,Br)_9$ compounds found that Br tends to bridge neighboring octahedra to favor the formation of the layered phase in order to minimize strain in the system.[256] However, the orbitals from Br and Cl do not contribute to the density of states at the band-edges, and is dominated by the hybridization

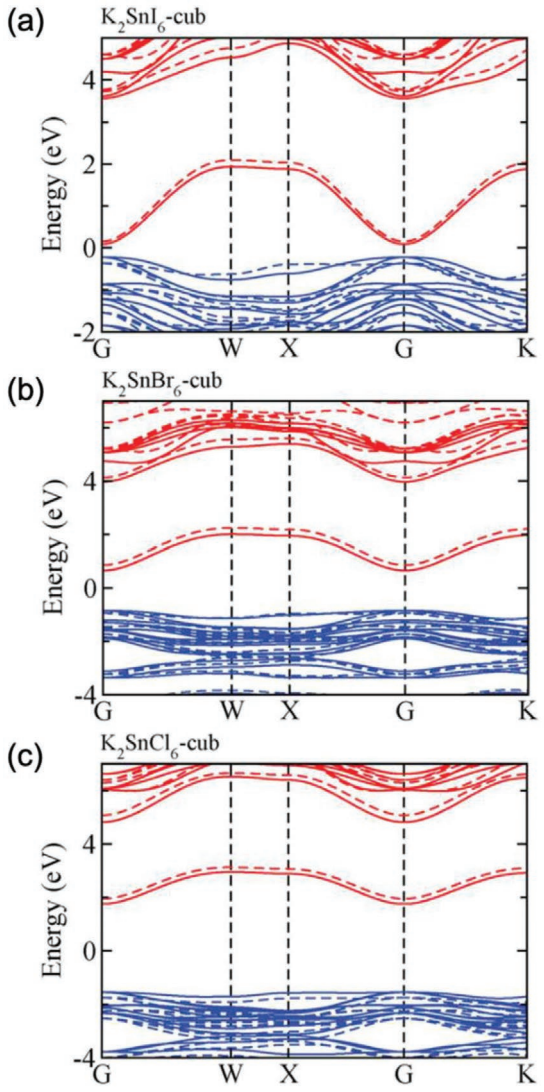

Figure 22. Computed electronic structure of a) K_2SnI_6, b) K_2SnBr_6, and c) K_2SnCl_6 with a cubic crystal structure using the HSE06 hybrid functional. Reproduced with permission.[261] Copyright 2019, Royal Society of Chemistry.

of the I and Bi/Sb orbitals.[244,256] Halide alloying to stabilize the 2D phase has thus been shown to be effective in lowering the effective masses of carriers in along the interconnected octahedra, as well as resulting in a smaller and more direct band gap, which leads to improved photovoltaic device performance compared to the 0D polymorphs (Table 2).[232,244,256,258,259]

Another class of perovskite-inspired materials gaining increasing attention are vacancy-ordered double perovskites, which have the general formula A_2BX_6. These can be thought of as double perovskites, but instead of alternating B(I)X_6 and B(III)X_6 octahedra, there are B(IV)X_6 octahedra alternating with vacancies (see Figure 19). This system is particularly advantageous for Sn-based perovskites, which are more stable in the 4+ oxidation state. However, the vacancy-ordered double perovskite system also has a 0D structural dimensionality.[236] In spite of this, Cs_2SnI_6 single crystals have demonstrated an electron mobility of 310 $cm^2\ V^{-1}\ s^{-1}$,[236] which is comparable to the electron mobility of $CsSnI_3$ polycrystals of 536 $cm^2\ V^{-1}\ s^{-1}$ at room temperature.[260] This high mobility is due to the close-packed halide framework, which leads to larger orbital overlap and higher band dispersion.[236] Band dispersion is also influenced by the A- and X-site ions. Changing the halide from I to Br or Cl results in reduced band dispersion because the smaller ionic radii of the Br^- and Cl^- anions leads to reduced orbital overlap and higher effective masses (**Figure 22**).[236,261] Reducing the size of the A-site cation has also been found through computational investigations to reduce the effective masses of electrons and holes in A_2BI_6 compounds,[262] which may in part be due to an increase in orbital hybridization as the lattice parameters decrease.

4.1.2. Role of Structural Dimensionality on Exciton Binding Energy

Ruddlesden–Popper tin-based perovskites have been investigated since the 1990s,[173] and, inspired by the results with lead-based perovskites (refer to Section 3.2), have more recently gained a resurgence in interest.[233] Groups have shown that mixing 3D $FASnI_3$ with 2D phenethylammonium tin iodide (PEA_2SnI_4), or by using a π-conjugated oligothiophene ligand in the A-site (i.e., $(4Tm)_2SnI_4$) has led to improved performance in photovoltaic and thin film transistor devices, respectively,[263,264] but in addition to affecting the mobility (as discussed in the previous section),[100,264,265] reducing the structural dimensionality also leads to the exciton binding energy increasing through a combination of quantum confinement and dielectric screening (refer to Section 3.3.2).[148,266] Furthermore, as the exciton binding energy increases, the fraction of carriers existing as excitons increases, and these can influence carrier transport by coupling with phonons in the lattice, as discussed in Section 5.

Increases in the exciton binding energy can also occur in structurally 3D tin perovskites through quantum and dielectric confinement when grown as low-dimensional nanostructures, such as quantum dots (0D), nanowires (1D), or nanoplatelets (2D).[191,267–269] For example, it has been shown through both computations and experiment that, as with lead-based perovskites (Section 3.4), reducing the number of monolayers in $CsSnI_3$ nanoplatelets results in a blue-shift in the band gap.[268,270] In colloidal $CsSnI_3$ nanoplatelets synthesized by Wong et al., a photoluminescence peak centered at 1.59 eV was achieved, whereas in bulk $CsSnI_3$, the photoluminescence peak was centered at 1.3 eV. These nanoplatelets have a thickness of 3.8 nm, which is associated with four or fivge monolayers, and are complexed with long and short-chain organic ligands. The blue-shift in band gap was therefore associated with quantum confinement effects (by reducing the thickness of $CsSnI_3$ nanoplatelets below the Bohr radius) as well as dielectric confinement effects.[268]

Bulk thin films of PIMs with 0D structural dimensionality also exhibit strong confinement of electrons and holes, resulting in high exciton binding energies. This has especially been well evidenced in $A_3B_2I_9$ compounds, in which the exciton binding energies of the 0D materials have been reported to range from 54 meV (for $MA_3Sb_2I_9$) to >300 meV (for $MA_3Bi_2I_9$), owing to the localization of carriers within the isolated bioctahedral $[B_2X_9]^{3-}$ groups (Table 2).[244,249,253,257,271] When electrons and holes are confined more strongly in a smaller region, the

exciton oscillator strength becomes larger, leading to the excitonic peak adopting a higher absorption coefficient as well as a larger separation from the absorption continuum.[148] As detailed in Section 5, these excitons can couple to phonons to form self-trapped excitons that limit mobilities and act as loss channels for carriers.[272]

Lower exciton binding energies are achieved for $A_3B_2X_9$ compounds with a 2D structural dimensionality. For example, while 0D $Cs_3Sb_2I_9$ has an E_b of 170–180 meV,[253] 2D $Cs_3Sb_2I_9$ has an E_b of approximately 100 meV.[3] Similar reductions in exciton binding energies could be achieved by halide-alloying 0D $A_3B_2X_9$ materials to stabilize the 2D polymorph. For example, McCall et al. showed from optical absorbance measurements that the exciton binding energy of the 2D polymorph of $Cs_3Bi_2I_9$ (E_b = 70 meV;[273] achieved by alloying with Cl, as detailed in Section 4.1.1) is substantially lower than that of the 0D polymorph (E_b = 295 meV).[274] The 0D polymorph exhibited a distinct excitonic peak, whereas the 2D polymorph did not have an excitonic peak that could be observed above the absorption edge due to the electronic band gap (**Figure 23**a).[244]

Vacancy-ordered double perovskites (i.e., A_2BX_6 compounds) are also structurally zero-dimensional, but as discussed in Section 4.1.1., the closely packed framework of halide anions results in stronger orbital overlap and improved band dispersion.[236,261] Not only does this result in reduced effective masses, but also reduced exciton binding energies. For example, calculations predict that the Wannier–Mott exciton binding energies of K_2SnI_6 are approximately 100 meV or lower (depending on whether the static or ionic dielectric constant is used; refer to Table 2).[261] These calculations further show that the exciton binding energy increases as the halide is changed from I to Br to Cl, which correlates with the trend in effective masses. This is due to the halide anion ionic radius reducing, which leads to reduced orbital overlap and band dispersion.[236]

The size of the exciton binding energy can influence the optical properties of materials. In materials with high E_b, there is a large separation of the excitonic peak from the electronic band gap, and the difference in energy between the exciton peak to the band gap is often considered to give the E_b.[149] In such cases, fitting the absorption onset in a Tauc plot is no longer a valid method to determine the band gap, since this would only give the lower energy edge of the excitonic peak and underestimate the electronic band gap.[275] For example, 0D $Cs_3Bi_2I_9$ and 2D $Cs_3Bi_2I_6Cl_3$ have very similar absorption onsets, (Figure 23a)[244] but from calculations, the 0D compound has a wider band gap than the 2D compound. The larger E_b of the 0D compound results in a more pronounced excitonic peak that is more red-shifted to the continuum. As a result, the absorption onset of the excitonic peak of the 0D compound is similar to the optical band gap of the 2D compound.[244] Approaches to determine the E_b and band gap of materials with the excitonic peak overlapping with the continuum absorption edge include fitting an Elliot model to the optical data.[274] However, for some materials, a peak in the absorption edge is not necessarily solely due to excitons in the system. For example, a sharp absorption onset has been found in $Cs_2Ag(Sb_xBi_{1-x})Br_6$ double perovskite thin films (Figure 23b). Li et al. recently showed that this is not necessarily due to excitons but could be accounted for by the electronic structure of the material itself (Figure 23c).[35]

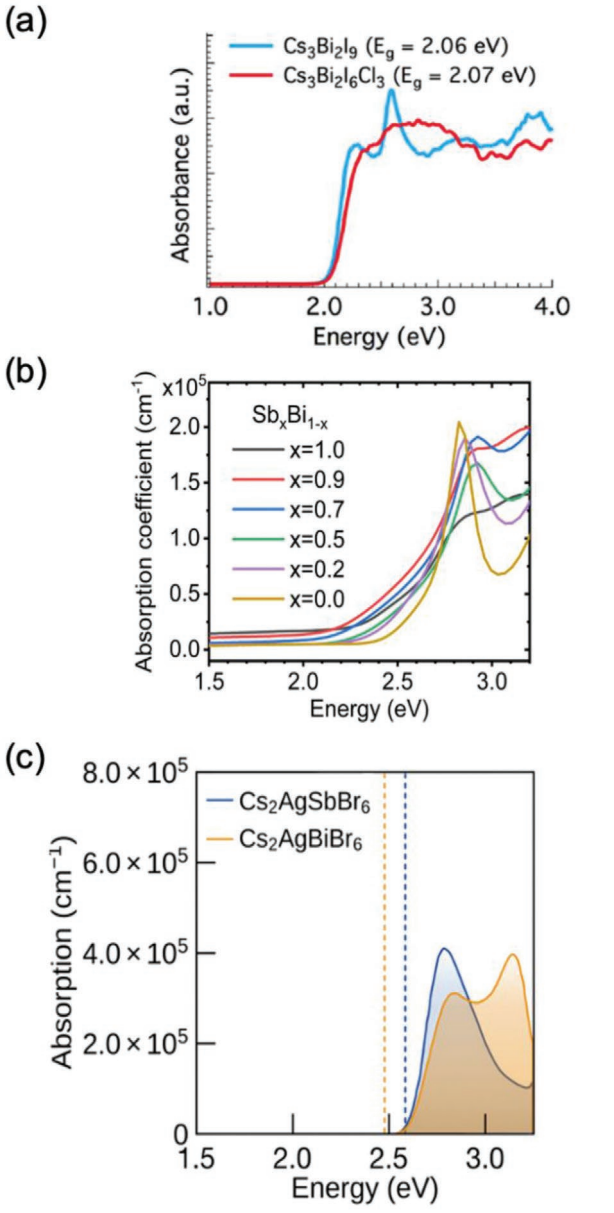

Figure 23. a) Absorption spectra of 0D $Cs_3Bi_2I_9$ and 2D $Cs_3Bi_2I_6Cl_3$. Reproduced with permission.[244] Copyright 2019, American Chemical Society. b) Measured absorption coefficients of $Cs_2Ag(Sb_xBi_{1-x})Br_6$ thin films and c) computed absorption spectra of $Cs_2AgSbBr_6$ and $Cs_2AgBiBr_6$. Reproduced under the terms of the CC-BY license.[35] Copyright 2020, Royal Society of Chemistry.

4.1.3. Role of Structural Dimensionality on Non-Radiative Recombination

Reducing the structural dimensionality generally results in lower orbital overlap, and wider band gaps tend to occur.[111,241,242,244] A consequence of wider band gaps is that deep traps levels may be more likely to form,[111,275] which give rise to increased non-radiative recombination.[15,106] For example, defect calculations of $Cs_3Sb_2I_9$,[242] BiI_3,[276] Cs_2SrPbI_6,[111] $Cs_2AgBiBr_6$,[277] and Cs_2TeI_6[278] all suggest that deep transition levels form. Consistent with high non-radiative recombination rates,

low PL intensities and short lifetimes have been found in these materials.[253,279,280] However, we emphasize that a wide range of other factors also play a role on whether deep or shallow traps form beyond simply the size of the band gap. These factors include both intrinsic factors (discussed in Section 4.2) and extrinsic factors, such as whether structural defects are present (which depends on the melting point of the material, as discussed in Section 2).[87]

Nevertheless, the increase in exciton binding energy that occurs in materials with reduced dimensionality also influences the recombination kinetics. As E_b increases, a larger fraction of carriers occur as excitons (as opposed to being free electrons and holes). This can be seen from the Saha equation (Equation (4)), which describes the equilibrium between unbound carriers (density of n_e and n_h) and excitons (density of n_X).[148,281]

$$n_e\, n_h = n_{eq}\, n_X \tag{4}$$

n_{eq} is the equilibrium constant between the unbound electrons and holes with the excitons, and can be determined for 3D semiconductors with Equation (5).[148]

$$2\, n_{eq} = 2\left(\frac{\mu_{ex} k_B T}{2\pi\hbar^2}\right)^{\frac{3}{2}} e^{-E_b/k_B T} \tag{5}$$

In Equation (5), μ_{ex} is the exciton reduced mass, as described for Equation (2) in Section 3.2.3. The Saha equation for 2D materials has a similar form, but has an exponent of 1 instead of 1.5 for the $\left(\frac{\mu_{ex} k_B T}{2\pi\hbar^2}\right)$ term.[148] Whether unbound carriers or excitons dominate also depends on the carrier density, in which high injection favors the formation excitons from the electron-hole pairs. The threshold electron-hole density above which excitons dominate can be calculated from Equation (6).[148]

$$n_{e(h)} + n_X = 2n_{eq} \tag{6}$$

For context, analysis by Marongiu et al. showed that lead-halide perovskites would have an electron–hole carrier density of 10^{13}–10^{14} cm^{-3} under 1 sun illumination, as calculated from their open-circuit voltage in photovoltaic devices. 3D perovskites with low effective masses and exciton binding energies would predominantly have free carriers. By contrast, 2D/quasi-2D perovskites with higher effective masses (μ_{ex} = 0.22) and exciton binding energy of greater than 250 meV would predominantly have excitons.[148] Similar effects would occur in lead-free alternatives, in which quasi-2D tin-based perovskites as well as low-dimensional perovskite-inspired materials with high exciton binding energy would predominantly have excitons under 1 sun illumination, and the kinetics of the excitons would dominate the recombination processes in the materials. In many low-dimensional perovskite-inspired materials (e.g., PEA_2SnI_4, $Rb_3Bi_2I_9$, $MA_3Bi_2I_9$, $Cs_3Bi_2I_9$, $Rb_3Sb_2I_9$, $K_3Sb_2I_9$, $MA_3Sb_2I_9$, $Cs_3Sb_2I_9$), the PL peak is Stokes-shifted to the electronic band gap due to exciton recombination or emission from self-trapped excitons (refer to Section 5).[152,242,244,253,272,274,282] However, Marongiu et al. pointed out that materials with low exciton binding energy would also form excitons from the free carriers before recombining radiatively. The PL would then have a quadratic dependence on the excess carrier density, not because of radiative recombination of free carriers, but because two free carriers form an exciton before the exciton recombines to give luminescence.[148]

Another important factor in non-radiative recombination is surface recombination at free surfaces, interfaces, and grain boundaries. Recently, it has been suggested that low-dimensional semiconductors with van der Waals interactions between layers may exhibit lower non-radiative recombination when surfaces terminate only with broken van der Waals interactions rather than broken bonds. This concept has particularly gained popularity with Sb_2Se_3, which is a 1D compound comprised of ribbons of $(Sb_4Se_6)_n$ arranged parallel to each other.[283] Note that Sb_2Se_3 is considered a PIM developed based on electronic analogy to LHPs, particularly owing to the presence of valence s^2 electrons from Sb^{3+} (see the introduction paragraph for Section 4). Although Sb and Se are covalently bonded along the [001] direction, weak van der Waals interactions occur in the [100] and [010] directions. Density functional theory calculations have shown that although (001) surfaces lead to deep traps,[284] no mid-gap states occur when Sb_2Se_3 is terminated along the (100) and (010) surfaces or surfaces parallel to the [001] direction.[283] The latter observation is supported by Kelvin probe force microscopy, which showed the surface potentials of Sb_2Se_3 to change by only 9.1 mV at grain boundaries, suggesting there to be no significant surface band bending or significant surface defects. Similarly, electron beam induced current measurements showed carrier collection to be uniform between grains, suggesting there to be no significant non-radiative recombination at grain boundaries.[283] A recent computational work also suggested that self-healing could occur in Sb_2Se_3, in which structural relaxations at the (001) surfaces result in the deep traps disappearing (**Figure 24**), thus enabling benign grain boundaries and surfaces.[284] However, another recent computational work suggests that deep anti-site defects may act as prevalent recombination centers within the bulk of this system that lead to a large V_{OC} deficit. The stability of these anti-site defects was attributed to the amphoteric, soft chemical behavior of both antimony and selenium.[285]

4.1.4. Electronic Dimensionality and the Effect on Charge-Carrier Transport and Lifetime

From Sections 4.1.1–4.1.2, it could be noted that structural dimensionality does not consistently account for the differences in effective mass, band gap, and exciton binding energy across all materials. This is because these parameters depend on the degree of orbital overlap and how uniform this is spatially. In other words, the electronic dimensionality could be a more direct descriptor of the electronic and optical properties of materials. In most cases, the structural and electronic dimensionality are the same, hence the optoelectronic properties vary as expected with structural dimensionality in most cases. However, structural and electronic dimensionality can deviate substantially due to structural or chemical causes.[111] Three prominent examples among PIMs are Ge-based perovskites, double perovskites and vacancy-ordered double perovskites,

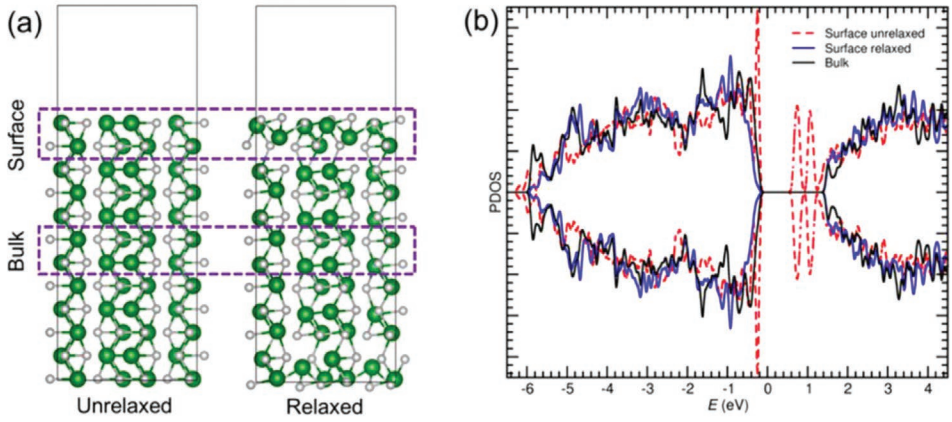

Figure 24. a) Structure of the (001) surface of Sb_2Se_3 (before and after structural relaxation in DFT), shown along the [100] projection. b) Partial density of states of Sb_2Se_3 in the bulk and surface, before and after structural relaxation. Reproduced with permission.[284] Copyright 2020, American Chemical Society.

where the structural dimensionality is no longer adequate as a descriptor for their optoelectronic properties.[111,236,286]

Reductions in electronic dimensionality due to chemical effects are especially well seen in double cation perovskites, with the general formula $A_2B(I)B(III)X_6$, where A and B(I) are monovalent cations, B(III) a trivalent cation and X an anion. When both the B(I) and B(III) cations have filled valence *s* orbitals (e.g., $Cs_2TlBiBr_6$),[287] it is possible for high electronic dimensionality to occur, with wide band widths, high band dispersion, and small band gaps that are direct,[286] but in many cases, the B(I) cation comprises Na^+, K^+, or Rb^+, which does not contribute energy states to the band-edges. The energy states from the octahedra based on B(III) (e.g., Bi^{3+} or Sb^{3+}) are therefore isolated, giving a 0D electronic dimensionality, despite the 3D structural dimensionality.[286] This was illustrated by Xiao et al., who compared the electronic structure of Cs_2PbPbI_6 with Cs_2SrPbI_6 (**Figure 25**). Substituting Pb^{2+} with Sr^{2+} resulted in the band gap becoming indirect and increasing from 1.48 to 3.05 eV. The defect levels also became deeper. These effects were because the band-edge density of states comprised hybridized orbitals from Pb and I, and the Sr did not contribute to these states. Cs_2SrPbI_6 therefore comprised isolated $[PbI_6]^{4-}$ octahedra at the band-edges, thus giving rise to a 0D electronic structure.[111] Using transition metal cations (e.g., Ag^+ or Cu^+) for the B(I) cation can result in higher dimensionality due to the outer d and s orbitals contributing to the density of states at the band edges.[288,289] However, the electronic dimensionality does not reach 3D owing to the directionality of the *d* orbitals, which leads to flatter bands than electronically 3D materials, as well as indirect band gaps that lead to lower absorption coefficients and limit the maximum efficiencies achievable.[286,287] For example, in $Cs_2AgBiBr_6$, the valence band maximum has Ag d, Bi s, and Br p character at the X point, whereas the conduction band minimum has Ag s, Bi p, and Br p character at the L point, leading to an indirect band gap.[287] Interestingly, Connor et al. found that the indirect band gap of $Cs_2AgBiBr_6$ can be made direct by reducing the structural dimensionality to a layered double perovskite with only one inorganic layer between layers of long-chain butylammonium (BA) ligands. In $(BA)_4AgBiBr_6$, the Ag s orbitals were shifted closer to vacuum level, and the Bi s orbitals shifted to deeper levels, such that the valence band edge had mostly Ag d – Br p character, whereas the conduction band edge was mostly Bi p – Br p character, with both extrema occurring at the Γ point.[289]

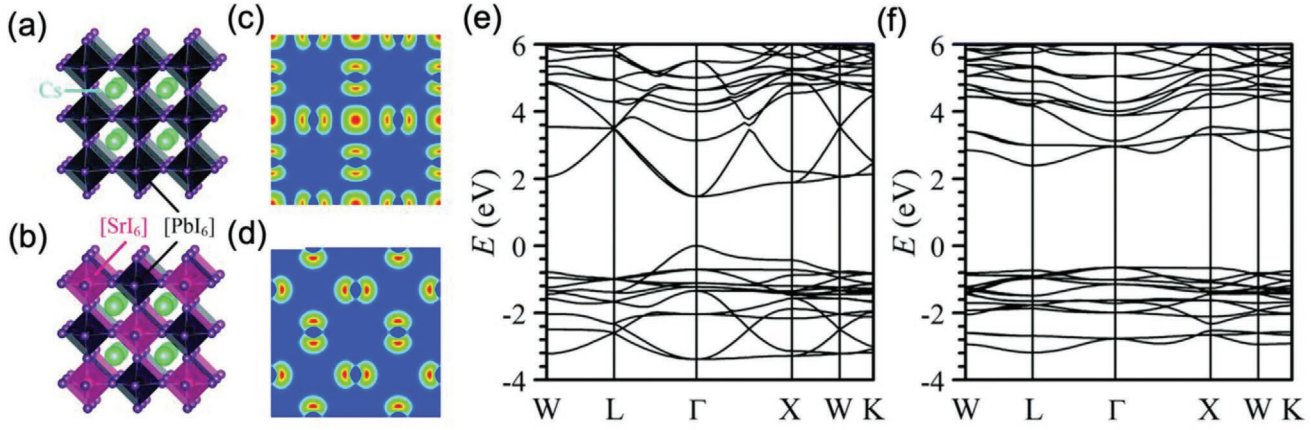

Figure 25. Illustrating the difference between structural and electronic dimensionality. Crystal structure of a) Cs_2PbPbI_6 and b) Cs_2SrPbI_6. Charge density maps of the valence band maximum of (c) Cs_2PbPbI_6 and (d) Cs_2SrPbI_6. Band structure of (e) Cs_2PbPbI_6 and (f) Cs_2SrPbI_6. Reproduced with permission.[111] Copyright 2017, Published by the Royal Society of Chemistry.

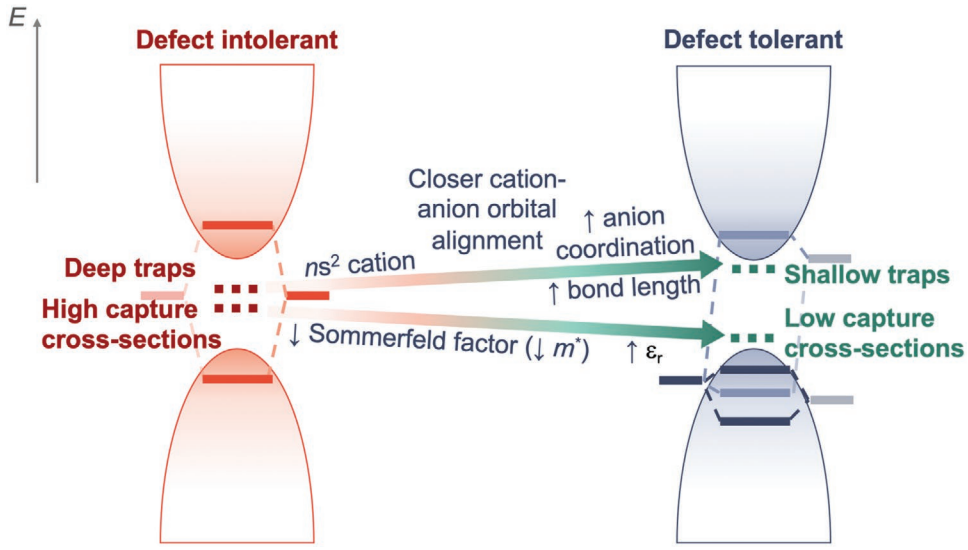

Figure 26. Illustration summarizing the discussion in Section 4.2 of the factors which contribute to a material forming shallow traps with low capture cross-sections that would give rise to defect tolerance. These factors include chemical effects (presence of ns^2 cations, dielectric constant and closer cation-anion orbital alignment) as well as effects influenced by structural and/or electronic dimensionality (anion coordination, bond length and effective mass).

Another example of electronic dimensionality deviating from structural dimensionality can be seen in $MAGeI_3$. In going from $MAPbI_3$ to $MASnI_3$ to $MAGeI_3$, one would expect the band gap to decrease due to the increase in orbital energy (i.e., closer to vacuum level) in going from Pb 6*s* to Sn 5*s* to Ge 4*s*.[111] Although $MASnI_3$ (1.2–1.3 eV) does indeed have a smaller band gap than $MAPbI_3$ (1.55 eV),[12,260] $MAGeI_3$ has a band gap of 1.94 eV.[290] Furthermore, the effective mass of $MAGeI_3$ was calculated to be $0.37m_0$,[290] which is higher than the effective masses of both $MASnI_3$ ($0.1–0.28m_0$)[123,290] and $MAPbI_3$ ($0.19–0.25m_0$).[123] These observations are due to structural distortions in the $[GeI_6]^{4-}$ octahedra due to the small ionic radius of Ge^{2+} (0.73 Å) compared to the halide anions,[291] which leads to the Ge^{2+} being off-center.[111,240,292] This affects the cation-anion orbital overlap, resulting in wider band gaps and reduced band dispersion, giving rise to the larger effective masses.[111]

Based on the discussion above, high electronic dimensionality is therefore important for achieving optoelectronic properties that are more favorable for efficient device performance. A view that was held was that high electronic dimensionality required high structural dimensionality as a pre-requisite.[286] However, recent analyses on vacancy-ordered double perovskites, particularly Cs_2SnI_6, have shown this to not necessarily be the case.[236] Early work described vacancy-ordered double perovskites to be electronically 0D as well as structurally 0D owing to the disconnected $[BX_6]^{2-}$ octahedra.[111] However, more recent first-principles analyses have shown the electronic dimensionality of Cs_2SnI_6 to be higher than 0D owing to the close-packed halide framework, which gives rise to strong overlap between the I 5*p* orbitals, as well as the Sn and I states between neighboring octahedra. This results in high dispersion in the conduction band minimum, leading to low electron effective masses of $0.48m_0$ for electrons.[236,278] Indeed, the reported electron mobility of Cs_2SnI_6 is 310 $cm^2\ V^{-1}\ s^{-1}$,[293] which is on a similar order of magnitude as 3D $CsSnI_3$.[100,236] The hole effective mass of Cs_2SnI_6 is higher at $1.32m_0$,[236] and indeed the hole mobility was found to be lower at 42 $cm^2\ V^{-1}\ s^{-1}$.[293] At the same time, the effective masses are lower than in some other low-dimensional semiconductors (e.g., BiI_3),[106] and this is due to the strong overlap in halogen *p* states, which contribute significantly to the valence band density of states.[236] Indeed, replacing the larger iodide anions with the smaller bromide anions would result in an increase in the hole effective mass. This can be seen in the comparison between Cs_2TiI_6 and Cs_2TiBr_6, in which the hole effective mass increases from $0.79–1.58m_0$ (Cs_2TiI_6) to $0.9–1.79m_0$ (Cs_2TiBr_6).[236] The interaction between the B-site cation and anion also plays a significant role on the electronic structure. For example, substituting Sn^{4+} with Te^{4+} in Cs_2BI_6 results in the band gap increasing from ≈1.3 eV (Cs_2SnI_6) to 1.6 eV (Cs_2TeI_6).[278] This is due to the hybridization of Te 5*p* states with I 5*p* states pushing up the conduction band minimum to higher energies, and which also results in the +1/0 transition level of iodine vacancies changing from shallow (0.07 eV from the conduction band minimum in Cs_2SnI_6) to deep (0.52 eV from the conduction band minimum in Cs_2TeI_6).[236,278]

4.2. Defect Tolerance and the Role of Dimensionality

According to Shockley–Read–Hall statistics, low non-radiative recombination rates can be achieved despite high densities of defects if 1) the traps are shallow (i.e., only a few kT from one of the band-edges), and/or 2) if the capture cross-sections are low (**Figure 26**).[15,33,106,276,294] Both properties have been found in LHPs, in which the most common point defects were found to be shallow[105] and the capture cross-sections small (with values of 10^{-14} cm^2 measured by deep-level transient spectroscopy).[295] This tolerance to intrinsic point defects in LHPs has also been found to extend to extrinsic defects (e.g., Fe-based

impurities, which may be introduced from the feedstock or the processing equipment).[296] These are critical for enabling LHP thin films processed outside a cleanroom, using simple equipment at low-temperature to achieve power conversion efficiencies comparable to industry-standard crystalline silicon solar cells.[9,10] Identifying the underlying causes for defect tolerance is therefore important to guide the search for promising lead-free PIMs.

An early proposition was that the formation of shallow traps with small capture cross-sections could be achieved in lead-free materials with partially-oxidized heavy *p*-block cations that have a stable valence pair of s electrons (similar to Pb^{2+}). These "ns^2 compounds" include materials based on Bi^{3+}, Sb^{3+}, Sn^{2+}, and In^{+}, and therefore encompass most of the PIMs discussed in this Section (refer to Figure 19 for an overview of the materials discussed here).[15,32,33,106] Whereas traditional semiconductors form a pair bonding–antibonding states across the band gap, in LHPs, the valence s^2 electrons in Pb^{2+} hybridize with the anion p orbitals to form a pair of bonding and antibonding states within the upper valence band (Figures 7a or 26). The empty valence Pb p orbitals also hybridize with the anion p orbitals to form a bonding state within the valence band and an antibonding state at the conduction band minimum. In addition, the high degree of spin orbit coupling results in a further decrease in band gap. The combination of these effects was proposed to favor trap formation either shallow within the band gap or resonant within the bands.[15,106] This is because these effects result in the original atomic orbitals forming close to the band-edges rather than in the middle of the band gap, and, to a first approximation, trap levels form close to the original atomic orbitals.[276] In addition, the highly polarizable Pb^{2+} cation leads to high Born effective charges and high dielectric constants,[106,297] which contribute to a reduced capture cross-section.[298,299] Some of the lead-free ns^2 compounds (e.g., InI, BiI_3, BiSI, BiOI, SbSI) have been found to also have an anti-bonding to anti-bonding state transition across the band gap, as well as high dielectric constants.[106,279,300] Recent computations and experimental work on BiOI have shown the material to be tolerant to vacancy and anti-site defects.[300,301] However, deep traps have been found to occur in BiI_3,[276] SbI_3,[276] $Cs_2AgBiBr_6$ double perovskites,[277] BiSI,[302] BiSeI,[302] and Sb_2Se_3.[285] In some cases, for example, for $Cs_2AgBiBr_6$, the contribution of the ns^2 cation valence s orbital to the valence band density of states is small compared to the contribution of orbitals from other species (e.g., directional d orbitals), and these other orbitals therefore dominate the electronic structure at the band-edges. As another example, Saparov et al. found that $Cs_3Sb_2I_9$ had deeper donor trap levels than LHPs because the Sb 5p orbitals were more localized, resulting in the conduction band minimum being pushed up.[242] Therefore, further, refined design rules for defect tolerance are needed.

A recent refined description of defect tolerance was based on chemical effects (illustrated in **Figure 27**). It was proposed that shallow cation vacancies are favored if there is closer alignment between the energies of the cation s and anion p orbitals. This results in increased bonding-antibonding state splitting in the upper valence band. When a cation vacancy forms, the anion dangling bonds interact to form the trap state close to the valence band maximum. A wider valence band leads to an increased likelihood of the trap level being shallow, and this was confirmed in computational investigations into binary halides.[276] If there were strong coupling between the empty cation p orbital and the upper-lying anion s orbital, then this design rule may also be extended to anion vacancies (which form trap levels close to the conduction band minimum). However, the anion s orbital energy is too high in energy for there to be any significant electronic coupling, and the conduction band minimum is dominated by the antibonding state formed between the cation and anion p orbitals.[276]

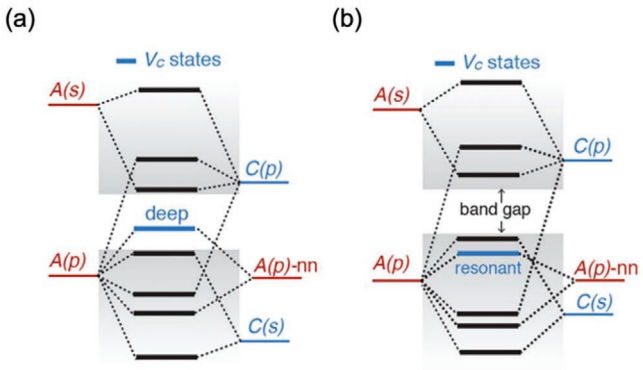

Figure 27. Illustration of how energy alignment between anion (A) *p* and cation (C) *s* states influences the trap energy of cation vacancies. In (a), there is a larger mismatch in A-*p* and C-*s* states than in (b), leading to a lower valence band maximum, and a greater likelihood of deep traps forming. These traps form through the interaction between dangling bonds from neighboring A-*p* states when a cation vacancy is present. Reproduced with permission.[276] Copyright 2018, American Chemical Society.

Recent computational work showed that shallow anion vacancies could be predicted based on structural factors and the structural dimensionality. Anion vacancies in the fully ionized state are positively charged and are donor defects with a transition level close to the conduction band minimum.[32,276,294,300] These defects can trap electrons by localizing them in the unoccupied p orbitals of neighboring cations. The depth of the defect transition level in a covalent semiconductor depends on the degree of hybridization of dangling bonds at the defect center.[294] The addition of an electron to the donor defect will result in a slight contraction of neighboring cations due to Coulomb interactions. The resulting increased hybridization of dangling p orbitals from the cations results in a reduction in the energy of the localized electron. The degree of electronic stabilization relative to the strain energy of the neighboring stretched bonds determines the transition level of the defect. Shallow anion vacancies can then form if orbital hybridization is not strong.[294] This will depend on bond lengths in the crystal structure and atomic coordination.[276,294,303]

Shorter bond lengths result in increased hybridization between dangling bonds, which could lead to deep traps forming (**Figure 28**a). This was illustrated in a recent computational work on $MAPbX_3$ by Kim et al., but the results could be applicable to other systems.[303] Changing the halide in $MAPbX_3$ from I^- to Br^- to Cl^- results in a decrease in the lattice parameter, and a transformation of the halide vacancy from a shallow state in $MAPbI_3$ and $MAPbBr_3$ to a localized deep state in $MAPbCl_3$.[303]

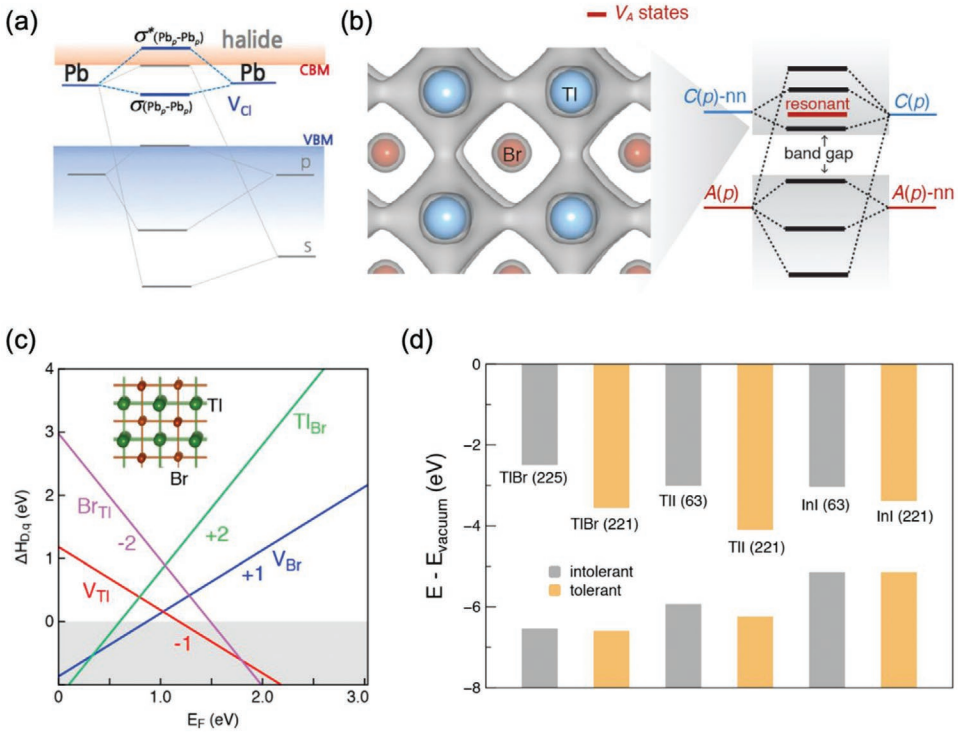

Figure 28. Role of structural dimensionality on defect tolerance. a) Electronic structure of $MAPbCl_3$, showing how Cl vacancies result in the interaction of dangling bonds from neighboring Pb 6p states, forming the vacancy trap level from the bonding orbital. Reproduced with permission.[303] Copyright 2016, PCCP Owner Societies. b) Charge densities profiles of TlBr in the CsCl crystal structure, along with a sketch of the band structure, showing how anion vacancies would be resonant within the conduction band. c) Defect diagram of TlBr in the CsCl structure under Br-rich conditions, and d) band diagram of TlBr, TlI, and InI in the rocksalt/orthorhombic (gray; defect-intolerant) and CsCl structures (yellow; defect-tolerant). b–d) Reproduced with permission.[276] Copyright 2018, American Chemical Society.

This is consistent with experimental work, which has shown Cl-based perovskites to have lower PLQEs than their I- or Br-based counterparts.[304,305] Kim et al. showed that when the lattice constant of the $[PbCl_3]^-$ sub-lattice was increased to that of $[PbI_3]^-$, the bonding states formed by the hybridization of dangling Pb 6p orbitals forms within the conduction band, which would therefore favor shallow anion vacancy transition levels.[303]

Atomic coordination determines the extent and nature of orbital hybridization. For example, it was shown that TlBr in the CsCl crystal structure forms shallow anion vacancies (Figure 28b), whereas TlBr in the rocksalt structure forms deep anion vacancies.[306] In the CsCl structure, each Br is coordinated with 8 Tl. The p orbitals from Br then point to the face centers of the coordination cube rather than the vertices, resulting in orbital interactions being stronger between Tl rather than with Br, with the conduction band minimum almost exclusively comprising cation states (Figure 28b).[276,306] Thus, no cation dangling bonds are exposed when anion vacancies form, and the anion vacancy transition levels are resonant within the conduction band (Figure 28b,c).[276] On the other hand, in the rocksalt structure, Br has 6-fold coordination with Tl, and the Br p orbitals point to the vertices of the coordination cube and significantly contribute to the states at the conduction band minimum.[276,306] Br vacancies will then result in deep transition levels due to the strong interaction of Tl dangling bonds pointing to the center of the octahedron. How deep the transition level is will then also depend on the relative sizes of the cations and anions. For example, shallow anion vacancies can still be formed if the anions are large and cations small, such that there are still low interactions between cation dangling bonds when anion vacancies form (e.g., Cu_3N).[276,307] To illustrate the importance of anion coordination and crystal site symmetry, it was shown computationally that while InI and TlI form deep I vacancies in their native layered structures (in which each I is 5-fold coordinated), these anion vacancies become shallow in the CsCl structure (Figure 28d).[276]

Reducing the anion coordination from octahedral to tetrahedral also generally favors deeper transition level formation. This is because tetrahedrally coordinated materials have shorter bond lengths than octahedrally coordinated materials, and the size of the ions have a less significant effect on how deep the transition levels are,[276] but reducing the anion coordination further to two-fold can instead favor shallow defect transition levels by promoting large cation spatial separation, especially if the anions are large. For example, in comparing $MAPbI_3$ and PbI_2, the band-edges are chemically similar because the MA^+ does not contribute orbitals to the band-edges. However, in $MAPbI_3$, each I is two-fold coordinated by Pb (**Figure 29**a), and I vacancies are shallow. By contrast, in PbI_2, I is 3-fold coordinated (Figure 29b) and deep I vacancies were found to form from defect calculations. Computations of a hypothetical structure of PbI_2 with two-fold I coordination shows that the I vacancy transition level does not form within the band gap (Figure 29c).[276] Thus, although MA^+ does not affect the band-edge density of

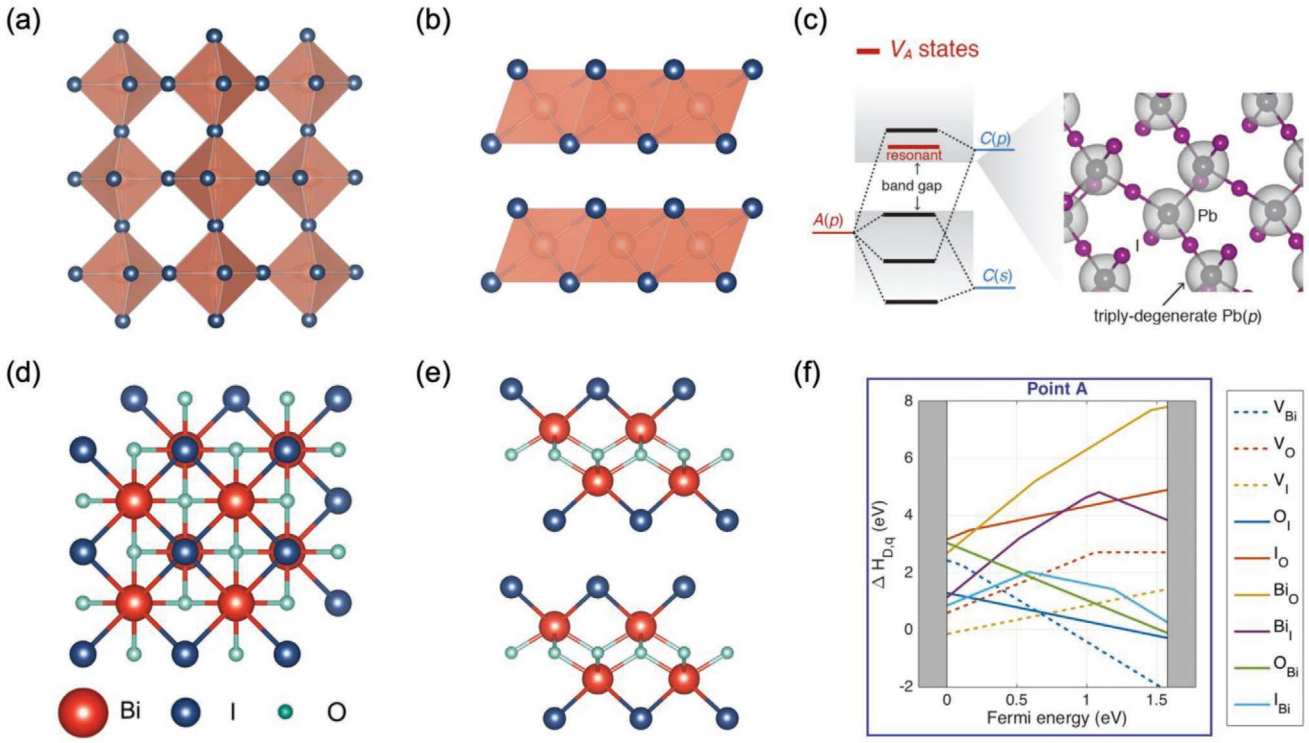

Figure 29. Structure of a) $MAPbI_3$ and b) PbI_2, along with c) a hypothetical structure of PbI_2, in which the coordination of the I^- anions is reduced to two. c) Reproduced with permission.[276] Copyright 2018, American Chemical Society. Structure and defect diagram of BiOI. Ball-and-stick diagram of the crystal structure of BiOI viewed along the d) [001] projection and e) [100] projection. f) Defect diagram of BiOI under I-rich conditions. Reproduced under the terms of the CC-BY license.[300] Copyright 2017, Wiley.

states, it plays an important role in enabling a perovskite crystal structure to form, which is favorable for shallow anion vacancy formation. It has also been suggested that the low anion coordination in layered Bi- and Sb-based chalcohalides favor shallow anion vacancy formation.[308] Shallow Se and Br vacancies have indeed been found for BiSeBr,[308] as well as for the I vacancy in BiOI.[300] However, in BiOI, each O is tetrahedrally-coordinated with Bi, and the oxygen vacancy was found to be deep (Figure 29d–f).[300]

The dimensionality of the materials also affects carrier capture. The Coulomb interaction between charge carriers and charged defect states are accounted for by the Sommerfeld factor $\langle s \rangle$, and the increase in the speed of carrier capture compared to a neutral defect is accounted for by multiplying the capture coefficient with $\langle s \rangle$.[299,309]

For Z < 0,[309]

$$\langle s \rangle = 4|Z|\left(\pi E_R / k_B T\right)^{1/2} \tag{7}$$

For Z > 0,[309]

$$\langle s \rangle = 8/\sqrt{3}\left(\pi^2 Z^2 E_R / k_B T\right)^{2/3} \exp\left(-3\left(Z^2 \pi^2 E_R / k_B T\right)^{1/3}\right) \tag{8}$$

In Equations (7) and (8), $Z = Q/q$, where Q is the charge state of the defect and q is the charge of the electron. k_B is Boltzmann's constant and T temperature. E_R is the effective Rydberg energy, as given by Equation (9).[299,309]

$$E_R = m^* q^4 / 2\hbar^2 \varepsilon^2 \tag{9}$$

In Equation (9), m^* is the carrier effective mass, ħ the reduced Planck's constant, and ε the low-frequency dielectric constant.[309] From these expressions, it can be seen that a low Sommerfeld factor is favored if the material has a low effective mass, as well as materials with high dielectric constants (as discussed earlier). Reducing the dimensionality of the materials can therefore result in higher capture coefficients for charged defects if band dispersion is reduced. Another important factor is the oxidation state of the ions present in the material. Compounds with ions in lower oxidation states have lower maximum $|Z|$ values that the defects could take, thus lowering the Sommerfeld factor.[294]

Finally, it is noted that Cs_2SnI_6 adopts a significantly different electronic structure than $MAPbI_3$, but has nevertheless been found computationally to be defect tolerant (**Figure 30**).[236,278] In Cs_2SnI_6, Sn has a +4 formal oxidation state, however, some computational papers suggest that electrons occupy the 5s orbitals due to the strong covalency of the Sn-I bonds, and that the true valence of the Sn in the compound is +2.[310,311] However, this remains under debate.[236] Nevertheless, in Cs_2SnI_6, the valence band maximum is formed from I 5p non-bonding states, while the conduction band minimum is due to the anti-bonding state from the hybridization of Sn 5s and I 5p orbitals.[236,311] Tin vacancies are predicted to still form at similar energies relative to the Sn-I antibonding orbital (i.e., at similar energies as $CsSnI_3$), but the Sn-I antibonding orbital state is not the conduction band minimum, and the tin vacancy is therefore predicted to form

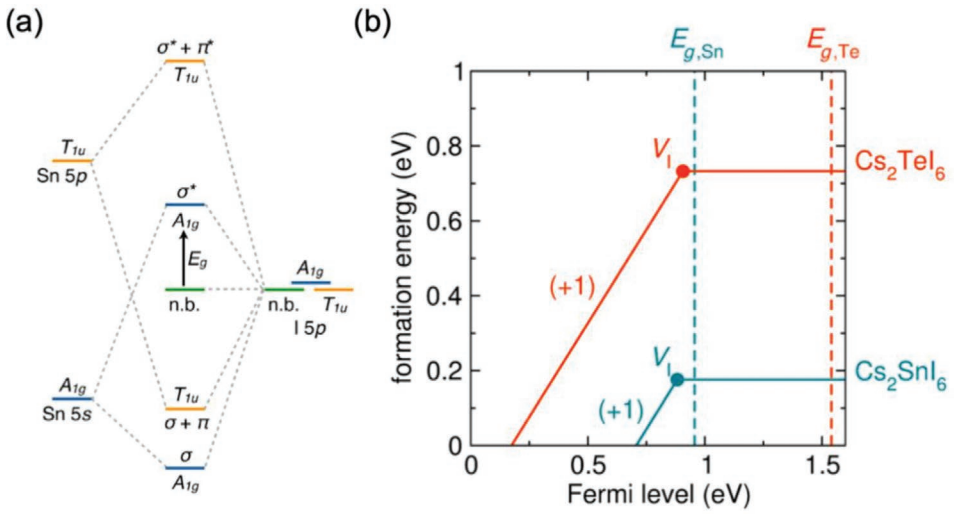

Figure 30. Band structure and defect tolerance in vacancy ordered double perovskites. a) Frontier states in Cs_2SnI_6, and b) defect diagram for Cs_2SnI_6 compared to Cs_2TeI_6 for the iodine vacancy. a) Reproduced with permission.[236] Copyright 2019, American Chemical Society. b) Reproduced under the terms of the CC-BY license.[278] Copyright 2016, American Chemical Society.

a transition level within the band gap but close to the conduction band minimum.[311] This shows that compounds with ns^2 cations would still be important for achieving tolerance to cation vacancies,[276] but in the case of Cs_2SnI_6, the strong Sn-I covalency results in tin vacancies having a high formation energy and therefore not likely to form under thermodynamic conditions.[311] Owing to the small band gap of only 1.3 eV, I vacancies are predicted to be shallow in Cs_2SnI_6.[236,278] However, defect tolerance is lost when changing the Sn cation to Te or cations with valence *d* orbitals (e.g., Ti).[236,278] The interaction between Te 5p and I 5p orbitals pushes up the antibonding state, and therefore pushes up the conduction band minimum. The wider band gap leads to the I vacancy being deep.[236,278] The defect intolerance of Cs_2TiI_6 is attributed to the large number of possible oxidation states and relatively localized d states.[236]

4.3. Challenges of Anisotropy on Device Performance

From the discussion in Sections 4.1 to 4.2, it is evident that the exploration of PIMs has led to materials with dimensionality ranging from 0D to 3D, with the lower dimensional materials offering important advantages in terms of stability and possibly reduced surface recombination. However, lowering the structural or electronic dimensionality below 3D leads to anisotropic charge-carrier properties, which needs to be accounted for in processing the materials for devices.

4.3.1. Photovoltaics

The structure of PIM-based PVs is similar to those used for LHPs. That is, the absorber is sandwiched with electron and hole transport layers (ETLs and HTLs, respectively). The band positions of the PIMs discussed compared to common ETLs and HTLs are shown in **Figure 31**c.

From Section 4.1, it can be seen that 3D structural and electronic dimensionality are favorable for achieving low effective masses (which favor higher mobilities and lower Sommerfeld factors) and low exciton binding energies. Sn-based perovskites (i.e., $ASnX_3$) fulfill these requirements, and have achieved the highest PCEs among the lead-free PIMs (Table 2),[233,294,32] with PCEs reaching 12.4% for solar cells based on $PEA_{0.15}FA_{0.85}SnI_3$ (device structure: ITO/PEDOT:PSS/$PEA_{0.15}FA_{0.85}SnI_3$/ICBA/BCP/Ag).[327] While Ge-based perovskites also have 3D structural dimensionality, the electronic dimensionality is lower due to structural distortions in the $[GeI_6]^{4-}$ octahedra, and Ge-I-based perovskites have wider band gaps (of 1.5–2.3 eV)[233,294] than Sn-I-based perovskites (of 1.3–1.4 eV)[233] and higher effective masses (refer to Section 4.1.4 and Table 2). Ge-based PVs have demonstrated low PCEs so far, reaching only 0.68% for $MAGeI_{2.7}Br_{0.3}$ PVs (device structure: ITO/PEDOT:PSS/$MAGeI_{2.7}Br_{0.3}$/$PC_{71}BM$/Ag).[328] Both Ge- and Sn-based perovskites suffer from low stability, in which the metal cation can easily be oxidized from the 2+ to 4+ state.[233,294,323] Extensive efforts have been made with the Sn-based system to address this, and stable device performance in air without encapsulation for several days has been achieved through the addition of SnF_2 and ethylenediammonium iodide, as well as alloying the A-site cation with GA, as well as long-chain alkylammonium cations (e.g., mixing FA and PEA, as mentioned above).[233,323] Alloying $CsGeI_3$ with Sn has been shown to improve stability (as well as performance) compared to pure Ge-based perovskites, but this was attributed to the formation of a thin surface layer of GeO_2.[325] Silver-bismuth double perovskites, with 3D structural dimensionality, have also been found to be stable in air.[34,329] However, the reduced electronic dimensionality (see Section 4.1.4) leads to a wide (>2 eV), indirect band gap that limits light absorption (Figure 31c). As a result, the maximum efficiencies expected based on their absorption spectra are well below the PCEs already achieved with silicon or LHP PVs.[287] $Cs_2AgBiBr_6$ is by far the most common double perovskite investigated so far for PVs, and most PCEs are ≈1%, with the highest value only 2.8% (FTO/TiO_2/m-TiO_2/$Cs_2AgBiBr_6$/N719/spiro-OMeTAD/Ag).[330] Routes to reducing the optical band

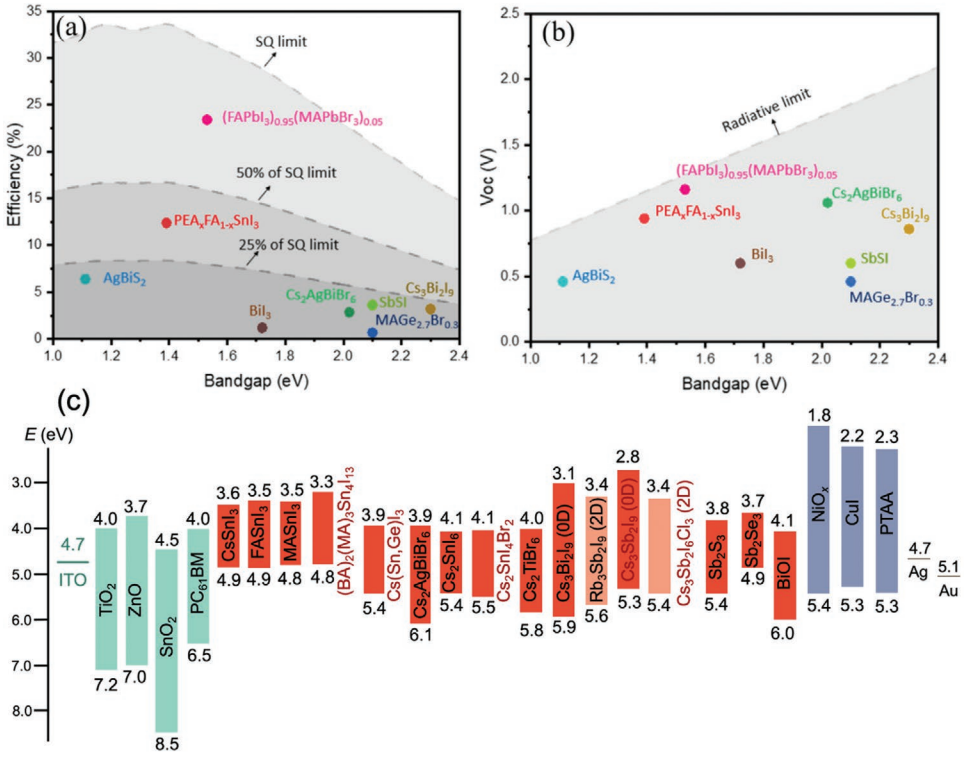

Figure 31. a) Power conversion efficiency and b) open-circuit voltage (V_{OC}) of perovskite-inspired materials compared to the radiative limit (or Shockley–Queisser, SQ, limit). Reproduced under the terms of the CC-BY license.[294] Copyright 2021, IOP Publishing. c) Band positions of perovskite-inspired materials discussed in Section 4.3.1. Values extracted from refs. [33,35,259,312–326].

gap and increasing the absorption coefficient without the use of toxic elements (e.g., Tl),[329] while maintaining high air-stability, are needed. Recently, it was found that one route to achieving this is to alloy two double perovskites that form a type II staggered junction. Non-linear mixing of the metal cation orbitals can result in the alloys adopting a smaller band gap than either of the pure compounds.[35]

Similarly, defect-ordered perovskites (i.e., $A_3B_2X_9$) that are structurally and electronically 0D adopt wide band gaps (Figure 31c). Owing to the low electronic dimensionality, high exciton binding energies and low effective masses occur (refer to Section 4.1), and low PCEs of up to only approximately 1–2% have been achieved in most cases (Table 2).[331] The main exceptions are $Cs_3Bi_2I_9$ and $(MA)_3Bi_2I_9$, for which efficiencies reaching 3.2% have been achieved.[317,332] In the case of $Cs_3Bi_2I_9$, the high efficiency was achieved in part due to the use of CuI as the HTL, rather than the more commonly used PTAA and spiro-OMeTAD HTLs. CuI has a high ionization potential of 5.3 eV, which is better matched with the valence band maximum of $Cs_3Bi_2I_9$ (5.7 eV ionization potential; Figure 31c).[317] The final device structure that gave the highest efficiency was FTO/TiO_2/$Cs_3Bi_2I_9$/CuI/Au.[317] In the case of $(MA)_3Bi_2I_9$, the high device efficiencies of up to 3.17% were attributed to the optimization in the processing method to achieve improved morphology and stoichiometry, with reduced bulk metallic content. The device structure used was FTO/TiO_2/m-TiO_2/$(MA)_3Bi_2I_9$/P3HT/Au.[332]

In contrast to the structurally 0D $A_3B_2X_9$ materials, Cs_2SnI_6 has higher band dispersion (see Section 4.1 and Table 2), and high hole mobilities of 42 $cm^2\ V^{-1}\ s^{-1}$ have been reported, along with the demonstration of Cs_2SnI_6 as an effect HTL in dye-sensitized solar cells, with PCEs up to 7.8% achieved.[293] Cs_2SnI_6 has also been recently demonstrated as the absorber in PV devices, which achieved 1.47% PCE.[326] The short-circuit current density (J_{SC}) of these devices reached 6.8 mA cm^{-2},[326] which is higher than the values achieved by $A_3B_2I_9$ PVs (where B = Bi or Sb).[294,331] This is consistent with the band gap of Cs_2SnI_6 (1.3 eV) being smaller than those of the $A_3B_2I_9$ compounds (Figure 31c). However, the open-circuit voltage (V_{OC}) of the Cs_2SnI_6 is well below the band gap, and the fill factors of 60% are not higher than the fill factors that have been achieved with the best $A_3B_2I_9$ PVs.[331] Improvements in the performance of the vacancy-ordered double perovskite devices were achieved by alloying with Br. $Cs_2SnI_4Br_2$ has a band gap of 1.4 eV (Figure 31c), which leads to a small decrease in J_{SC} to 6.2 mA cm^{-2} but an improvement in V_{OC} from 0.37 V (Cs_2SnI_6) to 0.56 V ($Cs_2SnBr_2I_4$) while the fill factor only decreased to 58%. The PCE increased to 2.1%.[326] For both the Cs_2SnI_6 and $Cs_2SnBr_2I_4$ devices, the device structure was FTO/TiO_2/Sn:TiO_2/$Cs_2SnBr_xI_{6-x}$/LPAH/FTO, where LPAH is large area polyaromatic hydrocarbon.[326] Higher PCEs have been achieved with Cs_2TiBr_6, in which a PCE of 3.3% has been demonstrated (device structure: FTO/TiO_2/C_{60}/Cs_2TiBr_6/P3HT/Au).[312] These Ti-bromide-based vacancy-ordered double perovskites have a wider band gap of 1.82 eV (Figure 31c), but the devices still achieved a J_{SC} of 5.7 mA cm^{-2} and a substantially larger V_{OC} of 1.02 V, along with a comparable fill factor of 56%.[312] Thus, substantial optimization of the absorber, interfaces, and device structure is needed before the predicted defect-tolerant properties and

dispersive band structure of Cs_2SnI_6 are manifest in improved device performance. Notably, Cs_2SnI_6 PVs have been found to be stable in air,[326] as have Cs_2TiBr_6 and $A_3B_2I_9$ PVs.[294,312,331]

As discussed in Section 4.1, the mobility of $A_3B_2I_9$ compounds can be increased, and the exciton binding energy reduced by stabilizing the 2D polymorph instead of the 0D polymorph, and this can be achieved by changing the A-site cation or through halide alloying. Works systematically comparing 0D and 2D $A_3B_2I_9$ compounds have shown the 2D polymorphs to give improved performance. For example, Correa-Baena et al. showed that 2D $Rb_3Sb_2I_9$ PVs delivered improved PCEs over 0D $Cs_3Sb_2I_9$ (0.76% *cf.* 0.03%, respectively). This was due to an order-of-magnitude improvement in the J_{SC} from 0.13 mA cm^{-2} (0D $Cs_3Sb_2I_9$) to 1.84 mA cm^{-2} (2D $Rb_3Sb_2I_9$), which arose from the direct band gap of $Rb_3Sb_2I_9$ (compared to the indirect band gap for $Cs_3Sb_2I_9$), as well as lower exciton binding energies of 95–107 meV (compared to 166–184 meV for $Cs_3Sb_2I_9$).[253] For all three materials, the device structure was FTO/TiO_2/m-TiO_2/$A_3Sb_2I_9$/spiro-OMeTAD/Au.[253] Subsequent work on improving the grain size of $Rb_3Sb_2I_9$ led to the PCE increasing to 1.35% (device structure: FTO/TiO_2/$Rb_3Sb_2I_9$/poly-TPD/Au).[316] Furthermore, Peng et al. showed that alloying Cl into $Cs_3Sb_2I_9$ to stabilize the 2D phase led to the PCE improving from 0.24% to 2.15% due to the J_{SC} increasing from 1.37 mA cm^{-2} to 6.46 mA cm^{-2} (device structure: FTO/TiO_2/$Cs_3Sb_2I_9$/poly-TPD/Au or FTO/TiO_2/$Cs_3Sb_2I_{9-x}Cl_x$/LZ-HTL-1-1/Au).[259] The performance improvement can be primarily attributed to an increase in the absorption coefficient (due to the band gap changing from indirect to nearly direct),[242] a reduction in the exciton binding energy, and increase in mobility.[259] Despite these improvements in performance, the PCEs have not yet exceeded the highest PCEs reported for 0D $A_3B_2I_9$ compounds (Table 2),[259,317,331,333,336] and further optimization in the processing of the absorber and the ETLs/HTLs used are needed.

For 1D and 2D materials in vertically structured PV devices, it is critical to control the preferred orientation and density of the grains in order to achieve efficient charge-carrier extraction. As discussed in Section 4.1, the transport properties can be highly anisotropic, and it is important to connect the top and bottom electrodes with the higher-mobility planes. In solution-processed materials, control over the preferred orientation has been extensively studied in 2D and quasi-2D Sn-based perovskites. It has been found that the preferred orientation can be tuned through the precursor composition, as well as the solvent used.[324,334,335] Liao et al. found that using 1:4 phenethylammonium iodide (PEAI):formamidinium iodide (FAI) resulted in quasi-2D tin-iodide-based perovskites with the inorganic layers oriented perpendicular to the substrate. This was favorable for efficient carrier extraction, and the $(PEA)_2(FA)_{n-1}Sn_nI_{3n+1}$ films achieved EQEs reaching approximately 60%, and PCEs reaching up to 5.94%, which was improved over the $FASnI_3$ PVs (1.2% PCE).[335] In both cases, the device structure was ITO/NiO_x/Sn-based perovskite/PCBM/Al.[335] $(PEA)_2(FA)_{n-1}Sn_nI_{3n+1}$ films with higher fractions of PEAI had less preferred orientation. The precise mechanism is unknown, but similar observations have been made with quasi-2D Pb-based perovskites.[336] Cao et al. found that the preferred orientation of $(BA)_2(MA)_{n-1}Sn_nI_{3n+1}$ perovskites depended on the solvents used (**Figure 32**).

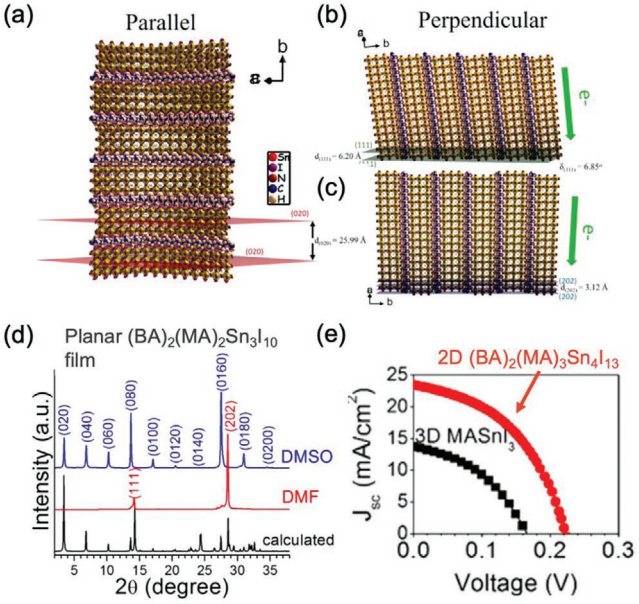

Figure 32. Controlling the preferred orientation of solution-processed $(BA)_2(MA)_{n-1}Sn_nI_{3n+1}$ quasi-2D/3D perovskites. BA is butylammonium and MA is methylammonium. Structure of $(BA)_2(MA)_2Sn_3I_{10}$ perovskites a) in the (0k0) orientation parallel to the substrate, and in the b) (111) and c) (202) orientations perpendicular to the substrate. d) X-ray diffraction patterns of $(BA)_2(MA)_2Sn_3I_{10}$ perovskites showing the effect of solvent on preferred orientation. e) Comparison of the performance of photovoltaic devices made from $MASnI_3$ and $(BA)_2(MA)_3Sn_4I_{13}$. Reproduced with permission.[324] Copyright 2017, American Chemical Society.

Using only *N*,*N*–dimethylformamide (DMF) as the solvent resulted in the $[Sn_nI_{3n+1}]^{(n+1)-}$ inorganic planes being vertically oriented. By contrast, using a mixture of 4:1 dimethylsulfoxide (DMSO):DMF resulted in the inorganic planes being oriented parallel to the substrate. This was attributed to DMSO giving rise to improved surface wetting and the precursor solvent spreading out more on the planar TiO_2 substrate, as well as the formation of the intermediate complexes between DMSO and the Sn-based precursor.[324] The degree of preferred orientation was enhanced by hot-casting at 120 °C, in which the perovskite is spin-coated at 120 °C rather than at room temperature.[324] Using quasi-2D perovskites with $n = 4$, PCEs up to 2.53% were achieved (band positions in Figure 32e).[324] The device structure was FTO/TiO_2/m-TiO_2/Sn-perovskite/PTAA/Au. The increase in preferred orientation with hot-casting is consistent with results with quasi-2D Pb-based perovskites,[141] but the effect of the solvents is opposite (in which increasing DMSO content was found to increase the vertical orientation of quasi-2D Pb-based perovskites).[336]

Effort has also been made to control the preferred orientation of PIMs grown from the vapor-phase, especially for $Sb_2(S,Se)_3$ and BiOI, which are structurally 1D and 2D materials, respectively.[283,300,337–339] We note that while $Sb_2(S,Se)_3$ and BiOI are not perovskites and do not have metal-anion octahedra, they are perovskite-inspired materials because they comprise metal cations that have a stable pair of valence electrons, whose orbitals hybridize with the anion orbitals in a similar way to LHPs.[15,106] As discussed in Section 4.2, this is one important features that may contribute to defect tolerance. In Sb_2S_3 and Sb_2Se_3, the

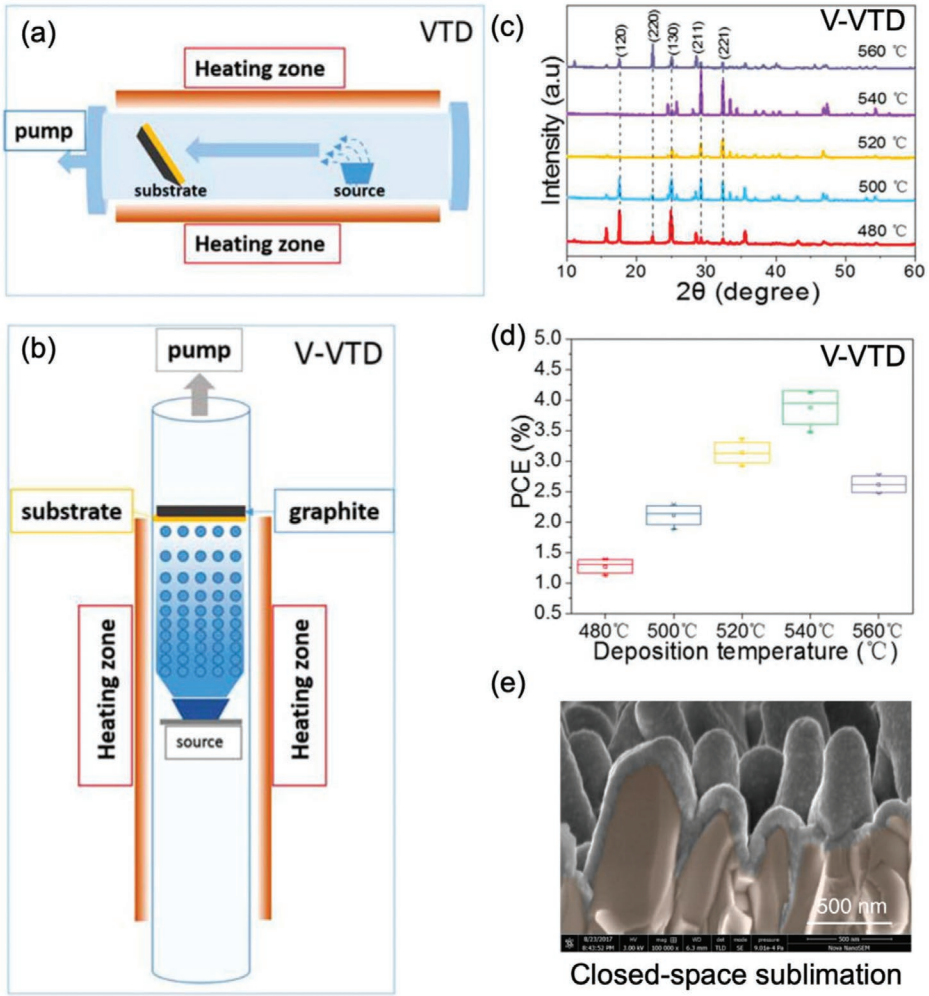

Figure 33. Vapor-phase growth of $Sb_2(S,Se)_3$. Illustration of a) vapor transport deposition (VTD) and b) vertical vapor transport deposition (V-VTD) reactors. c) X-ray diffraction patterns of Sb_2S_3 films deposited on CdS by V-VTD at different source temperatures (the CdS substrate was at a lower temperature), and d) the power conversion efficiencies (PCEs) of the resulting devices. Reproduced with permission.[339] Copyright 2020, Wiley. e) Cross-sectional scanning electron micrograph of Sb_2Se_3 nanorods grown by closed-space sublimation (CSS) and conformally covered with CdS by chemical bath deposition. Reproduced under the terms of the CC-BY license.[341] Copyright 2019, Springer Nature.

mobility along the inorganic $(Sb_4(S,Se)_6)_n$ ribbons ([hk1] directions) is an order of magnitude larger than between ribbons ([hk0] directions).[339] Reducing the texture coefficient for the [120] direction has therefore been shown to lead to an increase in efficiency due to a reduction in the series resistance, as the higher-mobility inorganic ribbons connect the top and bottom electrodes.[283] One of the common vapor-based methods to grow these materials is vapor transport deposition (VTD), in which the source powder (Sb_2S_3 or Sb_2Se_3) is evaporated and transported to the substrate.[339,340] The important factors for controlling the orientation and crystallinity of the films were thought to be the kinetic energy of the vapor particles and the mobility of adatoms on the substrate. These could be controlled by the evaporation temperature, source-to-substrate distance, and the pressure during growth.[340] By carefully optimizing these three parameters, Wen et al. were able to achieve 7.6%-efficient Sb_2Se_3 PVs with (221) preferred orientation (device structure: ITO/CdS/Sb_2Se_3/Au).[340] Zhang et al. modified the VTD method (**Figure 33**a) by using a vertical furnace rather than a horizontal furnace. Termed vertical VTD (V-VTD; Figure 33b), the source powder of Sb_2S_3 was evaporated directly beneath the substrate. They found that [hk1] preferred orientation was favored at higher evaporation (and deposition) temperatures, up to a source temperature of 540 °C. At higher temperature, the re-evaporation rate exceeded the deposition rate, and voids formed in the films, along with the (220) orientation being favored.[339] Over the 480–540 °C source temperature range, when the deposition rate was higher than the re-evaporation rate, the increase in the (221) and (221) texture coefficients with increasing temperature was attributed to faster growth along the [hkl] directions (Figure 33c). Changing the orientation from [hk0] to [hk1] increased the PCEs of the Sb_2S_3 PVs from 1.3% to 4.0% (Figure 33d).[339] Beyond VTD and V-VTD, closed-space sublimation (CSS) has also been used to grow Sb_2Se_3, in which the source and substrate are maintained with a small spacing of 11 mm.[341] In this technique, it was found a compact layer of Sb_2Se_3 films, followed by the growth of [001]-oriented Sb_2Se_3 nanorod arrays to relieve the internal stress formed in the growing Sb_2Se_3 layer (Figure 33e).[341] These PVs

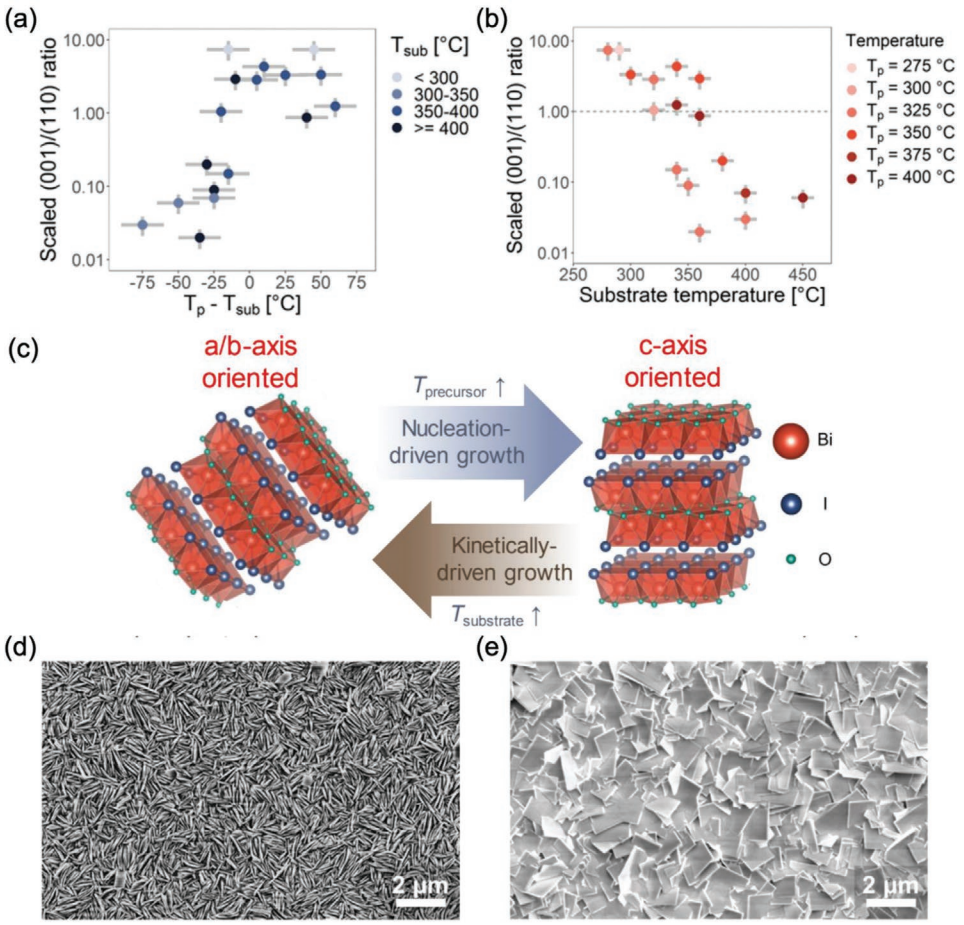

Figure 34. Controlling the preferred orientation of BiOI. a) Effect of substrate temperature and b) difference between precursor (T_p) and substrate (T_{sub}) temperatures on the scaled (001)/(110) intensity ratio. In the scaled intensity ratio, the ratio of the (001) and (110) diffraction peak intensities is multiplied by the ratio of the (110) and (001) diffraction peaks if there was no preferred orientation, that is, a scaled intensity ratio of 1.0 implies that there is no preferred orientation. c) Illustration of the model for how the preferred orientation of BiOI can be changed. Scanning electron micrographs of d) *a*/*b*-axis oriented and e) *c*-axis oriented BiOI. Reproduced with permission.[338] Copyright 2020, Published by the Royal Society of Chemistry.

exhibited 9.2% PCE and the device structure was Al:ZnO/ZnO/CdS/TiO_2/Sb_2Se_3/$MoSe_2$/Mo.

In contrast to the physical vapor deposition approaches for $Sb_2(S,Se)_3$, BiOI has been grown by thermal chemical vapor deposition (t-CVD), in which BiI_3 is vaporized and reacts with O_2 gas to form BiOI.[300,301,338] It should be noted that in the unit cell of BiOI, the inorganic layers are arranged perpendicular to the ribbons in $Sb_2(S,Se)_3$, such that the [hk1] direction is perpendicular to the layers. The t-CVD BiOI films initially had no preferred orientation, but as the films grew, the films adopted either a [001] (c-axis) or [hk0] (a/b-axis) preferred orientation, depending on the growth regime: nucleation-driven or kinetically driven. The growth regime that dominates can be controlled by the precursor and substrate temperatures. At higher precursor temperatures, the supersaturation of the BiI_3 precursor is high, which favors the nucleation-driven regime (**Figure 34**a). It is thermodynamically favored for BiOI platelets to nucleate layer-by-layer, since there are no dangling bonds. Nucleation-driven growth therefore favors *c*-axis oriented BiOI. By contrast, at higher substrate temperatures, kinetically driven growth is favored, in which the platelets preferentially grow from existing grains, which would occur along the *a*/*b*-axis directions (Figure 34b), which are terminated by dangling bonds. The effects of the precursor and substrate temperatures on preferred orientation is summarized in Figure 34c. The preferred orientation of BiOI not only affect carrier transport, but also the morphology of the films owing to the platelet structure of BiOI. *a*/*b*-axis oriented BiOI has an open structure that results in reduced shunt resistance (Figure 34d). By contrast, *c*-axis oriented BiOI has a closed structure with higher shunt resistance (Figure 34e), leading to increased V_{OC}s in PVs, but carrier extraction is inefficient in the c-axis direction in BiOI, and higher PCEs (up to 1.8%) are achieved in the *a*/*b*-axis orientation of BiOI (device structure: ITO/NiO_x/BiOI/ZnO/Al).[300,338] Combining *c*-axis with *a*/*b*-axis oriented BiOI (as in CSS-grown Sb_2Se_3) may overcome these challenges.

4.3.2. Light-Emitting Diodes

Although lead-halide perovskites have achieved PLQEs approaching unity, and LED EQEs exceeding 20% already,

with ultrasharp, color-pure electroluminescence, these features have not been matched by the lead-free alternatives.[17,294,342,343] Some of the causes include the oxidation of Sn^{2+} to Sn^{4+} in $CsSnX_3$,[343] and the indirect nature of the band gap of Bi- and Sb-based materials, which all give rise to low PLQEs that are typically <1%, but recent work has shown that the latter challenge could be addressed by lowering the structural and form factor dimensionality to induce quantum confinement in 0D $A_3B_2X_9$ (B = Bi^{3+}, Sb^{3+}) quantum dots (QDs).[342–345] PLQEs of 46%, 19.4%, and 12% have been achieved in $Cs_3Sb_2Br_9$, $Cs_3Bi_2Br_9$, and $(MA)_3Bi_2Br_9$ QDs, respectively, which are substantially higher than the PLQEs of bulk thin films of these materials.[342–344] These materials all have 2D structural dimensionality, and this leads to increased exciton binding energies compared to 3D materials.[257,342–344] The exciton binding energy is further increased through quantum confinement. For example, Leng et al. found that $Cs_3Bi_2Br_9$ single crystals have an exciton binding energy of 78 meV at room temperature, which increases to 211 meV in QDs.[343] As discussed in Section 4.1.3, the high exciton binding energy results in a majority of the PL emission being due to exciton recombination, and this is believed to contribute to an increased PLQE.[342–344] It has also been suggested that the small size of the QDs results in a reduced likelihood of defects forming, which would also enhance PLQE.[343] However, nanocrystals of 0D $Cs_3Bi_2I_9$ have a PLQE of only ≈1%, which may be due to sub-bandgap states.[257] Another advantage of Bi- and Sb-based defect-ordered perovskites is that they demonstrate improved stability over lead-halide perovskites. It was found that $Cs_3Sb_2Br_9$ QDs form a bromide-rich surface, which is expected to lead to a wider-bandgap shell on the surface that could further enhance PLQEs.[342] $Cs_3Sb_2Br_9$, $Cs_3Bi_2Br_9$, and $(MA)_3Bi_2Br_9$ QDs emit in the violet wavelength range (400–420 nm), and these materials could be used as phosphors, particularly since they have been demonstrated to be substantially more stable than lead-halide perovskites.[342–344] Indeed, $Cs_3Bi_2Br_9$ QDs were used as violet phosphors for UV-emitting GaN LEDs. When combined with $Y_3Al_5O_{12}$ (YAG) phosphors, which gives broad, yellow photoluminescence, white light emitting diodes were achieved, with Commission Internationale de l'éclairage (CIE) coordinates of (0.29, 0.30), which are close to the coordinates of (0.33, 0.33) for pure-white emitters (**Figures 35**a,b).[343] $Cs_3Sb_2Br_9$ QDs were also recently demonstrated in violet LEDs (Figure 35c), which demonstrated 0.2% EQE (Figure 35d) and maintained 90% of their original electroluminescence intensity after 6 h of continuous operation at 7 V applied bias (≈70 mA cm^{-2} current density (Figure 35e).[345] The device structure was ITO/ZnO/PEI/$Cs_3Sb_2Br_9$/TCTA/MoO_x/Al, where PEI is polyethylenimine and TCTA is 4,4′,4″-tris(carbazole-9-yl)triphenylamine.[345]

5. Carrier-Phonon Coupling: The Role of Dimensionality and the Impact on Optoelectronic Properties

Beyond non-radiative recombination due to the role of defects, an important aspect determining the transport properties of halide systems is the coupling between charge-carriers and phonons. Any crystal lattice is deformable and, at room temperature, is vibrating. Lattice vibrations can be described by acoustic phonons or optical phonons, depending on whether the movements are in-phase (acoustic) or out-of-phase (optical) with each other. These vibrations can give rise to the scattering of excited carriers and could influence their non-radiative decay.[346–348] Due to the deformability of the lattice the carriers can locally distort the lattice, thus forming a polaron. Both lead-halide perovskites (LHPs) and perovskite-inspired materials (PIMs) are soft, polar materials containing heavy elements.[32] As discussed in Sections 3 and 4, many classes of these materials have low dimensionality.[338,349] This section discusses the role of coupling between carriers and phonons in LHPs and PIMs, and how dimensionality influences this coupling. We first discuss the fundamentals of electron- and exciton-phonon coupling and the concept of carrier localization. Second, we assess the impact this coupling has on the optoelectronic properties of LHPs and PIMs (including mobility and lifetime). Finally, we discuss the impact on device performance and how self-trapping in semiconductors can be identified.

5.1. Fundamentals of Carrier-Phonon Coupling

5.1.1. Fröhlich coupling

Due to the deformability of the materials, carriers in polar semiconductors can induce a lattice distortion.[350] There are both transverse (TO) and longitudinal (LO) optical phonons depending on whether the vibration is perpendicular or in-line with the direction of propagation. When an electron is placed inside a polar crystal lattice, it locally distorts (polarizes) the lattice, attracting positively charged ions and repulsing negatively charged atoms. This is referred to as a polaron. When an electron moves throughout the lattice, it drags this distortion field along.

Figure 36a shows the movement of an electron inside a $MAPbI_3$ crystal along a [111] direction. For a TO phonon, the MA^+, I^-, Pb^{2+} layers oscillate past each other in their lattice positions, while not changing the interplanar distance. For the LO phonon mode, the interplanar distance between these layers changes. Due to the Coulombic interaction between the layers, there is an energy associated with this change. This interaction causes an increase in the effective mass of the carriers and is called Fröhlich coupling.

The coupling of carriers to LO phonons is expressed in terms of the Fröhlich polaron coupling constant α_{op}, which is given by Equation (10).[350]

$$\alpha_{op} = \frac{q^2}{\hbar}\left(\frac{1}{\varepsilon_\infty} - \frac{1}{\varepsilon_0}\right)\sqrt{\frac{m^*}{2\hbar\omega_{LO}}} \tag{10}$$

where q is the elementary charge, $\hbar$ is the reduced Planck constant, ε_∞ and ε_0 are the dielectric constant at infinite and zero frequency respectively, m^* is the effective mass of the electron or hole, and ω_{LO} is the frequency of the dominant LO phonon.

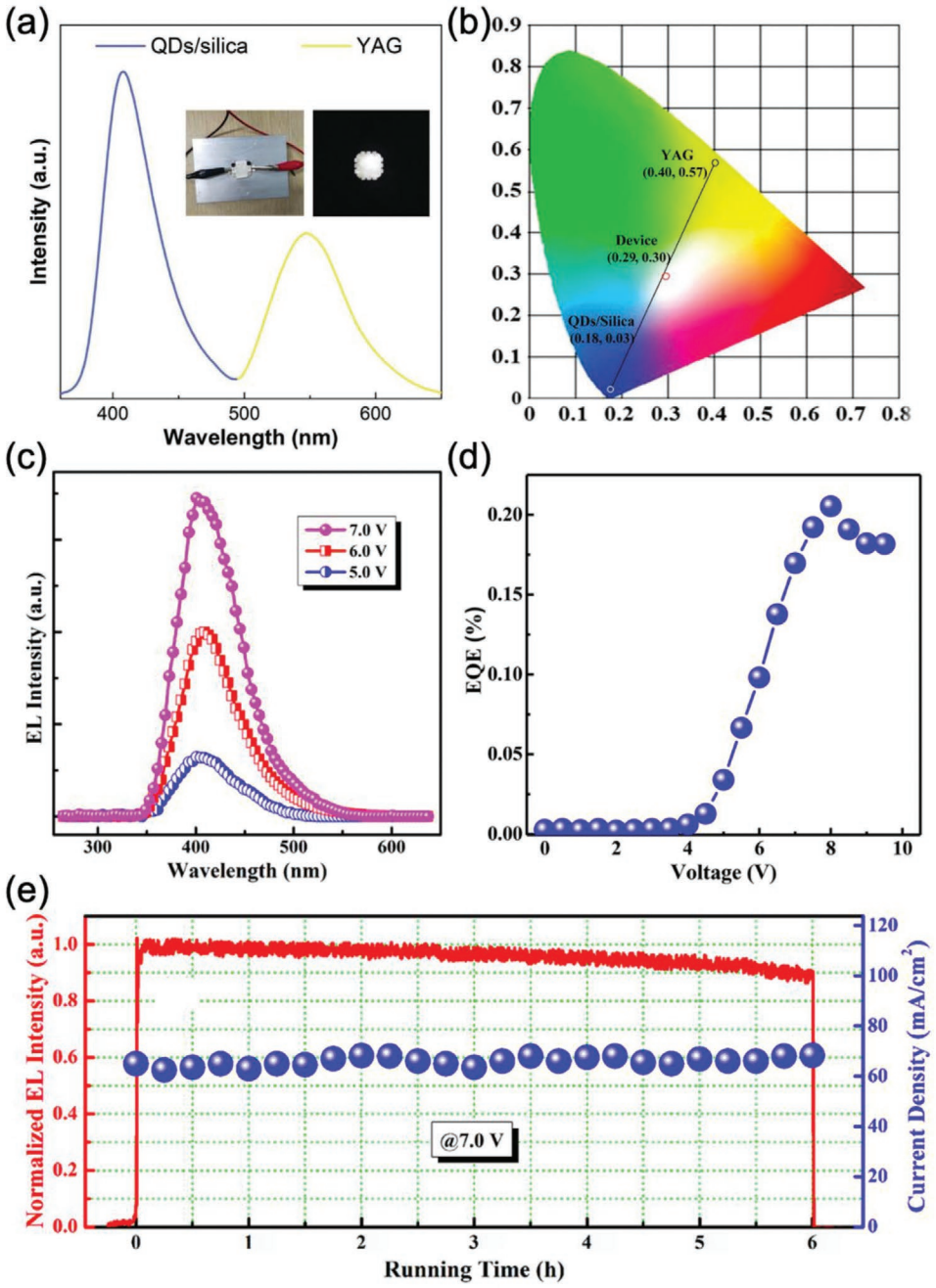

Figure 35. Light-emitting devices from low-dimensional perovskite-inspired materials. a) Electroluminescence (EL) spectrum of $Cs_3Bi_2Br_9$ nanocrystals and YAG phosphor, and b) the CIE coordinates of the white light-emitting diode. Reproduced with permission.[343] Copyright 2018, Wiley. c) Electroluminescence spectrum at different applied biases, and d) external quantum efficiency (EQE) versus applied bias of $Cs_3Sb_2Br_9$ quantum dot light-emitting diodes (LEDs). e) EL intensity, normalized to the initial EL peak, of $Cs_3Sb_2Br_9$ LEDs at 7 V constant bias. Reproduced with permission.[345] Copyright 2020, American Chemical Society.

In non-polar semiconductors, such as Si and Ge, there is no internal electric field, and hence Fröhlich interactions play a minor role. The polar (ionic) nature of LHPs and PIMs leads to higher coupling due to the higher differences between ε_∞ and ε_0 (in LHPs at room temperature $\varepsilon_\infty \gtrsim 5$ and above $\varepsilon_0 \simeq 30$).[149] This leads to intermediate Fröhlich coupling (α between 1.7 and 2.2 for LHPs), giving rise to polarons with radii of approximately a few nanometers, which limits the carrier mobility to ~200 $cm^2\ V^{-1}\ s^{-1}$ in $MAPbI_3$.[351] The natural frequency of a harmonic oscillator is proportional to $\sqrt{k/m}$ (where k is the spring constant and m is the mass). Thus, for semiconductors containing heavy elements the frequency of the longitudinal phonons, ω_{LO}, is reduced and the Fröhlich coupling increases. In the case of excitons, due to their electric neutrality, there is no Fröhlich coupling.

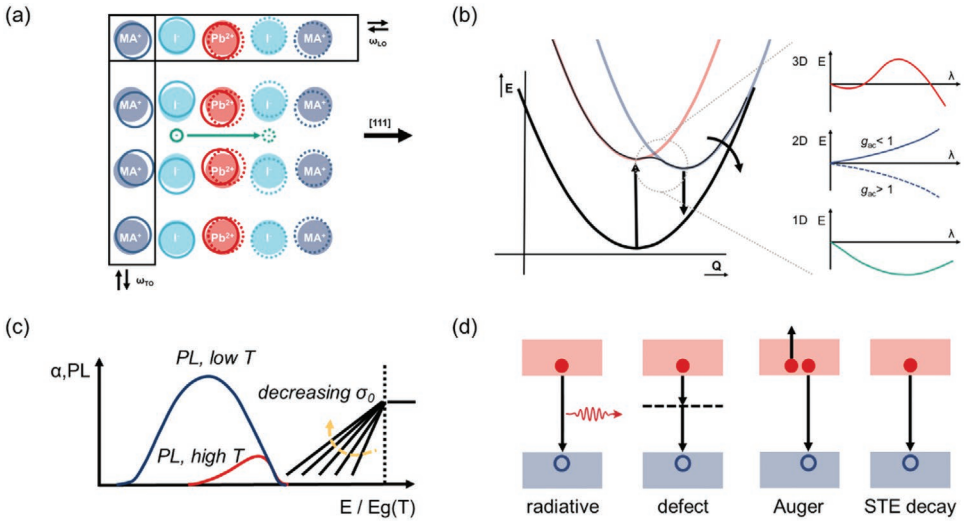

Figure 36. a) Example how an electron (green circle) can cause deformations in the cubic lead-halide perovskite lattice and interact with transverse (TO) and longitudinal (LO) optical phonons. The original (solid line) and final (dashed line) positions of the atoms are shown. b) Configurational coordinate diagram indicating the free (red) and localized (blue) states. Inset: Qualitative description of how the energy barrier based on Equations (13) and (14) depends on the dimensionless parameter λ for the 3D, 2D, and 1D case. c) The absorption profile and photoluminescence of a self-trapped system. Depending on the strength of the coupling to acoustic phonons, there is an absorption edge below the band gap. The photoluminescence is stokes shifted with respect to the band edge and can be strongly temperature dependent. d) Different decay mechanisms in which excited carriers can decay: i) radiatively, ii) through defects, iii) Auger recombination, and iv) non-radiative decay of the self-trapped exciton through direct coupling to the ground state.

5.1.2. Deformation Potential Scattering

In addition to the carrier affecting the lattice, lattice vibrations can also influence the carrier. This is described using deformation potentials.[352] When an atom is displaced from its lattice site, it induces a modification to the band structure. For small displacements due to acoustic phonons, the change in the energy of conduction band edge (∂E_c) can be approximated by Equation (11).[352]

$$\partial E_c = \Xi_{ac} \frac{\partial V}{V} \tag{11}$$

where Ξ_{ac} (eV) is the acoustic deformation potential and δV is the variation of the crystal volume V.

The coupling of carriers to acoustic phonons is expressed in terms of coupling constant α_{ac}, as given by Equation (12).[352]

$$\alpha_{ac} = i\boldsymbol{w}\cdot\boldsymbol{k}\left(\frac{\hbar\Xi_{ac}^2}{2V\rho\omega_q}\right)^{1/2} \tag{12}$$

where $\boldsymbol{w}$ and $\boldsymbol{k}$ are the polarization vector and wave vector of the phonon, respectively; ρ is the mass density; and V is crystal volume.

Similarly, for optical phonons, the coupling term is given by Equation (13).

$$\alpha_{op} = \left(\frac{\hbar\Xi_{op}^2}{2V\rho\omega_q}\right)^{1/2} \tag{13}$$

The variables in Equation (13) are the same as in Equation (12), and Ξ_{op} is the optical deformation potential.

5.1.3. Other Scattering Mechanisms

For non-centrosymmetric crystals (e.g., BiTeI), the local strain can also induce a local electrical polarization field due to the piezoelectric effect. Other scattering mechanisms include intervalley scattering and scattering from intrinsic or extrinsic defects. Further details can be found elsewhere.[350]

5.1.4. Self-Trapping from Acoustic Phonons

So far, we have only discussed the deformability of the lattice and the coupling of optical phonons to it, which leads to Fröhlich coupling. Coupling of carriers to acoustic phonons can lead to distortions of the crystal lattice, which result in the formation of self-trapped carriers or self-trapped excitons. This can have large impact on the optoelectronic properties, which we will discuss later in Section 5.3. Here, we will first discuss the localization of carriers (electrons or holes, but not excitons) in a continuum model as introduced by Toyozawa.[353] In the continuum model, the discrete crystal structure is replaced by a continuum and we investigate how the acoustic deformation potential can lead to self-trapping.

Let us place an electron, with wavefunction $\boldsymbol{\Psi}$, inside a crystal lattice. This lattice will elastically deform by $\boldsymbol{\Delta}(\mathbf{r})$, with corresponding electrostatic potential $\boldsymbol{\phi}$ $(\mathbf{r})$. The corresponding change in energy due to this elastic deformation can be written as Equation (14).[353]

$$E(\nabla,\Psi,\phi) = \frac{\hbar}{2m}\int(\nabla\Psi)^2\,d\boldsymbol{r} + E_d\int|\Psi(\boldsymbol{r})|\Delta(\boldsymbol{r})\,d\boldsymbol{r} + e\int|\Psi(\boldsymbol{r})|^2 \phi(\boldsymbol{r})\,d\boldsymbol{r} + \frac{C}{2}\int[\Delta(\boldsymbol{r})]^2\,d\boldsymbol{r} + \frac{\varepsilon'}{8\pi}\int[\Delta\phi(\boldsymbol{r})]^2\,d\boldsymbol{r} \tag{14}$$

where C is the elastic constant, E_d is the acoustic deformation potential, and $\varepsilon^{-1} = (\varepsilon_\infty^{-1} - \varepsilon_0^{-1})$ is the difference of the dielectric constant at infinite and zero frequency.

The first term in Equation (14) is the kinetic energy of the electron. The second term is due to the coupling of the acoustic phonons with the electrons and its magnitude is determined by the acoustic deformation potential. Equivalently, the third term is the contribution due to electrons coupling to optical phonons via Fröhlich coupling. The fourth and fifth terms represent the elastic and dielectric polarization energies of the medium.

To understand whether the charges will localize, we take for the wavefunction of the electron a three dimensional Gaussian, as written in Equation (15).

$$\Psi(r) = \left(\sqrt{2}/a\right)^{3/2} \exp\left[-\pi\left(\frac{r}{a}\right)^2\right] \tag{15}$$

where a is a constant describing the radial extend of the wavefunction.

If the carrier is localized to a single unit cell the value for a becomes equal to the lattice constant, $a = a_0$. When the carrier is unbound the value for a tends to infinity, $a \to \infty$.

If we now minimize Equation (14) for both the elastic distortion Δ and the electrostatic potential ϕ using the wave function in Equation 15, we obtain Equations (16) and (17).

$$\Delta(\boldsymbol{r}) = (-E_d/C)\left|\Psi(\boldsymbol{r},a)\right|^2 \tag{16}$$

$$\nabla^2\phi(\boldsymbol{r}) = (4\pi e/\varepsilon')\left|\Psi(\boldsymbol{r},a)\right|^2 \tag{17}$$

Substituting Equations (16) and (17) into Equation (14) yields the following for a 3D system:

$$E[a] = \frac{3\pi\hbar^2}{2ma_0^2}\left(\frac{a_0}{a}\right)^2 - \frac{E_d^2}{2Ca_0^3}\left(\frac{a_0}{a}\right)^3 - \frac{e^2}{\varepsilon' a_0}\left(\frac{a_0}{a}\right) \tag{18}$$

$$E[\lambda] = B\left(\lambda^2 - g_{ac}\lambda^3 - g_{op}\lambda\right) \tag{19}$$

In Equation (19), $\lambda = (a_0/a)$ is the localization parameter and g_{ac}, g_{op} represent dimensionless electron–phonon coupling parameters. Following similar steps for 1D and 2D semiconductors yields,

$$\text{2D}: E[\lambda] = B\left(\lambda^2 - g_{ac}\lambda^2 - g_{op}\lambda\right) \tag{20}$$

$$\text{1D}: E[\lambda] = B\left(\lambda^2 - g_{ac}\lambda - g_{op}\lambda\right) \tag{21}$$

The coupling factor g_{op} is related to the Fröhlich coupling constant by

$$g_{op} = 2\left(\frac{\hbar\omega_{LO}}{3\pi B}\right)^{1/2}\alpha \tag{22}$$

The configurational coordinate diagram together with how the barrier to self-trapping depends on the dimensionality is depicted in Figure 36b.

Here, it is shown that the barrier to self-trapping depends on the dimensionality of the system. For 3D systems, there exists a barrier to self-trapping. This barrier height W is expressed by Equation (23).[354]

$$W \sim \frac{\omega^4}{\mu_{ex}^3\gamma^4} \tag{23}$$

where μ_{ex} is the reduced effective mass of the exciton, γ is the exciton–phonon coupling constant, and ω is the characteristic frequency of the optical phonons. This implies that the self-trapped carrier and free carriers can co-exist and that in photoluminescence experiments, the PL from both free and self-trapped excitons can be observed.[355] For 2D materials, there is no barrier to self-trapping due to acoustic phonons and whether self-trapping can occur depends on the coupling constant g_{ac}. For 1D materials, there is no barrier to self-trapping irrespective of the coupling to acoustic phonons.[356] High values of g_{ac} enable self-trapping due to acoustic phonons. Based on Equations (18) and (19), we see that high values of g_{ac} are obtained for high values of the acoustic deformation potential, E_d, and low values for the elastic constant C. That is, self-trapping is more readily observed in soft materials.

5.1.5. Self-Trapping due to Optical Phonons

The above discussion covered the impact of the acoustic deformation potential in pristine materials. Because optical phonons do not induce a macroscopic strain in the continuum model, they cannot cause carriers to localize. However optical phonons can induce microscopic distortions within the primitive cell,[350] which have been omitted in the continuum model. This microscopic distortion can still influence the electronic structure and cause non-radiative decay channels. More research is needed into how the excited state carriers interact with the optical phonons, how these excited carriers change the crystal structure, whether the carriers become localized or remain delocalized and how this influences the optoelectronic properties such as carrier lifetime and mobility.

5.1.6. Intrinsic versus Extrinsic Self-Trapping

When the acoustic deformation potential is sufficiently high, there will be a thermodynamic driving force causing carriers to self-trap in pristine materials, as discussed in the previous sections. However, real materials systems contain impurities and/or structural defects, which can also lead to the formation of extrinsic self-trapped excitons.[357,358] For example, in Ruddlesden–Popper hybrid lead-tin iodide perovskites, the tin on lead anti-site defect can capture holes, leading to a structural deformation where the bond length decreases. This leads to a broad Stokes shifted PL to appear alongside the free exciton emission, whereas in pristine Ruddlesden–Popper hybrid lead iodide perovskites, this PL feature is absent.[357] How intrinsic or extrinsic self-trapped could be identified is discussed later in Section 5.4.

5.1.7. Self-Trapped Carriers versus Self-Trapped Excitons

Depending on the optoelectronic properties of the material, either self-trapped holes, self-trapped electrons, or self-trapped excitons can be formed. For many semiconducting systems, the holes have higher effective masses than for the electrons causing the holes to preferentially self-trap over electrons (Tables 1 and 2).[356,359]

When a semiconductor absorbs a photon, it creates a free electron–hole pair. If there is a thermodynamic driving force to form a self-trapped exciton or self-trapped carrier, the carrier will localize within picoseconds.[360] When a self-trapped hole (electron) is formed, then the surrounding electron (hole) will be captured through coulombic attraction, depending on the exciton binding energy of the exciton. There can exist a trapping barrier for this capture leading to coexistence of free carriers with self-trapped carriers and self-trapped excitons.[357] Alternatively, rather than trapping a hole or an electron, it is also possible that the exciton is trapped without the intermediate state where only one of the carriers localizes. How these two cases can be distinguished will be discussed later in Section 5.4.

In the previous sections, we have discussed how reduced dimensionality can increase the effective mass and the exciton binding energy, both favoring the formation of self-trapped excitons rather than free carriers. In the next section, we will assess the impact of electron–phonon coupling on the optoelectronic properties of LHPs and PIMs.

5.2. Impact of Electron–Phonon Coupling on Optoelectronic Properties

5.2.1. Impact on Absorption

The coupling of the carriers to phonons can induce an absorption edge below the band gap of the semiconductor, called the Urbach edge, as given in Equation (24).[361]

$$\alpha(E) = \alpha_0 \ \exp\left(-\sigma \frac{E_0 - E}{kT}\right) \tag{24}$$

where α_0 is a constant and σ is the steepness parameter.

For a large range of different insulators and semiconductors, both organic and inorganic, a small value of σ is a strong indication of self-trapping of the carriers. There exists a reciprocal relationship between the steepness parameter and the acoustic coupling factor g_{ac}, as given by Equation (25).[359]

$$\sigma = s / g_{ac} \tag{25}$$

where s is a numerical constant which depends on the dimensionality of the system, the crystal structure, and for 1D systems also on temperature. When the value of g_{ac} in 2D or 3D materials exceeds a critical value of g_c (close to 1), the carriers are likely to become self-trapped.[353] In 1D materials, carriers will localize irrespective of its coupling strength to the acoustic phonons. Similarly, strong coupling to optical phonons will also induce small values for the steepness parameter σ.[361]

At temperatures above absolute zero, polar optical phonons give rise to additional exciton screening, which leads to an increased effective dielectric constant, lowering the exciton binding energy and therefore changing the (temperature dependent) absorption profile.[168]

5.2.2. Impact on Carrier Mobility

To study and determine the main limiting factors of charge-carrier mobilities in LHP, first-principle calculations have suggested that acoustic-phonon deformation potential scattering is weak for $MAPbI_3$ and should not result in decreases in charge-carrier mobilities.[100] For this reason, both theoretical and experimental studies agree that these acoustic-phonon deformations are not the limiting factor for charge-carrier mobilities at room temperature in $MAPbI_3$.[120,362–364] Instead, the presence of polar scattering mechanisms, in agreement with Fröhlich interactions at room temperature, can decrease the charge-carrier mobilities.[100,120,351] It is suggested that Fröhlich interactions are the dominant mechanism limiting charge-carrier mobility in $MAPbI_3$ at room temperature.[100] In particular, Fröhlich interactions were found to be higher for $MAPbBr_3$ with respect to $MAPbI_3$, and this was attributed to the higher ionicity of the Pb-Br bond compared to the Pb-I bond,[120] resulting in $MAPbBr_3$ having lower mobilities than $MAPbI_3$. Experimental and theoretical evidence suggests that the most important factor limiting charge-carrier mobilities are the Fröhlich interactions between charge carriers and the electric fields associated with the phonon modes of the ionic lattice.[9,120,351,365]

Beyond scattering mechanisms, carrier localization can further reduce the carrier mobility. As discussed in Section 5.1, the propensity to self-trap is dependent on the size of the deformation potentials, the Young's modulus, and the kinetic energy of the carriers, which are influenced by the dimensionality of the system, as well as other factors. Both electron and hole trapping have been observed to occur (e.g., in BiI_3 or HgI_2),[366,367] severely hindering the mobility of that particular carrier, but with the opposing carrier remaining free and still useful for various device applications.[359,368]

5.2.3. Impact on Photoluminescence Quantum Efficiency and Charge-Carrier Lifetime

Due to the scattering of the carriers, the PL peak broadens, with the temperature dependence of the full width half maximum (FWHM) of the PL peak dependent on the dominant scattering mechanism.[369] For semiconductors where the carriers or excitons are free and the PL comes from band to band or exciton recombination, the PL width is small and the electron-phonon coupling has little influence on the PLQE and lifetime of the carriers.

When carriers become localized and locally distort the lattice, the change the energy of the ground state. This is depicted in the configuration coordinate diagram for self-trapped carriers, which is shown in Figure 36b. When the carriers recombine radiatively, the PL becomes Stokes shifted with respect to the band gap or the excitonic absorption edge, because of the

increase in the ground state energy. Alternatively, the excited state carrier can couple directly to the ground state and emit its excess energy non-radiatively through a multi-phonon emission process.[370]

At room temperature, carrier localization can result in a non-radiative decay channel, which causes both the PLQE and charge-carrier lifetime to decrease.[371] The amount of non-radiative decay and quenching of the photoluminescence lifetime depends on the temperature and how well the self-trapped states couples into the ground state (or other states). The effect on the photoluminescence and absorption profile is depicted in Figure 38. Further, it has been shown that the formation of polarons can explain the low electron-hole recombination rates due to the increased spatial separation between the carriers, reducing the non-radiative recombination pathways and increasing the carrier lifetimes.[372,373] Finally, the high dielectric constant and polar characteristics of the LHPs and PIMs can effectively screen the charges, reducing the non-radiative capture cross-section, and therefore reduce the non-radiative recombination.[106]

The direct coupling of the excited carriers into the ground state can cause a fast non-radiative decay channel limiting the carrier lifetime at room temperature (see also Figure 36d). The effective carrier lifetime τ of the excited carriers can be written as:

$$\frac{1}{\tau}=\frac{1}{\tau_r}+\frac{1}{\tau_d}+\frac{1}{\tau_A}+\frac{1}{\tau_{\mathrm{STE}}}+\frac{1}{\tau_{\mathrm{other}}} \tag{26}$$

where τ_x is the contribution to the effective carrier lifetime and the subscripts *r, d, A,* STE, and other indicate the radiative, defect, Auger, self-trapped exciton, and other processes. The non-radiative recombination of self-trapped excited carriers by direct coupling into the ground state can become dominant and causes the effective carrier lifetime to become

$$\tau \approx \tau_{\mathrm{STE}} \tag{27}$$

The decay of the self-trapped excitons is a phonon mediated processes. By cooling down the semiconductor and depopulating the optical phonon modes, this decay channel can effectively be blocked, yielding carrier lifetimes which are order of magnitudes longer (increasing from ≈1 ns to beyond ≈10 µs).[371,374]

5.3. Impact of Electron–Phonon Coupling on Device Performance

5.3.1. Impact on Solar Cells and LEDs

Carrier-phonon coupling influences optoelectronic device performance in several ways, namely by: 1) reducing carrier mobilities, 2) increasing Urbach energies, 3) increasing or lowering PLQEs, and 4) reducing the effective exciton binding energy significantly because optical phonons give rise to dynamical screening of the electron–hole (e–h) Coulomb attraction.[375] In particular, the formation of self-trapped excitons can lead to a severe reduction in the carrier lifetime as discussed previously causing an unavoidable loss channel that will prevent the radiative limit from being achieved. So far, the PIMs found to be limited by strong electron–phonon coupling or the unavoidable formation of self-trapped excitons include $(C_6H_{11}NH_3)_2PbBr_4$,[374] $Cs_3Bi_2Br_9$,[376] $Cs_2AgBiBr_6$,[377] BiI_3,[279] and Sb_2S_3.[356]

Mobility: The reduction in mobility due to Fröhlich coupling limits the drift and diffusion lengths of the carriers. This can have influence on the performance of solar cells when this length is reduced to below the thickness of the active layer, leading to reductions in carrier extraction, and hence lower external quantum and power conversion efficiencies. More details discussing the impact of reduced mobility on the performance of optoelectronic devices can be found elsewhere.[100]

The coupling of carriers to acoustic phonons has receive limited attention thus far. For free carrier, the upper limit for charge-carrier mobilities restricted by coupling to optical phonons (which typically has values of several hundred $cm^2\ V^{-1}\ s^{-1}$) is typically lower than the mobilities restricted by coupling to acoustic phonons (which typically has values of several thousand $cm^2\ V^{-1}\ s^{-1}$).[351,378] However, in the case of self-trapping due to acoustic phonons, the carrier mobilities can be further reduced and become the limiting factor, posing intrinsic limitations for the application of the material for photovoltaics.[378]

Photoluminescence Quantum Efficiency: Another critical property which influences the device performance of LEDs and solar cells is the photoluminescence quantum efficiency. The strong confinement effects that are caused due to self-trapping can lead to either an enhancement or reduction in PLQE. In the case where excited carriers couple directly to the ground state and a non-radiative decay channel is introduced, the PLQE is greatly reduced. However, the carrier localization can also enhance the PLQE by enhancing radiative recombination rates, thus enabling white light LEDs.[379,380] This effect is similar to enhancing the scintillator effect in thallium (Tl) doped NaI, where now the Tl atoms act as radiation centers.[381]

Open-Circuit Voltage in Photovoltaics: To highlight the importance of carrier-phonon coupling on device performance, we calculated how self-trapping influences the open-circuit voltage in photovoltaics. As discussed previously, strong carrier-phonon coupling in self-trapped systems can lead to a large Urbach energy at room temperature, thus reducing the V_{oc} of the system. From Equation (25), we obtain that at room temperature the Urbach energy of self-trapped semiconductors is approximately above kT (25 meV) leading to a reduction in the maximum obtainable open-circuit voltage of up to several hundred meV. This reduction of the V_{oc} with respect to the radiative limit (under similar assumptions) as a function of the Urbach energy is depicted in **Figure 37**. Details of the calculations can be found in ref. [382] and [16].

Second, many PIMs have large exciton binding energies (as discussed in Section 4). In efficient organic solar cells, the high exciton binding energy is overcome by a ≈300 meV offset in molecular orbital energy levels between the donor and acceptor, leading to a reduction in achievable open circuit voltage.[383] In order to dissociate the electron–hole pair into free carriers in PIMs, an additional built-in voltage would be required to extract the charge carriers, further reducing the V_{oc}.

Third, in an ideal system at the radiative limit and at open-circuit voltage all the recombination is radiative. However, in real systems, non-radiative recombination occurs due to defects. As discussed previously, self-trapped excitons can add to the non-radiative recombination rate and can lead to very low

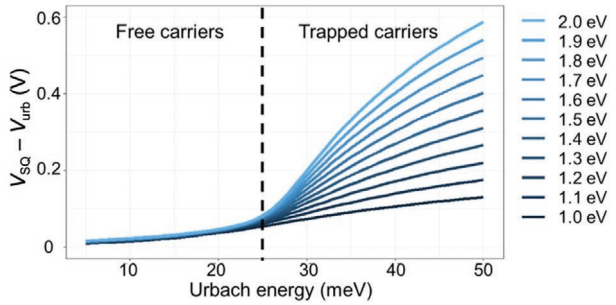

Figure 37. Calculated loss in radiative limit of the open circuit voltage due to the exponential absorption tail caused by carrier localization plotted for different band gaps. The calculations shown here are based on the description detailed in ref. [338] and [16].

electroluminescence quantum efficiencies ($EQE_{EL} << 10^{-3}$) in self-trapped systems.[377] The additional loss due to low EQE_{EL} at open circuit can be expressed by Equation (28).

$$V_{oc,loss} = \frac{kT}{q} \ln\left(\frac{1}{EQE_{EL}}\right) \tag{28}$$

For an EQE_{EL} between 10^{-3} and 10^{-7} (typical for low PLQE materials),[377] this leads to an additional voltage loss of between 175 and 409 meV.

Finally, at open circuit, there is no internal field to drive the drift of carriers toward the charge selective contacts. To extract all the photo-generated charges, the carriers/excitons need to diffuse through the absorber layer. As discussed previously, the diffusion length can be reduced due to carrier localization. This can increase the non-radiative recombination due to the limited lifetime, further reducing the open-circuit voltage.

The low EQE_{EL}, high Urbach energy, high exciton binding energy, and limited diffusion length of trapped carriers/excitons can explain the large voltage losses (from 100 meV up to >1 V) typically seen in PIMs and other emerging photovoltaic materials (Table 2), and identifying the occurrence of self-trapping is of paramount importance to access the potential of new material classes.[234] Note that under an applied electric field, the charges can still be sufficiently mobile yielding highly sensitive radiation detectors.[368]

5.4. How to Identify Self-Trapped Systems

Given the large implications of self-trapping on the optoelectronic properties and device performance, it is of great importance to identify experimentally whether carriers in the semi-conductor undergo self-trapping. There are several experimental characterization methods that can be used to identify this. Here, we will broadly discuss experimental approaches to do this, but it is noted that the exact results are highly materials class dependent.

One of the simplest ways to identify self-trapping is by measuring the steady-state and time-resolved absorption and photoluminescence properties of the semiconductor at various temperatures. Typically for self-trapped systems, the PL is broadened and Stokes shifted with respect to the absorption edge. From this, the Huang-Rhys factor can be determined, with high values for the Huang-Rhys factor indicating self-trapping.[384] For semiconductors with low PLQE at room temperature, it is important to measure the shape of the PL at low temperature. At reduced temperatures, the optical phonons are no longer populated, and thus the non-radiative decay channel is blocked, which leads to increased carrier lifetimes and PLQEs (see also **Figure 38**b).[253,371] Additionally, due to the strong coupling of the lattice to the carriers, the photoluminescence observed from single crystals can be polarized in the direction of the dimensionality of the system.[356] See Figure 38a for an example of how this has been measured in Sb_2S_3 single crystals, which have a quasi-1D crystal structure.

Beyond changes in the photoluminescence, there is also an impact on the absorption profile. Typically, self-trapped systems are excitonic and therefore absorption features due to excitons are present. We note, however, that the absence of excitonic absorption features is not proof that a system is not self-trapped, since the excitons may be dark due to it being associated with an indirect band gap or a direct transition that is parity forbidden. For direct band gap semiconductors, the excitonic free absorption features are sharp, while for indirect semiconductors these are broadened and difficult to identify.

Further the self-trapped carriers induce a photon induced absorption in the absorption spectrum, which can be measured by transient absorption.[385] By measuring the fluence dependence of carrier trapping, it can be determined whether one of the carriers localizes and then captures the other carrier or whether the exciton is captured as a single entity.[356] Additionally, the temperature-dependent Urbach energy can be measured, from which it is possible to determine the steepness parameter, as discussed earlier.[386] A steepness parameter below 1 indicates free carriers, whereas a value above 1 indicates trapped carriers.[353] Finally, by measuring the change of the absorption edge with the aid of a magnetic field, it is possible to determine the degree of localization.[387]

Self-trapping of carriers can further be determined from transport measurements, specifically by measuring the (temperature dependent) mobility of both carriers separately. There are various techniques available to measure the carrier mobilities.[100]

Finally, care needs to be taken to distinguish between self-trapping due to intrinsic and extrinsic origins. Impurity defects can also cause the excitons to become self-trapped, as for example has been shown in Ruddlesden–Popper hybrid lead iodide perovskites.[357] One way the extrinsic origin of this defect can be visualized is by mapping the spatial homogeneity of the PL (see also Figure 38c).[358] Here, the different intensity ratio of the two PL peaks at different parts of the crystal highlight the extrinsic origin of the PL.

Further to experimental characterization, computational measures are suitable to guide interpretation of data if it is suggesting carrier localization.[357] From first-principles density-functional-theory, the structural distortion caused by localized excited carriers can be determined, further strengthening the photophysical processes governing self-trapping.[357,360,380]

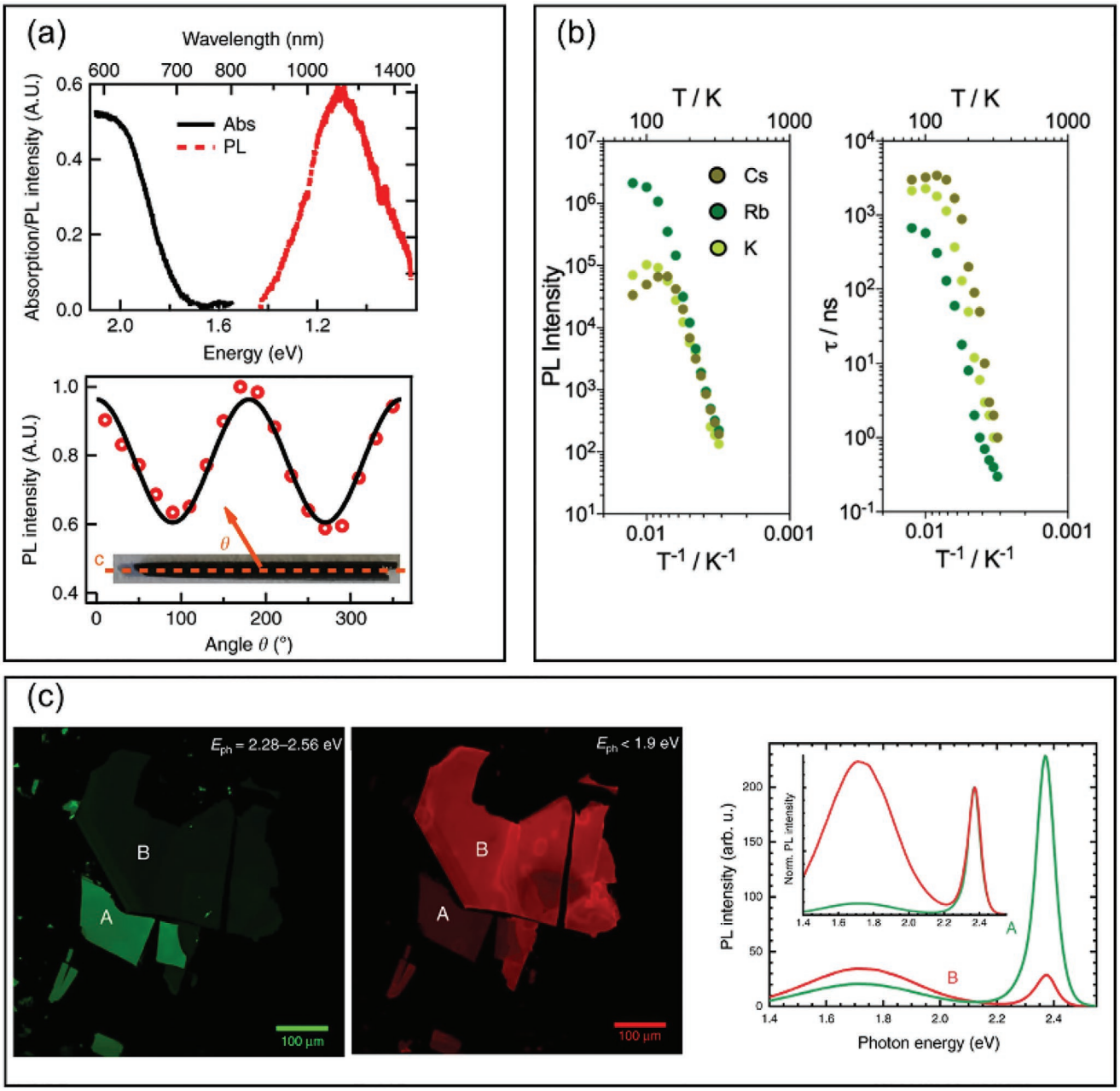

Figure 38. a) PL intensity from a Sb_2S_3 single crystal as a function of polarization detection angle (θ) and fitting with $\cos(2\theta)$. θ is defined to be 0 when detection polarization is along the crystal c-axis direction. Inset: Optical image of a needle-like Sb_2S_3 single crystal. Reproduced under the terms of the CC-BY license.[356] Copyright 2019, Springer Nature. b) Luminescence properties of $A_3Sb_2I_9$ thin films. The extracted photoluminescence counts (integrated from the time-resolved photoluminescence) as a function of temperature together with the extracted constant decay of the long-tail photoluminescence as a function of temperature for $Cs_3Sb_2I_9$, $Rb_3Sb_2I_9$, and $K_3Sb_2I_9$. Reproduced with permission.[253] Copyright 2018, American Chemical Society. c) Confocal PL maps of 3-fluorophenylethylammonium iodide, $FPEA_2PbI_4$, single crystals. The green (photon energy E_{ph} of 2.28–2.56 eV) and red (smaller than 1.9 eV) channel shows complementary intensity maps with bright green areas in point A appearing especially dim in the left and middle figure. The corresponding representative spectra for points A and B indicate the spatial inhomogeneity in the observed PL from the crystals. Reproduced under the terms of the CC-BY license.[358] Copyright 2020, Springer Nature.

6. Conclusions and Outlook

Perovskites are a highly versatile and very well studied family of materials exhibiting a wide range of properties, including the photovoltaic effect, ferroelectric effect, piezoelectric effect, and superconductivity. The structural and electronic dimensionality can be tuned from 3D down to 0D (including perovskite-derivative phases), through tuning the composition. Furthermore, the form factor can be tuned from 3D bulk thin films to 2D nanoplatelets and 2D electron gases, 1D nanowires, and 0D quantum dots. This tunability in dimensionality and form factor open up the ability to control the stability, band gap,

exciton binding energy, mobility, and defect tolerance, which is critical for the optimal performance of photovoltaics and light-emitting diodes.

Although inorganic oxide perovskites are the classical perovskites since their first discovery as a mineral in nature, they have only recently demonstrated promise for photovoltaics, with 8.1% power conversion efficiency achieved in the double perovskite Bi_2FeCrO_6. Owing to the multiferroic nature of oxide perovskites, there is the opportunity to explore novel concepts, such as the ferroelectric photovoltaic effect, which can enable open-circuit voltages exceeding the band gap. However, the mechanisms behind this effect are not completely understood and the efficiencies of ferroelectric photovoltaics are currently low due to low short-circuit current densities and fill factors. In general, oxide perovskites have wide band gaps, and it is critical to identify and develop materials with band gaps small enough for single-junction (1.34 eV) or top-cell (1.72 eV) applications. This has been achieved through doping and alloying, as well as by exploring polymorphs, such as the layered Brownmillerites. Another critical challenge is that oxide perovskites have high melting points, and it is necessary to process the materials at high temperatures >600 °C in order to achieve sufficiently low defect densities. There is potential to overcome these limitations in chalcogenide perovskites, since sulfides tend to have lower melting points than oxides and this would imply that high homologous temperatures can be achieved at lower processing temperatures. However, there are currently scant reports of chalcogenide perovskites for photovoltaics, although several materials have band gaps that are promising for solar absorbers (e.g., $BaZrS_3$ with a direct band gap of 1.73 eV).

Halide perovskites demonstrate complementary advantages and disadvantages to the oxide perovskites. While oxide perovskites suffer from high processing temperatures and generally wide band gaps, halide perovskites are typically processed at only 100 °C, and lead-iodide-based perovskites have suitable band gaps close to 1.6 eV for outdoor light harvesting. On the other hand, while oxide perovskites are stable, halide perovskites demonstrate limited thermal and environmental stability. Tuning the dimensionality of halide perovskites has been instrumental in addressing this, with the long organic ligands of Ruddlesden–Popper and Dion–Jacobson phases (derived from the perovskite structure) acting as barriers against moisture ingress or as passivating agents, enabling photovoltaics stable for 1000 h, and up to 10 000 h. Furthermore, Dion–Jacobson perovskites have shown to be more robust than Ruddlesden–Popper perovskites due to the double hydrogen bonding of their divalent cation to the inorganic lattice. Lowering the dimensionality of halide perovskites by forming 2D, quasi-2D phases, or nanocrystals leads to increased exciton binding energy, which has been critical in enabling improved LED performance, but the disadvantages of reduced dimensionality are wider band gaps and reduced band dispersion, leading to lower mobilities. In photovoltaics, this has been overcome through multi-dimensional perovskites, in which a bulk 3D perovskite (low band gap, high mobility) is covered with a surface layer of a 2D perovskite to improve stability and passivate surface defects. Multi-dimensional perovskites have also been advantageous for LED applications, in which perovskites with dimensionality ranging from 3D to 2D are mixed together into one thin film. Injected carriers are then funneled to the 3D perovskite phase (which has the lowest band gap), where the electrons and holes are strongly confined, leading to higher EQEs.

Dimensionality has also been a critical consideration in lead-free perovskite-inspired materials. The most commonly explored materials are tin- and germanium-based perovskites, vacancy-ordered triple ($A_3B(III)_2X_9$) and double ($A_2B(IV)X_6$) perovskites, as well as lead-free halide double perovskites ($A_2B(I)B(III)X_6$). Among these, mixed tin-germanium perovskites have demonstrated the highest power conversion efficiencies, and these materials are structurally and electronically 3D. While double perovskites are also structurally 3D, their electronic dimensionality is often lower owing to the orbitals introduced by the B-site cations (e.g., Ag and Bi). It is the electronic dimensionality rather than the structural dimensionality that more directly affects the band gap, mobility, and exciton binding energy. This can be seen in $A_2B(IV)X_6$ perovskites (e.g., Cs_2SnI_6), which are structurally 0D but have higher electronic dimensionality owing to the close-packed halide sub-lattice. Although the $A_3B(III)_2X_9$ vacancy-ordered triple perovskites initially considered ($MA_3Bi_2I_9$ and $Cs_3Bi_2I_9$) were electronically and structurally 0D (or at least quasi-0D),[274] recent efforts have uncovered approaches to increase the dimensionality to 2D by using small A-site cations (e.g., NH_4) or alloying Br or Cl into the X-site. These 2D polymorphs exhibit lower exciton binding energies and band gaps; however, the efficiencies achieved in photovoltaic devices have yet to match the Sn- or Pb-based perovskites.

The perovskite-inspired materials explored so far have gone beyond perovskites to materials that could replicate the defect tolerance of the lead-halide perovskites, and these include $Sb_2(S,Se)_3$ and BiOI. Recent work has shown dimensionality to play an important role on defect tolerance, particularly the bond length and anion coordination. These effects complement the original design rules for defect tolerance based on chemical descriptors. Furthermore, lower electronic dimensionality that leads to higher effective masses will result in larger Sommerfeld factors, which in turn result in larger capture cross-sections for charged defects. As is the case with the oxide perovskites, searching for materials with low melting points is an important goal for minimizing defect densities in PIMs processed at practical temperatures.[87]

Beyond the role of defects, the effects of carrier–phonon and exciton–phonon coupling need to be accounted for. This becomes especially important in lead-halide perovskites, as well as in PIMs, which are based on heavy metal elements. In soft materials (low elastic constant) with heavy elements, the resonant frequency of dominant phonons modes is lower, leading to larger Fröhlich coupling to optical phonons and a higher propensity to self-trapping of carriers. Furthermore, the barrier for self-trapping is dependent on the dimensionality of the crystal structure. Self-trapped excitons or carriers can act as an extra loss channel significantly reducing the carrier lifetimes and increasing the Urbach energy, which results in further reductions in the open-circuit voltage of solar cells, as well as broader emission in LEDs. On the other hand, emission from self-trapped excitons has recently been demonstrated for white-light

phosphors. Promisingly, the lead-free double perovskite white-light phosphors demonstrated were shown to be stable in air.[360]

Overall, the oxide and halide perovskite fields, as well as the PIMs field, offer a rich plethora of future opportunities for materials development that will enable photovoltaic and LED devices that are more efficient with improved stability, but it is clear that future efforts will need to pay particular attention to the electronic dimensionality of the materials developed. Further insights into the structural and chemical factors influencing trap energy and the capture cross-sections should also be developed in order to more accurately design defect-tolerant materials. It is also important that more attention is given into the effects of carrier/exciton coupling to phonons, which can fundamentally limit charge transport as well as the efficiency potential (especially if self-trapped excitons are formed). The insights into the role of dimensionality on the optoelectronic properties discussed in this review can guide these future efforts to discover, develop, and optimize perovskites and PIMs for solar cells and LEDs.

Acknowledgements

R.L.Z.H. acknowledges support from the Royal Academy of Engineering under the Research Fellowship scheme (No.: RF\201718\1701), the Isaac Newton Trust (Minute 19.07(d)), and Downing College Cambridge through the Kim and Juliana Silverman Research Fellowship. T.F. would like to thank the CNRS through its energy program (Cellule Energie). J.H. and J.-P.C.-B. would like to thank the Graduate Assistance in Areas of National Need (GAANN) fellowship for financial support. R.A.J. would like to acknowledge the support from a DTP studentship funded by the EPSRC (no. EP/N509620/1). R.A.J. and J.L.M.-D. would like to thank Bill Welland for financial support. J.L.M.-D. also thanks the Royal Academy of Engineering Chair in Emerging technologies grant (no. CIET1819_24), and the EPSRC Centre of Advanced Materials for Integrated Energy Systems (CAM-IES), grant no. EP/P007767/1 for financial support.

Conflict of Interest

The authors declare no conflict of interest.

Author Contributions

R.L.Z.H. led in writing the abstract, introduction, Section 4 on perovskite-inspired materials, Table 2, and Section 6 on conclusions and outlook. He also made contributions to Sections 3 and 5. J.H. led in writing Section 3 and Table 1, supervised by J.-P.C.-B. R.A.J. led in writing Section 5. T.F. and J.L.M.-D. wrote Section 2. All authors discussed and edited the review as a whole.

Keywords

defects, electronic dimensionality, light-emitting diodes, perovskite-inspired materials, perovskites, photovoltaics, structural dimensionality

Received: February 10, 2021
Revised: March 22, 2021
Published online: May 5, 2021

[1] A. K. Jena, A. Kulkarni, T. Miyasaka, *Chem. Rev.* **2019**, *119*, 3036.
[2] A. R. Chakhmouradian, P. M. Woodward, *Phys. Chem. Miner.* **2014**, *41*, 387.
[3] W. J. Yin, B. Weng, J. Ge, Q. Sun, Z. Li, Y. Yan, *Energy Environ. Sci.* **2019**, *12*, 442.
[4] J. Breternitz, S. Schorr, *Adv. Energy Mater.* **2018**, *8*, 1802366.
[5] H. J. Snaith, *Nat. Mater.* **2018**, *17*, 372.
[6] R. Nechache, C. Harnagea, S. Li, L. Cardenas, W. Huang, J. Chakrabartty, F. Rosei, *Nat. Photonics* **2014**, *9*, 61.
[7] *Nat. Energy* **2019**, *4*, 1.
[8] A. Kojima, K. Teshima, Y. Shirai, T. Miyasaka, *J. Am. Chem. Soc.* **2009**, *131*, 6050.
[9] NREL, Best Research-Cell Efficiency Chart **2020**, https://www.nrel.gov/pv/cell-efficiency.html.
[10] J. J. Yoo, S. Wieghold, M. C. Sponseller, M. R. Chua, S. N. Bertram, T. Putri, J. S. Tresback, *Energy Environ. Sci.* **2019**, *12*, 2192.
[11] A. Polman, M. Knight, E. C. Garnett, B. Ehrler, W. C. Sinke, *Science* **2016**, *352*, aad4424.
[12] G. E. Eperon, T. Leijtens, K. A. Bush, R. Prasanna, T. Green, J. T.-W. Wang, D. P. McMeekin, G. Volonakis, R. L. Milot, R. May, A. Palmstrom, D. J. Slotcavage, R. A. Belisle, J. B. Patel, E. S. Parrott, R. J. Sutton, W. Ma, F. Moghadam, B. Conings, A. Babayigit, H.-G. Boyen, S. Bent, F. Giustino, L. M. Herz, M. B. Johnston, M. D. McGehee, H. J. Snaith, *Science* **2016**, *354*, 861.
[13] P. P. Boix, S. Agarwala, T. M. Koh, N. Mathews, S. G. Mhaisalkar, *J. Phys. Chem. Lett.* **2015**, *6*, 898.
[14] S. D. Stranks, G. E. Eperon, G. Grancini, C. Menelaou, M. J. P. Alcocer, T. Leijtens, L. M. Herz, A. Petrozza, H. J. Snaith, *Science* **2013**, *342*, 341.
[15] R. E. Brandt, J. R. Poindexter, P. Gorai, R. C. Kurchin, R. L. Z. Hoye, L. Nienhaus, M. W. B. Wilson, J. A. Polizzotti, R. Sereika, R. Žaltauskas, L. C. Lee, J. L. MacManus-Driscoll, M. Bawendi, V. Stevanović, T. Buonassisi, *Chem. Mater.* **2017**, *29*, 4667.
[16] P. K. Nayak, S. Mahesh, H. J. Snaith, D. Cahen, *Nat. Rev. Mater.* **2019**, *4*, 269.
[17] S. D. Stranks, R. L. Z. Hoye, D. Di, R. H. Friend, F. Deschler, *Adv. Mater.* **2019**, *31*, 1803336.
[18] F. Igbari, Z. K. Wang, L. S. Liao, *Adv. Energy Mater.* **2019**, *9*, 1803150.
[19] I. Grinberg, D. V. West, M. Torres, G. Gou, D. M. Stein, L. Wu, G. Chen, E. M. Gallo, A. R. Akbashev, P. K. Davies, J. E. Spanier, A. M. Rappe, *Nature* **2013**, *503*, 509.
[20] S. Y. Yang, J. Seidel, S. J. Byrnes, P. Shafer, C. H. Yang, M. D. Rossell, P. Yu, Y. H. Chu, J. F. Scott, J. W. Ager, L. W. Martin, R. Ramesh, *Nat. Nanotechnol.* **2010**, *5*, 143.
[21] *Photovoltaics Report*, Freiburg, **2018**.
[22] R. Fu, D. Feldman, R. Margolis, M. Woodhouse, K. Ardani, *US Solar Photovoltaic System Cost Benchmark: Q1 2017*, Golden, CO **2017**.
[23] Z. Li, Y. Zhao, X. Wang, Y. Sun, Z. Zhao, Y. Li, H. Zhou, Q. Chen, *Joule* **2018**, *2*, 1559.
[24] R. Lin, K. Xiao, Z. Qin, Q. Han, C. Zhang, M. Wei, M. I. Saidaminov, Y. Gao, J. Xu, M. Xiao, A. Li, J. Zhu, E. H. Sargent, H. Tan, *Nat. Energy* **2019**, *4*, 864.
[25] V. Andrei, B. Reuillard, E. Reisner, *Nat. Mater.* **2020**, *19*, 189.
[26] V. Andrei, R. L. Z. Hoye, M. Crespo-Quesada, M. Bajada, S. Ahmad, M. De Volder, R. Friend, E. Reisner, *Adv. Energy Mater.* **2018**, *8*, 1801403.
[27] W. Li, K. Jiang, Z. Li, S. Gong, R. L. Z. Hoye, Z. Hu, Y. Song, C. Tian, J. Kim, K. H. L. Zhang, S. Cho, J. L. MacManus-Driscoll, *Adv. Energy Mater.* **2018**, *8*, 1801972.
[28] L. Dou, Y. M. Yang, J. You, Z. Hong, W. H. Chang, G. Li, Y. Yang, *Nat. Commun.* **2014**, *5*, 5404.
[29] J. Li, J. Wang, J. Ma, H. Shen, L. Li, X. Duan, D. Li, *Nat. Commun.* **2019**, *10*, 806.
[30] H. Wei, J. Huang, *Nat. Commun.* **2019**, *10*, 1066.

[31] N. Moody, S. Sesena, W. Dane, B. D. Dou, R. Swartwout, J. T. Buchman, A. Johnson, U. Eze, R. Brenes, M. Johnston, C. L. Haynes, N. Moody, S. Sesena, B. D. Dou, A. Johnson, R. Brenes, V. Bulovi, J. T. Buchman, L. Christy, *Joule* **2020**, *4*, 970.
[32] A. M. Ganose, C. N. Savory, D. O. Scanlon, *Chem. Commun.* **2017**, *53*, 20.
[33] L. C. Lee, T. N. Huq, J. L. MacManus-Driscoll, R. L. Z. Hoye, *APL Mater.* **2018**, *6*, 084502.
[34] A. H. Slavney, T. Hu, A. M. Lindenberg, H. I. Karunadasa, *J. Am. Chem. Soc.* **2016**, *138*, 2138.
[35] Z. Li, S. Kavanagh, M. Napari, R. G. Palgrave, M. Abdi-Jalebi, Z. Andaji-Garmaroudi, D. W. Davies, M. Laitinen, J. Julin, M. A. Isaacs, R. H. Friend, D. O. Scanlon, A. Walsh, R. L. Z. Hoye, *J. Mater. Chem. A* **2020**, *8*, 21780.
[36] R. L. Z. Hoye, M.-L. Lai, M. Anaya, Y. Tong, K. Galkowski, T. Doherty, W. Li, T. N. Huq, S. Mackowski, L. Polavarapu, J. Feldmann, J. L. MacManus-Driscoll, R. H. Friend, A. S. Urban, S. D. Stranks, *ACS Energy Lett.* **2019**, *4*, 1181.
[37] R. Sarmiento-Pérez, T. F. T. Cerqueira, S. Körbel, S. Botti, M. A. L. Marques, *Chem. Mater.* **2015**, *27*, 5957.
[38] G. Zhang, G. Liu, L. Wang, J. T. S. Irvine, *Chem. Soc. Rev.* **2016**, *45*, 5951.
[39] T. Minami, Y. Nishi, T. Miyata, *Appl. Phys. Express* **2016**, *9*, 052301.
[40] T. Fix, in *Advanced Micro- and Nanomaterials for Photovoltaics* (Eds: D. Ginley, T. Fix), Elsevier, New York **2019**, pp. 19–34.
[41] A. Pérez-Tomás, A. Mingorance, D. Tanenbaum, M. Lira-Cantú, in The *Future of Semiconductor Oxides in Next-Generation Solar Cells* (Ed: M. Lira-Cantú), Elsevier, New York **2018**, pp. 267–356.
[42] U. Rau, J. H. Werner, *Appl. Phys. Lett.* **2004**, *84*, 3735.
[43] T. Todorov, O. Gunawan, S. Guha, *Mol. Syst. Des. Eng.* **2016**, *1*, 370.
[44] A. B. Murphy, P. R. F. Barnes, L. K. Randeniya, I. C. Plumb, I. E. Grey, M. D. Horne, J. A. Glasscock, *Int. J. Hydrogen Energy* **2006**, *31*, 1999.
[45] C. W. Zhao, B. C. Luo, S. J. Guo, C. L. Chen, *Ceram. Int.* **2017**, *43*, 7861.
[46] A. Bera, K. Wu, A. Sheikh, E. Alarousu, O. F. Mohammed, T. Wu, *J. Phys. Chem. C* **2014**, *118*, 28494.
[47] M. Neophytou, M. De Bastiani, N. Gasparini, E. Aydin, E. Ugur, A. Seitkhan, F. Moruzzi, Y. Choaie, A. J. Ramadan, J. R. Troughton, R. Hallani, A. Savva, L. Tsetseris, S. Inal, D. Baran, F. Laquai, T. D. Anthopoulos, H. J. Snaith, S. De Wolf, I. McCulloch, *ACS Appl. Energy Mater.* **2019**, *2*, 8090.
[48] S. S. Shin, E. J. Yeom, W. S. Yang, S. Hur, M. G. Kim, J. Im, J. Seo, J. H. Noh, S. Il Seok, *Science* **2017**, *356*, 167.
[49] M. Nakamura, A. Sawa, J. Fujioka, M. Kawasaki, Y. Tokura, *Phys. Rev. B* **2010**, *82*, 4.
[50] N. N. Kovaleva, A. V. Boris, P. Yordanov, A. Maljuk, E. Brücher, J. Strempfer, M. Konuma, I. Zegkinoglou, C. Bernhard, A. M. Stoneham, B. Keimer, *Phys. Rev. B* **2007**, *76*, 155125.
[51] A. A. Tsvetkov, F. P. Mena, P. H. M. Van Loosdrecht, D. Van der Marel, Y. Ren, A. A. Nugroho, A. A. Menovsky, I. S. Elfimov, G. A. Sawatzky, *Phys. Rev. B* **2004**, *69*, 075110.
[52] M. Jellite, J. L. Rehspringer, M. A. Fazio, D. Muller, G. Schmerber, G. Ferblantier, S. Colis, A. Dinia, M. Sugiyama, A. Slaoui, D. Cavalcoli, T. Fix, *Sol. Energy* **2018**, *162*, 1.
[53] M. Imada, A. Fujimori, Y. Tokura, *Rev. Mod. Phys.* **1998**, *70*, 1039.
[54] S. W. Bae, P. H. Borse, J. S. Lee, *Appl. Phys. Lett.* **2008**, *92*, 104107.
[55] A. G. Chynoweth, *Phys. Rev.* **1956**, *102*, 705.
[56] M. M. Seyfouri, D. Wang, *Crit. Rev. Solid State Mater. Sci.* **2020**, *46*, 83.
[57] J. Chakrabartty, C. Harnagea, M. Celikin, F. Rosei, R. Nechache, *Nat. Photonics* **2018**, *12*, 271.
[58] J. Chakrabartty, D. Barba, L. Jin, D. Benetti, F. Rosei, R. Nechache, *J. Power Sources* **2017**, *365*, 162.
[59] Y. Yang, Z. Liu, W. K. Ng, L. Zhang, H. Zhang, X. Meng, Y. Bai, S. Xiao, T. Zhang, C. Hu, K. S. Wong, S. Yang, *Adv. Funct. Mater.* **2019**, *29*, 1806506.
[60] L. Theofylaktos, K. O. Kosmatos, E. Giannakaki, H. Kourti, D. Deligiannis, M. Konstantakou, T. Stergiopoulos, *Dalton Trans.* **2019**, *48*, 9516.
[61] A. Quattropani, D. Stoeffler, T. Fix, G. Schmerber, M. Lenertz, G. Versini, J. L. Rehspringer, A. Slaoui, A. Dinia, S. Colis, *J. Phys. Chem. C* **2018**, *122*, 1070.
[62] G. Gou, N. Charles, J. Shi, J. M. Rondinelli, *Inorg. Chem.* **2017**, *56*, 11854.
[63] A. S. Thind, S. Kavadiya, M. Kouhnavard, R. Wheelus, S. B. Cho, L. Y. Lin, C. Kacica, H. K. Mulmudi, K. A. Unocic, A. Y. Borisevich, G. Pilania, P. Biswas, R. Mishra, *Chem. Mater.* **2019**, *31*, 4769.
[64] M. Sariful Sheikh, D. Ghosh, A. Dutta, S. Bhattacharyya, T. P. Sinha, *Mater. Sci. Eng. B Solid-State Mater. Adv. Technol.* **2017**, *226*, 10.
[65] G. Zhang, H. Wu, G. Li, Q. Huang, C. Yang, F. Huang, F. Liao, J. Lin, *Sci. Rep.* **2013**, *3*, 1265.
[66] T. Fix, G. Schmerber, H. Wang, J. L. Rehspringer, C. Leuvrey, S. Roques, M. Lenertz, D. Muller, H. Wang, A. Slaoui, *ACS Appl. Energy Mater.* **2019**, *2*, 8039.
[67] V. Thangadurai, W. Weppner, *Ionics (Kiel)* **2006**, *12*, 81.
[68] Y. Chen, Y. Sun, J. Peng, J. Tang, K. Zheng, Z. Liang, *Adv. Mater.* **2018**, *30*, 1703487.
[69] B. Y. Alfaifi, A. A. Tahir, K. G. U. Wijayantha, *Sol. Energy Mater. Sol. Cells* **2019**, *195*, 134.
[70] J. Bai, Y. Li, X. Li, L. Liu, *New J. Chem.* **2017**, *41*, 7783.
[71] H. G. Kim, D. W. Hwang, J. S. Lee, *J. Am. Chem. Soc.* **2004**, *126*, 8912.
[72] B. Prijamboedi, S. Umar, F. Failamani, *AIP Conf. Proc* **2015**, *1656*, 10.
[73] Z. Liang, K. Tang, Q. Shao, G. Li, S. Zeng, H. Zheng, *J. Solid State Chem.* **2008**, *181*, 964.
[74] F. Meng, Z. Hong, J. Arndt, M. Li, M. Zhi, F. Yang, N. Wu, *Nano Res.* **2012**, *5*, 213.
[75] A. Ohtomo, D. A. Muller, J. L. Grazul, H. Y. Hwang, *Nature* **2002**, *419*, 378.
[76] T. Fix, F. Schoofs, J. L. MacManus-Driscoll, M. G. Blamire, *Phys. Rev. Lett.* **2009**, *103*, 166802.
[77] E. Assmann, P. Blaha, R. Laskowski, K. Held, S. Okamoto, G. Sangiovanni, *Phys. Rev. Lett.* **2013**, *110*, 078701.
[78] D. Ji, S. Cai, T. R. Paudel, H. Sun, C. Zhang, L. Han, Y. Wei, Y. Zang, M. Gu, Y. Zhang, W. Gao, H. Huyan, W. Guo, D. Wu, Z. Gu, E. Y. Tsymbal, P. Wang, Y. Nie, X. Pan, *Nature* **2019**, *570*, 87.
[79] D. Lu, D. J. Baek, S. S. Hong, L. F. Kourkoutis, Y. Hikita, H. Y. Hwang, *Nat. Mater.* **2016**, *15*, 1255.
[80] B. Zhang, C. Yun, J. L. MacManus-Driscoll, *Nano-Micro Lett.* **2021**, *13*, 39.
[81] T. Yang, T. T. Song, M. Callsen, J. Zhou, J. W. Chai, Y. P. Feng, S. J. Wang, M. Yang, *Adv. Mater. Interfaces* **2019**, *6*, 1801160.
[82] F. Polo-Garzon, Z. Bao, X. Zhang, W. Huang, Z. Wu, *ACS Catal.* **2019**, *9*, 5692.
[83] L. Li, L. Liang, H. Wu, X. Zhu, *Nanoscale Res. Lett.* **2016**, *11*, 121.
[84] S. Datta, S. Chandra, S. Samanta, K. Das, H. Srikanth, B. Ghosh, *J. Nanomater.* **2013**, *2013*, 162315.
[85] B. D. Yuhas, P. Yang, *J. Am. Chem. Soc.* **2009**, *131*, 3756.
[86] K. P. Musselman, A. Wisnet, D. C. Iza, H. C. Hesse, C. Scheu, J. L. MacManus-Driscoll, L. Schmidt-Mende, *Adv. Mater.* **2010**, *22*, E254.
[87] J. L. MacManus-Driscoll, M. P. Wells, C. Yun, J. W. Lee, C. B. Eom, D. G. Schlom, *APL Mater.* **2020**, *8*, 040904.
[88] Z. Grzesik, K. Przybylski, in *Developments in High Temperature Corrosion and Protection of Materials* (Eds: W. Gao, Z. Li), Woodhead Publishing, Sawston, UK **2008**, pp. 599–638.
[89] H. Hahn, U. Mutschke, *Z. Anorg. Allg. Chem.* **1957**, *288*, 269.
[90] S. Perera, H. Hui, C. Zhao, H. Xue, F. Sun, C. Deng, N. Gross, C. Milleville, X. Xu, D. F. Watson, B. Weinstein, Y. Y. Sun, S. Zhang, H. Zeng, *Nano Energy* **2016**, *22*, 129.

[91] Q. Sun, H. Chen, W. J. Yin, *Chem. Mater.* **2019**, *31*, 244.
[92] C. Comparotto, A. Davydova, T. Ericson, L. Riekehr, M. V. Moro, T. Kubart, J. Scragg, *ACS Appl. Energy Mater.* **2020**, *3*, 2762.
[93] X. Wei, H. Hui, C. Zhao, C. Deng, M. Han, Z. Yu, A. Sheng, P. Roy, A. Chen, J. Lin, D. F. Watson, Y. Y. Sun, T. Thomay, S. Yang, Q. Jia, S. Zhang, H. Zeng, *Nano Energy* **2020**, *68*, 104317.
[94] A. Crovetto, R. Nielsen, M. Pandey, L. Watts, J. G. Labram, M. Geisler, N. Stenger, K. W. Jacobsen, O. Hansen, B. Seger, I. Chorkendorff, P. C. K. Vesborg, *Chem. Mater.* **2019**, *31*, 3359.
[95] S. Niu, H. Huyan, Y. Liu, M. Yeung, K. Ye, L. Blankemeier, T. Orvis, D. Sarkar, D. J. Singh, R. Kapadia, J. Ravichandran, *Adv. Mater.* **2017**, *29*, 1604733.
[96] Y. Wang, N. Sato, T. Fujino, *J. Alloys Compd.* **2001**, *327*, 104.
[97] Y. Y. Sun, M. L. Agiorgousis, P. Zhang, S. Zhang, *Nano Lett.* **2015**, *15*, 581.
[98] S. Niu, D. Sarkar, K. Williams, Y. Zhou, Y. Li, E. Bianco, H. Huyan, S. B. Cronin, M. E. McConney, R. Haiges, R. Jaramillo, D. J. Singh, W. A. Tisdale, R. Kapadia, J. Ravichandran, *Chem. Mater.* **2018**, *30*, 4882.
[99] J. Du, J. Shi, *Adv. Mater.* **2019**, *31*, 1905643.
[100] L. M. Herz, *ACS Energy Lett.* **2017**, *2*, 1539.
[101] C. Wehrenfennig, M. Liu, H. J. Snaith, M. B. Johnston, L. M. Herz, *J. Phys. Chem. Lett.* **2014**, *5*, 1300.
[102] S. de Wolf, J. Holovsky, S.-J. Moon, P. Löper, B. Niesen, M. Ledinsky, F. Haug, J. Yum, C. Ballif, *J. Phys. Chem. Lett.* **2014**, *5*, 1035.
[103] L. Etgar, *Energy Environ. Sci.* **2018**, *11*, 234.
[104] G. Xing, N. Mathews, S. S. Lim, Y. M. Lam, S. Mhaisalkar, T. C. Sum, *Science* **2013**, *342*, 344.
[105] W.-J. Yin, T. Shi, Y. Yan, *Appl. Phys. Lett.* **2014**, *104*, 063903.
[106] R. E. Brandt, V. Stevanovic, D. S. Ginley, T. Buonassisi, *MRS Commun.* **2015**, *5*, 265.
[107] E. M. Tennyson, T. A. S. Doherty, S. D. Stranks, *Nat. Rev. Mater.* **2019**, *4*, 573.
[108] G. W. Kim, A. Petrozza, *Adv. Energy Mater.* **2020**, *10*, 2001959.
[109] W. A. Dunlap-Shohl, Y. Zhou, N. P. Padture, D. B. Mitzi, *Chem. Rev.* **2019**, *119*, 3193.
[110] Q. A. Akkerman, G. Rainò, M. V. Kovalenko, L. Manna, *Nat. Mater.* **2018**, *17*, 394.
[111] Z. Xiao, W. Meng, J. Wang, D. B. Mitzi, Y. Yan, *Mater. Horiz.* **2017**, *4*, 206.
[112] J. P. Correa-Baena, M. Saliba, T. Buonassisi, M. Grätzel, A. Abate, W. Tress, A. Hagfeldt, *Science* **2017**, *358*, 739.
[113] O. A. Syzgantseva, M. Saliba, M. Grätzel, U. Rothlisberger, *J. Phys. Chem. Lett.* **2017**, *8*, 1191.
[114] Z. Li, M. Yang, J. Park, S. Wei, J. J. Berry, K. Zhu, *Chem. Mater.* **2016**, *28*, 284.
[115] K. A. Bush, A. F. Palmstrom, Z. J. Yu, M. Boccard, R. Cheacharoen, J. P. Mailoa, D. P. McMeekin, R. L. Z. Hoye, C. D. Bailie, T. Leijtens, I. M. Peters, M. C. Minichetti, N. Rolston, R. Prasanna, S. Sofia, D. Harwood, W. Ma, F. Moghadam, H. J. Snaith, T. Buonassisi, Z. C. Holman, S. F. Bent, M. D. McGehee, *Nat. Energy* **2017**, *2*, 17009.
[116] K. O. Brinkmann, J. Zhao, N. Pourdavoud, T. Becker, T. Hu, S. Olthof, K. Meerholz, L. Hoffmann, T. Gahlmann, R. Heiderhoff, M. F. Oszajca, N. A. Luechinger, D. Rogalla, Y. Chen, B. Cheng, T. Riedl, *Nat. Commun.* **2017**, *8*, 13938.
[117] J. Zhao, K. O. Brinkmann, T. Hu, N. Pourdavoud, T. Becker, T. Gahlmann, R. Heiderhoff, A. Polywka, P. Görrn, Y. Chen, B. Cheng, T. Riedl, *Adv. Energy Mater.* **2017**, *7*, 1602599.
[118] K. P. Ong, S. Wu, T. H. Nguyen, D. J. Singh, Z. Fan, M. B. Sullivan, C. Dang, *Sci. Rep.* **2019**, *9*, 2144.
[119] X. G. Zhao, G. M. Dalpian, Z. Wang, A. Zunger, *Phys. Rev. B* **2020**, *101*, 155137.
[120] A. D. Wright, C. Verdi, R. L. Milot, G. E. Eperon, M. A. Pérez-Osorio, H. J. Snaith, F. Giustino, M. B. Johnston, L. M. Herz, *Nat. Commun.* **2016**, *7*, 1038.
[121] E. Menéndez-Proupin, P. Palacios, P. Wahnón, J. C. Conesa, *Phys. Rev. B* **2014**, *90*, 045207.
[122] G. Giorgi, J. I. Fujisawa, H. Segawa, K. Yamashita, *J. Phys. Chem. Lett.* **2013**, *4*, 4213.
[123] P. Umari, E. Mosconi, F. De Angelis, *Sci. Rep.* **2015**, *4*, 4467.
[124] C. Motta, F. El-Mellouhi, S. Sanvito, *Sci. Rep.* **2015**, *5*, 12746.
[125] M. Hirasawa, T. Ishihara, T. Goto, K. Uchida, N. Miura, *Phys. B* **1994**, *201*, 427.
[126] A. Miyata, A. Mitioglu, P. Plochocka, O. Portugall, J. T. W. Wang, S. D. Stranks, H. J. Snaith, R. J. Nicholas, *Nat. Phys.* **2015**, *11*, 582.
[127] K. Galkowski, A. Mitioglu, A. Miyata, P. Plochocka, O. Portugall, G. E. Eperon, J. T. W. Wang, T. Stergiopoulos, S. D. Stranks, H. J. Snaith, R. J. Nicholas, *Energy Environ. Sci.* **2016**, *9*, 962.
[128] A. Amat, E. Mosconi, E. Ronca, C. Quarti, P. Umari, M. K. Nazeeruddin, M. Grätzel, F. De Angelis, *Nano Lett.* **2014**, *14*, 3608.
[129] J. Cho, J. T. Dubose, P. V. Kamat, *J. Phys. Chem. Lett.* **2020**, *11*, 2570.
[130] D. Burkitt, R. Patidar, P. Greenwood, K. Hooper, J. McGettrick, S. Dimitrov, M. Colombo, V. Stoichkov, D. Richards, D. Beynon, M. Davies, T. Watson, *Sustainable Energy Fuels* **2020**, *4*, 3340.
[131] Y. Deng, C. H. van Brackle, X. Dai, J. Zhao, B. Chen, J. Huang, *Sci. Adv.* **2019**, *5*, eaax7537.
[132] P. Schulz, D. Cahen, A. Kahn, *Chem. Rev.* **2019**, *119*, 3349.
[133] F. Zhang, H. Lu, J. Tong, J. J. Berry, M. C. Beard, K. Zhu, *Energy Environ. Sci.* **2020**, *13*, 1154.
[134] I. H. Park, Q. Zhang, K. C. Kwon, Z. Zhu, W. Yu, K. Leng, D. Giovanni, H. S. Choi, I. Abdelwahab, Q. H. Xu, T. C. Sum, K. P. Loh, *J. Am. Chem. Soc.* **2019**, *141*, 15972.
[135] P. Huang, S. Kazim, M. Wang, S. Ahmad, *ACS Energy Lett.* **2019**, *4*, 2960.
[136] L. Mao, W. Ke, L. Pedesseau, Y. Wu, C. Katan, J. Even, M. R. Wasielewski, C. C. Stoumpos, M. G. Kanatzidis, *J. Am. Chem. Soc.* **2018**, *140*, 3775.
[137] D. Ghosh, D. Acharya, L. Pedesseau, C. Katan, J. Even, S. Tretiak, A. J. Neukirch, *J. Mater. Chem. A* **2020**, *8*, 22009.
[138] C. C. Stoumpos, D. H. Cao, D. J. Clark, J. Young, J. M. Rondinelli, J. I. Jang, J. T. Hupp, M. G. Kanatzidis, *Chem. Mater.* **2016**, *28*, 2852.
[139] M. H. Tremblay, J. Bacsa, B. Zhao, F. Pulvirenti, S. Barlow, S. R. Marder, *Chem. Mater.* **2019**, *31*, 6145.
[140] H. Tsai, W. Nie, J.-C. Blancon, C. C. Stoumpos, R. Asadpour, B. Harutyunyan, A. J. Neukirch, R. Verduzco, J. J. Crochet, S. Tretiak, L. Pedesseau, J. Even, M. A. Alam, G. Gupta, J. Lou, P. M. Ajayan, M. J. Bedzyk, M. G. Kanatzidis, A. D. Mohite, *Nature* **2016**, *536*, 312.
[141] A. Z. Chen, M. Shiu, J. H. Ma, M. R. Alpert, D. Zhang, B. J. Foley, D. M. Smilgies, S. H. Lee, J. J. Choi, *Nat. Commun.* **2018**, *9*, 1336.
[142] M. C. Gélvez-Rueda, M. B. Fridriksson, R. K. Dubey, W. F. Jager, W. van der Stam, F. C. Grozema, *Nat. Commun.* **2020**, *11*, 1901.
[143] I. C. Smith, E. T. Hoke, D. Solis-Ibarra, M. D. McGehee, H. I. Karunadasa, *Angew. Chem., Int. Ed.* **2014**, *53*, 11232; , *Angew. Chem.* **2014**, *126*, 11414.
[144] J.-F. Liao, H.-S. Rao, B.-X. Chen, D.-B. Kuang, C.-Y. Su, *J. Mater. Chem. A* **2017**, *5*, 2066.
[145] D. S. Lee, J. S. Yun, J. Kim, A. M. Soufiani, S. Chen, Y. Cho, X. Deng, J. Seidel, S. Lim, S. Huang, A. W. Y. Ho-Baillie, *ACS Energy Lett.* **2018**, *3*, 647.
[146] M. D. Smith, B. A. Connor, H. I. Karunadasa, *Chem. Rev.* **2019**, *119*, 3104.
[147] Y. Shang, Y. Liao, Q. Wei, Z. Wang, B. Xiang, Y. Ke, W. Liu, Z. Ning, *Sci. Adv.* **2019**, *5*, eaaw8072.
[148] D. Marongiu, M. Saba, F. Quochi, A. Mura, G. Bongiovanni, *J. Mater. Chem. C* **2019**, *7*, 12006.

[149] M. Baranowski, P. Plochocka, *Adv. Energy Mater.* **2020**, *10*, 1903659.
[150] B. A. Gregg, *J. Phys. Chem. B* **2003**, *107*, 4688.
[151] E. M. Conwell, *Synth. Met.* **1996**, *83*, 101.
[152] J. C. Hebig, I. Kühn, J. Flohre, T. Kirchartz, *ACS Energy Lett.* **2016**, *1*, 309.
[153] B. Saparov, D. B. Mitzi, *Chem. Rev.* **2016**, *116*, 4558.
[154] Z. Yang, A. Surrente, K. Galkowski, N. Bruyant, D. K. Maude, A. A. Haghighirad, H. J. Snaith, P. Plochocka, R. J. Nicholas, *J. Phys. Chem. Lett.* **2017**, *8*, 1851.
[155] J. Li, J. Ma, X. Cheng, Z. Liu, Y. Chen, D. Li, *ACS Nano* **2020**, *14*, 2156.
[156] J. Zhang, X. Zhu, M. Wang, B. Hu, *Nat. Commun.* **2020**, *11*, 2618.
[157] H. Xu, M. Wang, Z. G. Yu, K. Wang, B. Hu, *Adv. Phys.* **2019**, *68*, 49.
[158] K. Tanaka, T. Kondo, *Sci. Technol. Adv. Mater.* **2003**, *4*, 599.
[159] D. B. Straus, C. R. Kagan, *J. Phys. Chem. Lett.* **2018**, *9*, 1434.
[160] X.-F. He, *Phys. Rev. B* **1991**, *43*, 2063.
[161] J. T. Lin, C. C. Liao, C. S. Hsu, D. G. Chen, H. M. Chen, M. K. Tsai, P. T. Chou, C. W. Chiu, *J. Am. Chem. Soc.* **2019**, *141*, 10324.
[162] H. Esmaielpour, V. R. Whiteside, S. Sourabh, G. E. Eperon, J. T. Precht, M. C. Beard, H. Lu, B. K. Durant, I. R. Sellers, *J. Phys. Chem. C* **2020**, *124*, 9496.
[163] S. Maheshwari, T. J. Savenije, N. Renaud, F. C. Grozema, *J. Phys. Chem. C* **2018**, *122*, 17118.
[164] T. Ishihara, X. Hong, J. Ding, A. V. Nurmikko, *Surf. Sci.* **1992**, *267*, 323.
[165] E. A. Muljarov, S. G. Tikhodeev, N. A. Gippius, *Phys. Rev. B* **1995**, *51*, 14370.
[166] J. C. Blancon, A. V. Stier, H. Tsai, W. Nie, C. C. Stoumpos, B. Traoré, L. Pedesseau, M. Kepenekian, F. Katsutani, G. T. Noe, J. Kono, S. Tretiak, S. A. Crooker, C. Katan, M. G. Kanatzidis, J. J. Crochet, J. Even, A. D. Mohite, *Nat. Commun.* **2018**, *9*, 2254.
[167] M. C. Gélvez-Rueda, E. M. Hutter, D. H. Cao, N. Renaud, C. C. Stoumpos, J. T. Hupp, T. J. Savenije, M. G. Kanatzidis, F. C. Grozema, *J. Phys. Chem. C* **2017**, *121*, 26566.
[168] L. Pedesseau, D. Sapori, B. Traore, R. Robles, H. H. Fang, M. A. Loi, H. Tsai, W. Nie, J. C. Blancon, A. Neukirch, S. Tretiak, A. D. Mohite, C. Katan, J. Even, M. Kepenekian, *ACS Nano* **2016**, *10*, 9776.
[169] V. M. Agranovich, Y. N. Gartstein, M. Litinskaya, *Chem. Rev.* **2011**, *111*, 5179.
[170] P. Chen, Y. Bai, M. Lyu, J. H. Yun, M. Hao, L. Wang, *Sol. RRL* **2018**, *2*, 1700186.
[171] P. Gao, A. R. Bin Mohd Yusoff, M. K. Nazeeruddin, *Nat. Commun.* **2018**, *9*, 5028.
[172] Y. Li, J. V. Milić, A. Ummadisingu, J. Y. Seo, J. H. Im, H. S. Kim, Y. Liu, M. I. Dar, S. M. Zakeeruddin, P. Wang, A. Hagfeldt, M. Grätzel, *Nano Lett.* **2019**, *19*, 150.
[173] D. B. Mitzi, S. Wang, C. A. Feild, C. A. Chess, A. M. Guloy, *Science* **1995**, *267*, 1473.
[174] G. Grancini, M. K. Nazeeruddin, *Nat. Rev. Mater.* **2019**, *4*, 4.
[175] S. Ahmad, P. Fu, S. Yu, Q. Yang, X. Liu, X. Wang, X. Wang, X. Guo, C. Li, *Joule* **2019**, *3*, 794.
[176] Z. Wang, Q. Lin, F. P. Chmiel, N. Sakai, L. M. Herz, H. J. Snaith, *Nat. Energy* **2017**, *2*, 17135.
[177] G. Grancini, C. Roldán-Carmona, I. Zimmermann, E. Mosconi, X. Lee, D. Martineau, S. Narbey, F. Oswald, F. De Angelis, M. Graetzel, M. K. Nazeeruddin, *Nat. Commun.* **2017**, *8*, 15684.
[178] C. Ma, C. Leng, Y. Ji, X. Wei, K. Sun, L. Tang, J. Yang, W. Luo, C. Li, Y. Deng, S. Feng, J. Shen, S. Lu, C. Du, H. Shi, *Nanoscale* **2016**, *8*, 18309.
[179] Q. Jiang, Y. Zhao, X. Zhang, X. Yang, Y. Chen, Z. Chu, Q. Ye, X. Li, Z. Yin, J. You, *Nat. Photonics* **2019**, *13*, 460.
[180] H. Zhu, Y. Liu, F. T. Eickemeyer, L. Pan, D. Ren, M. A. Ruiz-Preciado, B. Carlsen, B. Yang, X. Dong, Z. Wang, H. Liu, S. Wang, S. M. Zakeeruddin, A. Hagfeldt, M. I. Dar, X. Li, M. Grätzel, *Adv. Mater.* **2020**, *32*, 1907757.
[181] W. Feng, C. Zhang, J. X. Zhong, L. Ding, W. Q. Wu, *Chem. Commun.* **2020**, *56*, 5006.
[182] Z. Yuan, C. Zhou, Y. Tian, Y. Shu, J. Messier, J. C. Wang, L. J. Van De Burgt, K. Kountouriotis, Y. Xin, E. Holt, K. Schanze, R. Clark, T. Siegrist, B. Ma, *Nat. Commun.* **2017**, *8*, 14051.
[183] C. Sun, Y. Di Yue, W. F. Zhang, X. Y. Sun, Y. Du, H. M. Pan, Y. Y. Ma, Y. C. He, M. T. Li, Z. H. Jing, *CrystEngComm* **2020**, *22*, 1480.
[184] T. Qiu, Y. Hu, F. Xu, Z. Yan, F. Bai, G. Jia, S. Zhang, *Nanoscale* **2018**, *10*, 20963.
[185] U. Thumu, M. Piotrowski, B. Owens-Baird, Y. V. Kolen'ko, *J. Solid State Chem.* **2019**, *271*, 361.
[186] Y. Zhang, M. I. Saidaminov, I. Dursun, H. Yang, B. Murali, E. Alarousu, E. Yengel, B. A. Alshankiti, O. M. Bakr, O. F. Mohammed, *J. Phys. Chem. Lett.* **2017**, *8*, 961.
[187] S. Elleuch, A. Lusson, S. Pillet, K. Boukheddaden, Y. Abid, *ACS Photonics* **2020**, *7*, 1178.
[188] M. I. Saidaminov, J. Almutlaq, S. Sarmah, I. Dursun, A. A. Zhumekenov, R. Begum, J. Pan, N. Cho, O. F. Mohammed, O. M. Bakr, *ACS Energy Lett.* **2016**, *1*, 840.
[189] G. C. Papavassiliou, G. Pagona, N. Karousis, G. A. Mousdis, I. Koutselas, A. Vassilakopoulou, *J. Mater. Chem.* **2012**, *22*, 8271.
[190] L. Protesescu, S. Yakunin, M. I. Bodnarchuk, F. Krieg, R. Caputo, C. H. Hendon, R. X. Yang, A. Walsh, M. V. Kovalenko, *Nano Lett.* **2015**, *15*, 3692.
[191] J. Shamsi, A. S. Urban, M. Imran, L. De Trizio, L. Manna, *Chem. Rev.* **2019**, *119*, 3296.
[192] J. Ye, M. M. Byranvand, C. O. Martínez, R. L. Z. Hoye, M. Saliba, L. Polavarapu, *Angew. Chem., Int. Ed.* **2021**, https://doi.org/10.1002/anie.202102360; , *Angew. Chem.* **2021**, https://doi.org/10.1002/ange.202102360.
[193] B. J. Bohn, Y. Tong, M. Gramlich, M. L. Lai, M. Döblinger, K. Wang, R. L. Z. Hoye, P. Muller-Buschbaum, S. D. Stranks, A. S. Urban, L. Polavarapu, J. Feldmann, *Nano Lett.* **2018**, *18*, 5231.
[194] J. Gan, J. He, R. L. Z. Hoye, A. Mavlonov, F. Raziq, J. L. MacManus-Driscoll, X. Wu, S. Li, X. Zu, Y. Zhan, X. Zhang, L. Qiao, *ACS Energy Lett.* **2019**, *4*, 1308.
[195] M. C. Weidman, A. J. Goodman, W. A. Tisdale, *Chem. Mater.* **2017**, *29*, 5019.
[196] L. C. Schmidt, A. Pertegás, S. González-Carrero, O. Malinkiewicz, S. Agouram, G. Mínguez Espallargas, H. J. Bolink, R. E. Galian, J. Pérez-Prieto, *J. Am. Chem. Soc.* **2014**, *136*, 850.
[197] H. Huang, J. Raith, S. V. Kershaw, S. Kalytchuk, O. Tomanec, L. Jing, A. S. Susha, R. Zboril, A. L. Rogach, *Nat. Commun.* **2017**, *8*, 996.
[198] Y. Wu, X. Li, H. Zeng, *ACS Energy Lett.* **2019**, *4*, 673.
[199] S. Kumar, J. Jagielski, T. Marcato, S. F. Solari, C. J. Shih, *J. Phys. Chem. Lett.* **2019**, *10*, 7560.
[200] B. Yang, F. Hong, J. Chen, Y. Tang, L. Yang, Y. Sang, X. Xia, J. Guo, H. He, S. Yang, W. Deng, K. Han, *Angew. Chem., Int. Ed.* **2019**, *58*, 2278; , *Angew. Chem.* **2019**, *131*, 2300.
[201] M. J. Jurow, T. Morgenstern, C. Eisler, J. Kang, E. Penzo, M. Do, M. Engelmayer, W. T. Osowiecki, Y. Bekenstein, C. Tassone, L. W. Wang, A. P. Alivisatos, W. Brütting, Y. Liu, *Nano Lett.* **2019**, *19*, 2489.
[202] A. Pan, B. He, X. Fan, Z. Liu, J. J. Urban, A. P. Alivisatos, L. He, Y. Liu, *ACS Nano* **2016**, *10*, 7943.
[203] M. Imran, V. Caligiuri, M. Wang, L. Goldoni, M. Prato, R. Krahne, L. De Trizio, L. Manna, *J. Am. Chem. Soc.* **2018**, *140*, 2656.
[204] M. Imran, F. Di Stasio, Z. Dang, C. Canale, A. H. Khan, J. Shamsi, R. Brescia, M. Prato, L. Manna, *Chem. Mater.* **2016**, *28*, 6450.
[205] D. Zhang, S. W. Eaton, Y. Yu, L. Dou, P. Yang, *J. Am. Chem. Soc.* **2015**, *137*, 9230.
[206] Y. Wu, C. Wei, X. Li, Y. Li, S. Qiu, W. Shen, B. Cai, Z. Sun, D. Yang, Z. Deng, H. Zeng, *ACS Energy Lett.* **2018**, *3*, 2030.

[207] E. T. Hoke, D. J. Slotcavage, E. R. Dohner, A. R. Bowring, H. I. Karunadasa, M. D. McGehee, *Chem. Sci.* **2015**, *6*, 613.
[208] D. P. Nenon, K. Pressler, J. Kang, B. A. Koscher, J. H. Olshansky, W. T. Osowiecki, M. A. Koc, L. W. Wang, A. P. Alivisatos, *J. Am. Chem. Soc.* **2018**, *140*, 17760.
[209] Y. Tong, E. Bladt, M. F. Aygüler, A. Manzi, K. Z. Milowska, V. A. Hintermayr, P. Docampo, S. Bals, A. S. Urban, L. Polavarapu, J. Feldmann, *Angew. Chem., Int. Ed.* **2016**, *55*, 13887; , *Angew. Chem.* **2016**, *128*, 14091.
[210] E. P. Yao, Z. Yang, L. Meng, P. Sun, S. Dong, Y. Yang, Y. Yang, *Adv. Mater.* **2017**, *29*, 1606859.
[211] M. K. Gangishetty, S. Hou, Q. Quan, D. N. Congreve, *Adv. Mater.* **2018**, *30*, 1706226.
[212] P. Zhu, S. Gu, X. Shen, N. Xu, Y. Tan, S. Zhuang, Y. Deng, Z. Lu, Z. Wang, J. Zhu, *Nano Lett.* **2016**, *16*, 871.
[213] J. H. Park, A. Y. Lee, J. C. Yu, Y. S. Nam, Y. Choi, J. Park, M. H. Song, *ACS Appl. Mater. Interfaces* **2019**, *11*, 8428.
[214] Y. Ye, W. Zhang, Z. Zhao, J. Wang, C. Liu, Z. Deng, X. Zhao, J. Han, *Adv. Opt. Mater.* **2019**, *7*, 1801663.
[215] C. Bi, S. Wang, Q. Li, S. V. Kershaw, J. Tian, A. L. Rogach, *J. Phys. Chem. Lett.* **2019**, *10*, 943.
[216] Y. Dong, Y. K. Wang, F. Yuan, A. Johnston, Y. Liu, D. Ma, M. J. Choi, B. Chen, M. Chekini, S. W. Baek, L. K. Sagar, J. Fan, Y. Hou, M. Wu, S. Lee, B. Sun, S. Hoogland, R. Quintero-Bermudez, H. Ebe, P. Todorovic, F. Dinic, P. Li, H. T. Kung, M. I. Saidaminov, E. Kumacheva, E. Spiecker, L. S. Liao, O. Voznyy, Z. H. Lu, E. H. Sargent, *Nat. Nanotechnol.* **2020**, *15*, 668.
[217] L. M. Wheeler, E. M. Sanehira, A. R. Marshall, P. Schulz, M. Suri, N. C. Anderson, J. A. Christians, D. Nordlund, D. Sokaras, T. Kroll, S. P. Harvey, J. J. Berry, L. Y. Lin, J. M. Luther, *J. Am. Chem. Soc.* **2018**, *140*, 10504.
[218] A. Swarnkar, A. R. Marshall, E. M. Sanehira, B. D. Chernomordik, D. T. Moore, J. A. Christians, T. Chakrabarti, J. M. Luther, *Science* **2016**, *354*, 92.
[219] E. M. Sanehira, A. R. Marshall, J. A. Christians, S. P. Harvey, P. N. Ciesielski, L. M. Wheeler, P. Schulz, L. Y. Lin, M. C. Beard, J. M. Luther, *Sci. Adv.* **2017**, *3*, eaao4204.
[220] H. Yoshimura, M. Yamauchi, S. Masuo, *J. Phys. Chem. Lett.* **2020**, *11*, 530.
[221] H. Utzat, W. Sun, A. E. K. Kaplan, F. Krieg, M. Ginterseder, B. Spokoyny, N. D. Klein, K. E. Shulenberger1, C. F. Perkinson, M. V. Kovalenko, M. G. Bawendi, *Science* **2019**, *363*, 1068.
[222] Q. Zhao, A. Hazarika, L. T. Schelhas, J. Liu, E. A. Gaulding, G. Li, M. Zhang, M. F. Toney, P. C. Sercel, J. M. Luther, *ACS Energy Lett.* **2020**, *5*, 238.
[223] J. Chen, D. Jia, E. M. J. Johansson, A. Hagfeldt, X. Zhang, *Energy Environ. Sci.* **2021**, *14*, 224.
[224] S. S. Mali, C. S. Shim, C. K. Hong, *NPG Asia Mater* **2015**, *7*, e208.
[225] M. Hao, Y. Bai, S. Zeiske, L. Ren, J. Liu, Y. Yuan, N. Zarrabi, N. Cheng, M. Ghasemi, P. Chen, M. Lyu, D. He, J.-H. Yun, Y. Du, Y. Wang, S. Ding, A. Armin, P. Meredith, G. Liu, H.-M. Cheng, L. Wang, *Nat. Energy* **2020**, *5*, 79.
[226] J. Yuan, A. Hazarika, Q. Zhao, X. Ling, T. Moot, W. Ma, J. M. Luther, *Joule* **2020**, *4*, 1160.
[227] Y. Wei, Z. Cheng, J. Lin, *Chem. Soc. Rev.* **2018**, *48*, 310.
[228] Y. Bekenstein, B. A. Koscher, S. W. Eaton, P. Yang, A. P. Alivisatos, *J. Am. Chem. Soc.* **2015**, *137*, 16008.
[229] M. J. Jurow, T. Lampe, E. Penzo, J. Kang, M. A. Koc, T. Zechel, Z. Nett, M. Brady, L. W. Wang, A. P. Alivisatos, S. Cabrini, W. Brütting, Y. Liu, *Nano Lett.* **2017**, *17*, 4534.
[230] J. Cui, Y. Liu, Y. Deng, C. Lin, Z. Fang, C. Xiang, P. Bai, K. Du, X. Zuo, K. Wen, S. Gong, H. He, Z. Ye, Y. Gao, H. Tian, B. Zhao, J. Wang, Y. Jin, (Preprint) arXiv: 2006.07611v1, submitted Jun **2020**.
[231] D. Meggiolaro, S. G. Motti, E. Mosconi, A. J. Barker, J. Ball, C. Andrea Riccardo Perini, F. Deschler, A. Petrozza, F. De Angelis, *Energy Environ. Sci.* **2018**, *11*, 702.
[232] R. Nie, R. R. Sumukam, S. H. Reddy, M. Banavoth, S. Il Seok, *Energy Environ. Sci.* **2020**, *13*, 2363.
[233] W. Ke, M. G. Kanatzidis, *Nat. Commun.* **2019**, *10*, 965.
[234] Y.-T. Huang, S. R. Kavanagh, D. O. Scanlon, A. Walsh, R. L. Z. Hoye, *Nanotechnology* **2021**, *32*, 132004.
[235] N. Glück, T. Bein, *Energy Environ. Sci.* **2020**, *13*, 4691.
[236] A. E. Maughan, A. M. Ganose, D. O. Scanlon, J. R. Neilson, *Chem. Mater.* **2019**, *31*, 1184.
[237] Health and Safety Executive, *EH40 /2005 Workplace Exposure Limits Limits for Use with the Control of Substances (Fourth Edition 2020)*, TSO, Norwich, UK **2020**, https://www.hse.gov.uk/pubns/books/eh40.htm (accessed: February 2021).
[238] Health and Safety Executive, Control of lead at work (Third edition) **2002**, https://www.hse.gov.uk/pubns/priced/l132.pdf (accessed: February 2021).
[239] W. J. Yin, T. Shi, Y. Yan, *Adv. Mater.* **2014**, *26*, 4653.
[240] C. C. Stoumpos, L. Frazer, D. J. Clark, Y. S. Kim, S. H. Rhim, A. J. Freeman, J. B. Ketterson, J. I. Jang, M. G. Kanatzidis, *J. Am. Chem. Soc.* **2015**, *137*, 6804.
[241] Z. Wang, A. M. Ganose, C. Niu, D. O. Scanlon, *J. Mater. Chem. A* **2018**, *6*, 5652.
[242] B. Saparov, F. Hong, J. P. Sun, H. S. Duan, W. Meng, S. Cameron, I. G. Hill, Y. Yan, D. B. Mitzi, *Chem. Mater.* **2015**, *27*, 5622.
[243] L. Ma, M. G. Ju, J. Dai, X. C. Zeng, *Nanoscale* **2018**, *10*, 11314.
[244] K. M. McCall, C. C. Stoumpos, O. Y. Kontsevoi, G. C. B. Alexander, B. W. Wessels, M. G. Kanatzidis, *Chem. Mater.* **2019**, *31*, 2644.
[245] R. Hoye, R. E. Brandt, A. Osherov, V. Stevanović, S. D. Stranks, M. W. B. Wilson, H. Kim, A. J. Akey, J. D. Perkins, R. C. Kurchin, J. R. Poindexter, E. N. Wang, M. G. Bawendi, V. Bulović, T. Buonassisi, *Chem. A Eur. J.* **2015**, *22*, 2605.
[246] X. Zheng, W. Zhao, P. Wang, H. Tan, M. I. Saidaminov, S. Tie, L. Chen, Y. Peng, J. Long, W. H. Zhang, *J. Energy Chem.* **2020**, *49*, 299.
[247] W. G. Li, X. D. Wang, J. F. Liao, Y. Jiang, D. Bin Kuang, *Adv. Funct. Mater.* **2020**, *30*, 1909701.
[248] K. Eckhardt, V. Bon, J. Getzschmann, J. Grothe, F. M. Wisser, S. Kaskel, *Chem. Commun.* **2016**, *52*, 3058.
[249] N. Giesbrecht, A. Weis, T. Bein, *J. Phys. Energy* **2020**, *2*, 024007.
[250] R. Zhuang, X. Wang, W. Ma, Y. Wu, X. Chen, L. Tang, H. Zhu, J. Liu, L. Wu, W. Zhou, X. Liu, Y. (M.) Yang, *Nat. Photonics* **2019**, *13*, 602.
[251] A. J. Lehner, D. H. Fabini, H. A. Evans, C. A. Hébert, S. R. Smock, J. Hu, H. Wang, J. W. Zwanziger, M. L. Chabinyc, R. Seshadri, *Chem. Mater.* **2015**, *27*, 7137.
[252] C. Zuo, L. Ding, *Angew. Chemie Int. Ed.* **2017**, *56*, 6528.
[253] J. P. Correa-Baena, L. Nienhaus, R. C. Kurchin, S. S. Shin, S. Wieghold, N. T. P. Hartono, M. Layurova, N. D. Klein, J. R. Poindexter, A. Polizzotti, S. Sun, M. G. Bawendi, T. Buonassisi, *Chem. Mater.* **2018**, *30*, 3734.
[254] N. G. Park, *Mater. Today* **2015**, *18*, 65.
[255] V. Sidey, *Acta Crystallogr. Sect. B: Struct. Sci. Cryst. Eng. Mater.* **2016**, *72*, 626.
[256] T. L. Hodgkins, C. N. Savory, K. K. Bass, B. L. Seckman, D. O. Scanlon, P. I. Djurovich, M. E. Thompson, B. C. Melot, *Chem. Commun.* **2019**, *55*, 3164.
[257] J. Pal, A. Bhunia, S. Chakraborty, S. Manna, S. Das, A. Dewan, S. Datta, A. Nag, *J. Phys. Chem. C* **2018**, *122*, 10643.
[258] F. Jiang, D. Yang, Y. Jiang, T. Liu, X. Zhao, Y. Ming, B. Luo, F. Qin, J. Fan, H. Han, L. Zhang, Y. Zhou, *J. Am. Chem. Soc.* **2018**, *140*, 1019.
[259] Y. Peng, F. Li, Y. Wang, Y. Li, R. L. Z. Hoye, L. Feng, K. Xia, V. Pecunia, *Appl. Mater. Today* **2020**, *19*, 100637.

[260] C. C. Stoumpos, C. D. Malliakas, M. G. Kanatzidis, *Inorg. Chem.* **2013**, *52*, 9019.
[261] U. G. Jong, C. J. Yu, Y. H. Kye, *RSC Adv.* **2019**, *10*, 201.
[262] Y. Cai, W. Xie, H. Ding, Y. Chen, K. Thirumal, L. H. Wong, N. Mathews, S. G. Mhaisalkar, M. Sherburne, M. Asta, *Chem. Mater.* **2017**, *29*, 7740.
[263] S. Shao, J. Liu, G. Portale, H. H. Fang, G. R. Blake, G. H. ten Brink, L. J. A. Koster, M. A. Loi, *Adv. Energy Mater.* **2018**, *8*, 1702019.
[264] Y. Gao, Z. Wei, P. Yoo, E. Shi, M. Zeller, C. Zhu, P. Liao, L. Dou, *J. Am. Chem. Soc.* **2019**, *141*, 15577.
[265] L. Peng, W. Xie, *RSC Adv.* **2020**, *10*, 14679.
[266] C. Katan, N. Mercier, J. Even, *Chem. Rev.* **2019**, *119*, 3140.
[267] W. Lee, H. Li, A. B. Wong, D. Zhang, M. Lai, Y. Yu, Q. Kong, E. Lin, J. J. Urban, J. C. Grossman, P. Yang, *Proc. Natl. Acad. Sci. U. S. A.* **2017**, *114*, 8693.
[268] A. B. Wong, Y. Bekenstein, J. Kang, C. S. Kley, D. Kim, N. A. Gibson, D. Zhang, Y. Yu, S. R. Leone, L. W. Wang, A. P. Alivisatos, P. Yang, *Nano Lett.* **2018**, *18*, 2060.
[269] Q. Fan, G. V. Biesold-McGee, J. Ma, Q. Xu, S. Pan, J. Peng, Z. Lin, *Angew. Chem., Int. Ed.* **2020**, *59*, 1030; , *Angew. Chem.* **2020**, *132*, 1042.
[270] B. Liu, M. Long, M. Q. Cai, J. Yang, *J. Phys. D. Appl. Phys.* **2018**, *51*, 105101.
[271] T. Kawai, S. Shimanuki, *Phys. Status Solidi* **1993**, *177*, K43.
[272] K. M. McCall, C. C. Stoumpos, S. S. Kostina, M. G. Kanatzidis, B. W. Wessels, *Chem. Mater.* **2017**, *29*, 4129.
[273] K. Kundu, P. Acharyya, K. Maji, R. Sasmal, S. S. Agasti, K. Biswas, *Angew. Chem., Int. Ed.* **2020**, *59*, 13093; , *Angew. Chem.* **2020**, *132*, 13193.
[274] S. Rieger, B. J. Bohn, M. Döblinger, A. F. Richter, Y. Tong, K. Wang, P. Müller-Buschbaum, L. Polavarapu, L. Leppert, J. K. Stolarczyk, J. Feldmann, *Phys. Rev. B* **2019**, *100*, 201404(R).
[275] Z. Xiao, Y. Yan, *Adv. Energy Mater.* **2017**, *7*, 1701136.
[276] R. C. Kurchin, P. Gorai, T. Buonassisi, V. Stevanović, *Chem. Mater.* **2018**, *30*, 5583.
[277] Z. Xiao, W. Meng, J. Wang, Y. Yan, *ChemSusChem* **2016**, *9*, 2628.
[278] A. E. Maughan, A. M. Ganose, M. M. Bordelon, E. M. Miller, D. O. Scanlon, J. R. Neilson, *J. Am. Chem. Soc.* **2016**, *138*, 8453.
[279] R. E. Brandt, R. C. Kurchin, R. L. Z. Hoye, J. R. Poindexter, M. W. B. Wilson, S. Sulekar, F. Lenahan, P. X. T. Yen, V. Stevanović, J. C. Nino, M. G. Bawendi, T. Buonassisi, *J. Phys. Chem. Lett.* **2015**, *6*, 4297.
[280] I. Vázquez-Fernández, S. Mariotti, O. S. Hutter, M. Birkett, T. D. Veal, T. D. C. Hobson, L. J. Phillips, L. Danos, P. K. Nayak, H. J. Snaith, W. Xie, M. P. Sherburne, M. Asta, K. Durose, *Chem. Mater.* **2020**, *32*, 6676.
[281] M. N. Saha, *J. Astrophys. Astron.* **1994**, *15*, 203.
[282] R. L. Z. Hoye, R. E. Brandt, A. Osherov, V. Stevanovic, S. D. Stranks, M. W. B. Wilson, H. Kim, A. J. Akey, J. D. Perkins, R. C. Kurchin, J. R. Poindexter, E. N. Wang, M. G. Bawendi, V. Bulovic, T. Buonassisi, *Chem. - Eur. J.* **2016**, *22*, 2605.
[283] Y. Zhou, L. Wang, S. Chen, S. Qin, X. Liu, J. Chen, D. J. Xue, M. Luo, Y. Cao, Y. Cheng, E. H. Sargent, J. Tang, *Nat. Photonics* **2015**, *9*, 409.
[284] R. E. Williams, Q. M. Ramasse, K. P. McKenna, L. J. Phillips, P. J. Yates, O. S. Hutter, K. Durose, J. D. Major, B. G. Mendis, *ACS Appl. Mater. Interfaces* **2020**, *12*, 21730.
[285] C. N. Savory, D. O. Scanlon, *J. Mater. Chem. A* **2019**, *7*, 10739.
[286] X. G. Zhao, D. Yang, J. C. Ren, Y. Sun, Z. Xiao, L. Zhang, *Joule* **2018**, *2*, 1662.
[287] C. N. Savory, A. Walsh, D. O. Scanlon, *ACS Energy Lett.* **2016**, *1*, 949.
[288] B. A. Connor, R. I. Biega, L. Leppert, H. I. Karunadasa, *Chem. Sci.* **2020**, *11*, 7708.
[289] B. A. Connor, L. Leppert, M. D. Smith, J. B. Neaton, H. I. Karunadasa, *J. Am. Chem. Soc.* **2018**, *140*, 5235.
[290] S. Nagane, D. Ghosh, R. L. Z. Hoye, B. Zhao, S. Ahmad, A. B. Walker, M. S. Islam, S. Ogale, A. Sadhanala, *J. Phys. Chem. C* **2018**, *122*, 5940.
[291] R. D. Shannon, *Acta Crystallogr.* **1976**, *A32*, 751.
[292] W. Travis, E. N. K. Glover, H. Bronstein, D. O. Scanlon, R. G. Palgrave, *Chem. Sci.* **2016**, *7*, 4548.
[293] B. Lee, C. C. Stoumpos, N. Zhou, F. Hao, C. Malliakas, C. Y. Yeh, T. J. Marks, M. G. Kanatzidis, R. P. H. Chang, *J. Am. Chem. Soc.* **2014**, *136*, 15379.
[294] Y.-T. Huang, S. R. Kavanagh, D. O. Scanlon, A. Walsh, R. L. Z. Hoye, *Nanotechnology* **2021**, *32*, 132004.
[295] S. Heo, G. Seo, Y. Lee, D. Lee, M. Seol, J. Lee, J. B. Park, K. Kim, D. J. Yun, Y. S. Kim, J. K. Shin, T. K. Ahn, M. K. Nazeeruddin, *Energy Environ. Sci.* **2017**, *10*, 1128.
[296] J. R. Poindexter, R. L. Z. Hoye, L. Nienhaus, R. C. Kurchin, A. E. Morishige, E. E. Looney, A. Osherov, J.-P. Correa-Baena, B. Lai, V. Bulović, V. Stevanović, M. G. Bawendi, T. Buonassisi, *ACS Nano* **2017**, *11*, 7101.
[297] M. H. Du, *J. Mater. Chem. A* **2014**, *2*, 9091.
[298] S. Kim, J. A. Márquez, T. Unold, A. Walsh, *Energy Environ. Sci.* **2020**, *13*, 1481.
[299] B. Das, I. Aguilera, U. Rau, T. Kirchartz, *Phys. Rev. Mater.* **2020**, *4*, 024602.
[300] R. L. Z. Hoye, L. C. Lee, R. C. Kurchin, T. N. Huq, K. H. L. Zhang, M. Sponseller, L. Nienhaus, R. E. Brandt, J. Jean, J. A. Polizzotti, A. Kursumović, M. G. Bawendi, V. Bulović, V. Stevanović, T. Buonassisi, J. L. MacManus-Driscoll, *Adv. Mater.* **2017**, *29*, 1702176.
[301] T. N. Huq, L. C. Lee, L. Eyre, W. Li, R. A. Jagt, C. Kim, S. Fearn, V. Pecunia, F. Deschler, J. L. MacManus-Driscoll, R. L. Z. Hoye, *Adv. Funct. Mater.* **2020**, *30*, 1909983.
[302] A. M. Ganose, S. Matsumoto, J. Buckeridge, D. O. Scanlon, *Chem. Mater.* **2018**, *30*, 3827.
[303] J. Kim, C. H. Chung, K. H. Hong, *Phys. Chem. Chem. Phys.* **2016**, *18*, 27143.
[304] E. P. Yao, Z. Yang, L. Meng, P. Sun, S. Dong, Y. Yang, Y. Yang, *Adv. Mater.* **2017**, *29*, 1606859.
[305] X. Zheng, Y. Hou, H. T. Sun, O. F. Mohammed, E. H. Sargent, O. M. Bakr, *J. Phys. Chem. Lett.* **2019**, *10*, 2629.
[306] H. Shi, M. H. Du, *Phys. Rev. B* **2014**, *90*, 174103.
[307] A. Zakutayev, C. M. Caskey, A. N. Fioretti, D. S. Ginley, J. Vidal, V. Stevanovic, E. Tea, S. Lany, *J. Phys. Chem. Lett.* **2014**, *5*, 1117.
[308] H. Shi, W. Ming, M. H. Du, *Phys. Rev. B* **2016**, *93*, 104108.
[309] S. Kim, J. S. Park, S. N. Hood, A. Walsh, *J. Mater. Chem. A* **2019**, *7*, 2686.
[310] Z. Xiao, H. Lei, X. Zhang, Y. Zhou, H. Hosono, T. Kamiya, *Bull. Chem. Soc. Jpn.* **2015**, *88*, 1250.
[311] Z. Xiao, Y. Zhou, H. Hosono, T. Kamiya, *Phys. Chem. Chem. Phys.* **2015**, *17*, 18900.
[312] M. Chen, M. G. Ju, A. D. Carl, Y. Zong, R. L. Grimm, J. Gu, X. C. Zeng, Y. Zhou, N. P. Padture, *Joule* **2018**, *2*, 558.
[313] S. S. Bhosale, A. K. Kharade, E. Jokar, A. Fathi, S. M. Chang, E. W. G. Diau, *J. Am. Chem. Soc.* **2019**, *141*, 20434.
[314] H. Lei, G. Yang, Y. Guo, L. Xiong, P. Qin, X. Dai, X. Zheng, W. Ke, H. Tao, Z. Chen, B. Li, G. Fang, *Phys. Chem. Chem. Phys.* **2016**, *18*, 16436.
[315] X. Wang, R. Tang, Y. Yin, H. Ju, S. Li, C. Zhu, T. Chen, *Sol. Energy Mater. Sol. Cells* **2019**, *189*, 5.
[316] F. Li, Y. Wang, K. Xia, R. L. Z. Hoye, V. Pecunia, *J. Mater. Chem. A* **2020**, *8*, 4396.
[317] F. Bai, Y. Hu, Y. Hu, T. Qiu, X. Miao, S. Zhang, *Sol. Energy Mater. Sol. Cells* **2018**, *184*, 15.
[318] A. Intaniwet, C. A. Mills, P. J. Sellin, M. Shkunov, J. L. Keddie, *ACS Appl. Mater. Interfaces* **2010**, *2*, 1692.
[319] J. Gu, G. Yan, Y. Lian, Q. Mu, H. Jin, Z. Zhang, Z. Deng, Y. Peng, *RSC Adv.* **2018**, *8*, 25802.

[320] R. L. Z. Hoye, B. Ehrler, M. L. Böhm, D. Muñoz-Rojas, R. M. Altamimi, A. Y. Alyamani, Y. Vaynzof, A. Sadhanala, G. Ercolano, N. C. Greenham, R. H. Friend, J. L. MacManus-Driscoll, K. P. Musselman, *Adv. Energy Mater.* **2014**, *4*, 1301544.
[321] L. Xiong, Y. Guo, J. Wen, H. Liu, G. Yang, P. Qin, G. Fang, *Adv. Funct. Mater.* **2018**, *28*, 1802757.
[322] M. Napari, T. N. Huq, R. L. Z. Hoye, J. L. MacManus-Driscoll, *InfoMat* **2020**, *Early View*, https://doi.org/10.1002/inf2.12146.
[323] E. Jokar, C. H. Chien, C. M. Tsai, A. Fathi, E. W. G. Diau, *Adv. Mater.* **2019**, *31*, 1804835.
[324] D. H. Cao, C. C. Stoumpos, T. Yokoyama, J. L. Logsdon, T. Bin Song, O. K. Farha, M. R. Wasielewski, J. T. Hupp, M. G. Kanatzidis, *ACS Energy Lett.* **2017**, *2*, 982.
[325] M. Chen, M. G. Ju, H. F. Garces, A. D. Carl, L. K. Ono, Z. Hawash, Y. Zhang, T. Shen, Y. Qi, R. L. Grimm, D. Pacifici, X. C. Zeng, Y. Zhou, N. P. Padture, *Nat. Commun.* **2019**, *10*, 16.
[326] B. Lee, A. Krenselewski, S. Il Baik, D. N. Seidman, R. P. H. Chang, *Sustainable Energy Fuels* **2017**, *1*, 710.
[327] X. Jiang, F. Wang, Q. Wei, H. Li, Y. Shang, W. Zhou, C. Wang, P. Cheng, Q. Chen, L. Chen, Z. Ning, *Nat. Commun.* **2020**, *11*, 1245.
[328] I. Kopacic, B. Friesenbichler, S. F. Hoefler, B. Kunert, H. Plank, T. Rath, G. Trimmel, *ACS Appl. Energy Mater.* **2018**, *1*, 343.
[329] A. H. Slavney, L. Leppert, D. Bartesaghi, A. Gold-Parker, M. F. Toney, T. J. Savenije, J. B. Neaton, H. I. Karunadasa, *J. Am. Chem. Soc.* **2017**, *139*, 5015.
[330] X. Yang, Y. Chen, P. Liu, H. Xiang, W. Wang, R. Ran, W. Zhou, Z. Shao, *Adv. Funct. Mater.* **2020**, *30*, 2001557.
[331] C. Wu, Q. Zhang, G. Liu, Z. Zhang, D. Wang, B. Qu, Z. Chen, L. Xiao, *Adv. Energy Mater.* **2020**, *10*, 1902496.
[332] S. M. Jain, D. Phuyal, M. L. Davies, M. Li, B. Philippe, C. De Castro, Z. Qiu, J. Kim, T. Watson, W. C. Tsoi, O. Karis, H. Rensmo, G. Boschloo, T. Edvinsson, J. R. Durrant, *Nano Energy* **2018**, *49*, 614.
[333] P. Karuppuswamy, K. M. Boopathi, A. Mohapatra, H. C. Chen, K. T. Wong, P. C. Wang, C. W. Chu, *Nano Energy* **2018**, *45*, 330.
[334] W. Ke, C. C. Stoumpos, M. G. Kanatzidis, *Adv. Mater.* **2019**, *31*, 1803230.
[335] Y. Liao, H. Liu, W. Zhou, D. Yang, Y. Shang, Z. Shi, B. Li, X. Jiang, L. Zhang, L. N. Quan, R. Quintero-Bermudez, B. R. Sutherland, Q. Mi, E. H. Sargent, Z. Ning, *J. Am. Chem. Soc.* **2017**, *139*, 6693.
[336] A. Z. Chen, J. J. Choi, *J. Vac. Sci. Technol. A* **2020**, *38*, 010801.
[337] R. Kondrotas, C. Chen, J. Tang, *Joule* **2018**, *2*, 857.
[338] R. A. Jagt, T. N. Huq, K. M. Börsig, D. Sauven, L. C. Lee, J. L. MacManus-Driscoll, R. L. Z. Hoye, *J. Mater. Chem. C* **2020**, *8*, 10791.
[339] H. Zhang, S. Yuan, H. Deng, M. Ishaq, X. Yang, T. Hou, U. A. Shah, H. Song, J. Tang, *Prog. Photovoltaics Res. Appl.* **2020**, *28*, 823.
[340] X. Wen, C. Chen, S. Lu, K. Li, R. Kondrotas, Y. Zhao, W. Chen, L. Gao, C. Wang, J. Zhang, G. Niu, J. Tang, *Nat. Commun.* **2018**, *9*, 2179.
[341] Z. Li, X. Liang, G. Li, H. Liu, H. Zhang, J. Guo, J. Chen, K. Shen, X. San, W. Yu, R. E. I. Schropp, Y. Mai, *Nat. Commun.* **2019**, *10*, 125.
[342] J. Zhang, Y. Yang, H. Deng, U. Farooq, X. Yang, J. Khan, J. Tang, H. Song, *ACS Nano* **2017**, *11*, 9294.
[343] M. Leng, Y. Yang, K. Zeng, Z. Chen, Z. Tan, S. Li, J. Li, B. Xu, D. Li, M. P. Hautzinger, Y. Fu, T. Zhai, L. Xu, G. Niu, S. Jin, J. Tang, *Adv. Funct. Mater.* **2018**, *28*, 1704446.
[344] M. Leng, Z. Chen, Y. Yang, Z. Li, K. Zeng, K. Li, G. Niu, Y. He, Q. Zhou, J. Tang, *Angew. Chem Int. Ed.* **2016**, *55*, 15012; , *Angew. Chem.* **2016**, *128*, 15236.
[345] Z. Ma, Z. Shi, D. Yang, F. Zhang, S. Li, L. Wang, D. Wu, Y. Zhang, G. Na, L. Zhang, X. Li, Y. Zhang, C. Shan, *ACS Energy Lett.* **2020**, *5*, 385.
[346] W. Chu, Q. Zheng, O. V. Prezhdo, J. Zhao, W. A. Saidi, *Sci. Adv.* **2020**, *6*, eaaw7453.
[347] S. Kim, A. Walsh, **2020**, axXiv: 2003.05394.
[348] W. Chu, Q. Zheng, O. V. Prezhdo, J. Zhao, W. A. Saidi, **2020**, arXiv: 2004.12559.
[349] K. Li, C. Chen, S. Lu, C. Wang, S. Wang, Y. Lu, J. Tang, *Adv. Mater.* **2019**, *31*, 1903914.
[350] P. Y. Yu, M. Cardona, in *Fundamentals of Semiconductors: Physics and Materials Properties*, Springer, Berlin, Heidelberg **1996**, pp. 107–158.
[351] M. Sendner, P. K. Nayak, D. A. Egger, S. Beck, C. Müller, B. Epding, W. Kowalsky, L. Kronik, H. J. Snaith, A. Pucci, R. Lovrinčić, *Mater. Horiz.* **2016**, *3*, 613.
[352] G. D. Mahan, *Many-Particle Physics*, Springer, Boston, MA **2000**.
[353] K. S. Song, R. T. Williams, *Self-Trapped Excitons*, Springer, Berlin **1993**.
[354] A. S. Ioselevich, E. I. Rashba, in *Quantum Tunnelling in Condensed Media* (Eds: Y. Kagan, A. J. Leggett), Elsevier, New York **1992**, pp. 347–425.
[355] C. W. M. Timmermans, G. Blasse, *Phys. Status Solidi* **1981**, *106*, 647.
[356] Z. Yang, X. Wang, Y. Chen, Z. Zheng, Z. Chen, W. Xu, W. Liu, Y. (M.) Yang, J. Zhao, T. Chen, H. Zhu, *Nat. Commun.* **2019**, *10*, 4540.
[357] T. Li, X. Chen, X. Wang, H. Lu, Y. Yan, M. C. Beard, D. B. Mitzi, *ACS Energy Lett.* **2020**, *5*, 347.
[358] S. Kahmann, E. K. Tekelenburg, H. Duim, M. E. Kamminga, M. A. Loi, *Nat. Commun.* **2020**, *11*, 2344.
[359] A. T. Lintereur, W. Qiu, J. C. Nino, J. Baciak, *Nucl. Instrum. Methods Phys. Res., Sect. A* **2011**, *652*, 166.
[360] J. Luo, X. Wang, S. Li, J. Liu, Y. Guo, G. Niu, L. Yao, Y. Fu, L. Gao, Q. Dong, C. Zhao, M. Leng, F. Ma, W. Liang, L. Wang, S. Jin, J. Han, L. Zhang, J. Etheridge, J. Wang, Y. Yan, E. H. Sargent, J. Tang, *Nature* **2018**, *563*, 541.
[361] J. D. Dow, D. Redfield, *Phys. Rev. B* **1972**, *5*, 594.
[362] Y. He, G. Galli, *Chem. Mater.* **2014**, *26*, 5394.
[363] Z. G. Yu, *J. Phys. Chem. Lett.* **2016**, *7*, 3078.
[364] A. Filippetti, A. Mattoni, C. Caddeo, M. I. Saba, P. Delugas, *Phys. Chem. Chem. Phys.* **2016**, *18*, 15352.
[365] R. W. Hellwarth, I. Biaggio, *Phys. Rev. B* **1999**, *60*, 299.
[366] H. Han, M. Hong, S. S. Gokhale, S. B. Sinnott, K. Jordan, J. E. Baciak, J. C. Nino, *J. Phys. Chem. C* **2014**, *118*, 3244.
[367] J. E. Baciak, Z. He, *IEEE Nucl. Sci. Symp. Med. Imaging Conf.* **2002**, *1*, 439.
[368] W. Pan, H. Wu, J. Luo, Z. Deng, C. Ge, C. Chen, X. Jiang, W. Yin, G. Niu, L. Zhu, L. Yin, Y. Zhou, Q. Xie, X. Ke, M. Sui, J. Tang, *Nat. Photonics* **2017**, *11*, 726.
[369] J. Lee, E. S. Koteles, M. O. Vassell, *Phys. Rev. B* **1986**, *33*, 5512.
[370] C. H. Henry, D. V. Lang, *Phys. Rev. B* **1977**, *15*, 989.
[371] S. Yakunin, B. M. Benin, Y. Shynkarenko, O. Nazarenko, M. I. Bodnarchuk, D. N. Dirin, C. Hofer, S. Cattaneo, M. V. Kovalenko, *Nat. Mater.* **2019**, *18*, 846.
[372] F. Ambrosio, J. Wiktor, F. De Angelis, A. Pasquarello, *Energy Environ. Sci.* **2018**, *11*, 101.
[373] N. Österbacka, P. Erhart, S. Falletta, A. Pasquarello, J. Wiktor, *Chem. Mater.* **2020**, *32*, 8393.
[374] A. Yangui, D. Garrot, J. S. Lauret, A. Lusson, G. Bouchez, E. Deleporte, S. Pillet, E. E. Bendeif, M. Castro, S. Triki, Y. Abid, K. Boukheddaden, *J. Phys. Chem. C* **2015**, *119*, 23638.
[375] M. Ueta, H. Kanzaki, K. Kobayashi, Y. Toyozawa, E. Hanamura, *Excitonic Processes in Solids*, Springer-Verlag, Berlin Heidelberg **1986**.
[376] B. Bin Yu, M. Liao, J. Yang, W. Chen, Y. Zhu, X. Zhang, T. Duan, W. Yao, S. H. Wei, Z. He, *J. Mater. Chem. A* **2019**, *7*, 8818.
[377] G. Longo, S. Mahesh, L. R. V. Buizza, A. D. Wright, A. J. Ramadan, M. Abdi-Jalebi, P. K. Nayak, L. M. Herz, H. J. Snaith, *ACS Energy Lett.* **2020**, *5*, 2200.
[378] P. A. Mante, C. C. Stoumpos, M. G. Kanatzidis, A. Yartsev, *Nat. Commun.* **2017**, *8*, 14398.
[379] M. D. Smith, H. I. Karunadasa, *Acc. Chem. Res.* **2018**, *51*, 619.
[380] Z. Tan, J. Li, C. Zhang, Z. Li, Q. Hu, Z. Xiao, T. Kamiya, H. Hosono, G. Niu, E. Lifshitz, Y. Cheng, J. Tang, *Adv. Funct. Mater.* **2018**, *28*, 1801131.
[381] R. Hofstadter, *Phys. Rev.* **1949**, *75*, 796.

[382] Y. Peng, T. N. Huq, J. Mei, L. Portilla, R. A. Jagt, L. G. Occhipinti, J. L. MacManus-Driscoll, R. L. Z. Hoye, V. Pecunia, *Adv. Energy Mater.* **2021**, *11*, 2002761.
[383] S. M. Menke, N. A. Ran, G. C. Bazan, R. H. Friend, *Joule* **2018**, *2*, 25.
[384] S. J. Zelewski, J. M. Urban, A. Surrente, D. K. Maude, A. Kuc, L. Schade, R. D. Johnson, M. Dollmann, P. K. Nayak, H. J. Snaith, P. Radaelli, R. Kudrawiec, R. Nicholas, P. Plochocka, M. Baranowski, *J. Mater. Chem. C* **2019**, *7*, 8350.
[385] T. Hu, M. D. Smith, E. R. Dohner, M. J. Sher, X. Wu, M. T. Trinh, A. Fisher, J. Corbett, X. Y. Zhu, H. I. Karunadasa, A. M. Lindenberg, *J. Phys. Chem. Lett.* **2016**, *7*, 2258.
[386] M. Ledinsky, T. Schönfeldová, J. Holovský, E. Aydin, Z. Hájková, L. Landová, N. Neyková, A. Fejfar, S. De Wolf, *J. Phys. Chem. Lett.* **2019**, *10*, 1368.
[387] M. Baranowski, S. J. Zelewski, M. Kepenekian, B. Traoré, J. M. Urban, A. Surrente, K. Galkowski, D. K. Maude, A. Kuc, E. P. Booker, R. Kudrawiec, S. D. Stranks, P. Plochocka, *ACS Energy Lett.* **2019**, *4*, 2386.
[388] C. Wehrenfennig, G. E. Eperon, M. B. Johnston, H. J. Snaith, L. M. Herz, *Adv. Mater.* **2014**, *26*, 1584.
[389] M. T. Weller, O. J. Weber, P. F. Henry, A. M. Di Pumpo, T. C. Hansen, *Chem. Commun.* **2015**, *51*, 4180.
[390] R. L. Milot, G. E. Eperon, H. J. Snaith, M. B. Johnston, L. M. Herz, *Adv. Funct. Mater.* **2015**, *25*, 6218.
[391] W. Rehman, R. L. Milot, G. E. Eperon, C. Wehrenfennig, J. L. Boland, H. J. Snaith, M. B. Johnston, L. M. Herz, *Adv. Mater.* **2015**, *27*, 7938.
[392] G. Maculan, A. D. Sheikh, A. L. Abdelhady, M. I. Saidaminov, M. A. Haque, B. Murali, E. Alarousu, O. F. Mohammed, T. Wu, O. M. Bakr, *J. Phys. Chem. Lett.* **2015**, *6*, 3781.
[393] D. M. Trots, S. V. Myagkota, *J. Phys. Chem. Solids* **2008**, *69*, 2520.
[394] F. Thouin, S. Neutzner, D. Cortecchia, V. A. Dragomir, C. Soci, T. Salim, Y. M. Lam, R. Leonelli, A. Petrozza, A. R. S. Kandada, C. Silva, *Phys. Rev. Mater.* **2018**, *2*, 034001.
[395] Y. Q. Zhao, Q. R. Ma, B. Liu, Z. L. Yu, J. Yang, M. Q. Cai, *Nanoscale* **2018**, *10*, 8677.
[396] X. Li, W. Ke, B. Traoré, P. Guo, I. Hadar, M. Kepenekian, J. Even, C. Katan, C. C. Stoumpos, R. D. Schaller, M. G. Kanatzidis, *J. Am. Chem. Soc.* **2019**, *141*, 12880.
[397] I. Chung, J. H. Song, J. Im, J. Androulakis, C. D. Malliakas, H. Li, A. J. Freeman, J. T. Kenney, M. G. Kanatzidis, *J. Am. Chem. Soc.* **2012**, *134*, 8579.
[398] K. P. Marshall, M. Walker, R. I. Walton, R. A. Hatton, *Nat. Energy* **2016**, *1*, 16178.
[399] Z. Chen, C. Yu, K. Shum, J. J. Wang, W. Pfenninger, N. Vockic, J. Midgley, J. T. Kenney, *J. Lumin.* **2012**, *132*, 345.
[400] J. Feng, B. Xiao, *J. Phys. Chem. C* **2014**, *118*, 19655.
[401] F. Hao, C. C. Stoumpos, D. H. Cao, R. P. H. Chang, M. G. Kanatzidis, *Nat. Photonics* **2014**, *8*, 489.
[402] W. Ke, C. C. Stoumpos, I. Spanopoulos, L. Mao, M. Chen, M. R. Wasielewski, M. G. Kanatzidis, *J. Am. Chem. Soc.* **2017**, *139*, 14800.
[403] P. Umari, E. Mosconi, F. De Angelis, *J. Phys. Chem. Lett.* **2018**, *9*, 620.
[404] R. L. Milot, M. T. Klug, C. L. Davies, Z. Wang, H. Kraus, H. J. Snaith, M. B. Johnston, L. M. Herz, *Adv. Mater.* **2018**, *30*, 1804506.
[405] T. Krishnamoorthy, H. Ding, C. Yan, W. L. Leong, T. Baikie, Z. Zhang, M. Sherburne, S. Li, M. Asta, N. Mathews, S. G. Mhaisalkar, *J. Mater. Chem. A* **2015**, *3*, 23829.
[406] X. Lu, Z. Zhao, K. Li, Z. Han, S. Wei, C. Guo, *RSC Adv.* **2016**, *6*, 86976.
[407] K. Nishimura, M. A. Kamarudin, D. Hirotani, K. Hamada, Q. Shen, S. Iikubo, T. Minemoto, K. Yoshino, S. Hayase, *Nano Energy* **2020**, *74*, 104858.
[408] R. L. Z. Hoye, L. Eyre, F. Wei, F. Brivio, A. Sadhanala, S. Sun, W. Li, K. H. L. Zhang, J. L. MacManus-driscoll, P. D. Bristowe, R. H. Friend, A. K. Cheetham, F. Deschler, *Adv. Mater. Interfaces* **2018**, *5*, 1800464.
[409] F. Wei, Z. Deng, S. Sun, N. T. P. Hartono, H. L. Seng, T. Buonassisi, P. D. Bristowe, A. K. Cheetham, *Chem. Commun.* **2019**, *55*, 3721.
[410] D. B. Mitzi, C. A. Feild, W. T. A. Harrison, A. M. Guloy, *Nature* **1994**, *369*, 467.
[411] D. B. Mitzi, *Chem. Mater.* **1996**, *8*, 791.
[412] C. R. Kagan, D. B. Mitzi, C. D. Dimitrakopoulos, *Science* **1999**, *286*, 945.
[413] T. Matsushima, S. Hwang, A. S. D. Sandanayaka, C. Qin, S. Terakawa, T. Fujihara, M. Yahiro, C. Adachi, *Adv. Mater.* **2016**, *28*, 10275.
[414] G. C. Papavassiliou, I. B. Koutselas, A. Terzis, M.-H. Whangbo, *Solid State Commun.* **1994**, *91*, 695.
[415] A. Singh, K. M. Boopathi, A. Mohapatra, Y. F. Chen, G. Li, C. W. Chu, *ACS Appl. Mater. Interfaces* **2018**, *10*, 2566.
[416] F. Umar, J. Zhang, Z. Jin, I. Muhammad, X. Yang, H. Deng, K. Jahangeer, Q. Hu, H. Song, J. Tang, *Adv. Opt. Mater.* **2019**, *7*, 1801368.
[417] S. Weber, T. Rath, K. Fellner, R. Fischer, R. Resel, B. Kunert, T. Dimopoulos, A. Steinegger, G. Trimmel, *ACS Appl. Energy Mater.* **2019**, *2*, 539.
[418] S. Sun, S. Tominaka, J. H. Lee, F. Xie, P. D. Bristowe, A. K. Cheetham, *APL Mater.* **2016**, *4*, 031101.
[419] W. A. Dunlap-Shohl, I. G. Hill, Y. Yan, D. B. Mitzi, *Chem. Mater.* **2018**, *30*, 8226.
[420] N. Ohno, M. Fujita, Y. Nakai, K. Nakamura, *Solid State Commun.* **1978**, *28*, 137.
[421] M. Kępińska, M. Nowak, P. Duka, M. Kotyczka-Morańska, P. Szperlich, *Opt. Mater.* **2011**, *33*, 1753.
[422] N. J. Podraza, W. Qiu, B. B. Hinojosa, H. Xu, M. A. Motyka, S. R. Phillpot, J. E. Baciak, S. Trolier-Mckinstry, J. C. Nino, *J. Appl. Phys.* **2013**, *114*, 033110.
[423] D. Tiwari, D. Alibhai, D. J. Fermin, *ACS Energy Lett.* **2018**, *3*, 1882.
[424] A. Owens, A. Peacock, *Nucl. Instruments Methods Phys. Res. Sect. A* **2004**, *531*, 18.
[425] M. Scholz, K. Oum, T. Lenzer, *Phys. Chem. Chem. Phys.* **2018**, *20*, 10677.
[426] Y. Kaifu, *J. Lumin.* **1988**, *42*, 61.
[427] W. W. Dai, Z. Y. Zhao, *Catalysts* **2016**, *6*, 133.
[428] Y. C. Choi, D. U. Lee, J. H. Noh, E. K. Kim, S. Il Seok, *Adv. Funct. Mater.* **2014**, *24*, 3587.
[429] A. D. DeAngelis, K. C. Kemp, N. Gaillard, K. S. Kim, *ACS Appl. Mater. Interfaces* **2016**, *8*, 8445.
[430] S. I. Beril, I. G. Stamov, A. V. Tiron, V. V. Zalamai, N. N. Syrbu, *Opt. Mater.* **2020**, *101*, 109737.
[431] C. Chen, D. C. Bobela, Y. Yang, S. Lu, K. Zeng, C. Ge, B. Yang, L. Gao, Y. Zhao, M. C. Beard, J. Tang, *Front. Optoelectron.* **2017**, *10*, 18.
[432] N. N. Syrbu, V. V. Zalamai, I. G. Stamov, S. I. Beril, *Beilstein J. Nanotechnol.* **2020**, *11*, 1045.
[433] O. S. Hutter, L. J. Phillips, K. Durose, J. D. Major, *Sol. Energy Mater. Sol. Cells* **2018**, *188*, 177.
[434] R. Nie, H. S. Yun, M. J. Paik, A. Mehta, B. W. Park, Y. C. Choi, S. Il Seok, *Adv. Energy Mater.* **2018**, *8*, 1701901.
[435] I. L. Markov, *Nature* **2014**, *512*, 147.
[436] K. T. Butler, J. M. Frost, A. Walsh, *Energy Environ. Sci.* **2015**, *8*, 838.
[437] D. Tiwari, F. Cardoso-Delgado, D. Alibhai, M. Mombrú, D. J. Fermín, *ACS Appl. Energy Mater.* **2019**, *2*, 3878.
[438] K. M. Boopathi, P. Karuppuswamy, A. Singh, C. Hanmandlu, L. Lin, S. A. Abbas, C. C. Chang, P. C. Wang, G. Li, C. W. Chu, *J. Mater. Chem. A* **2017**, *5*, 20843.
[439] B. Yang, Y. J. Li, Y. X. Tang, X. Mao, C. Luo, M. S. Wang, W. Q. Deng, K. L. Han, *J. Phys. Chem. Lett.* **2018**, *9*, 3087.
[440] D. Ju, X. Jiang, H. Xiao, X. Chen, X. Hu, X. Tao, *J. Mater. Chem. A* **2018**, *6*, 20753.
[441] Y. Li, K. Yang, *Energy Environ. Sci.* **2019**, *12*, 2233.

[442] V. F. MacHulin, F. V. Motsnyi, O. M. Smolanka, G. S. Svechnikov, E. Y. Peresh, *Low Temp. Phys.* **2004**, *30*, 964.
[443] M. Scholz, O. Flender, K. Oum, T. Lenzer, *J. Phys. Chem. C* **2017**, *121*, 12110.
[444] Z. Zhang, X. Li, X. Xia, Z. Wang, Z. Huang, B. Lei, Y. Gao, *J. Phys. Chem. Lett.* **2017**, *8*, 4300.
[445] B. Saparov, J. Sun, W. Meng, Z. Xiao, H. Duan, O. Gunawan, D. Shin, I. G. Hill, Y. Yan, D. B. Mitzi, *Chem. Mater.* **2016**, *28*, 2315.
[446] M. G. Ju, M. Chen, Y. Zhou, H. F. Garces, J. Dai, L. Ma, N. P. Padture, X. C. Zeng, *ACS Energy Lett.* **2018**, *3*, 297.
[447] J. Euvrard, X. Wang, T. Li, Y. Yan, D. B. Mitzi, *J. Mater. Chem. A* **2020**, *8*, 4049.
[448] B. W. Park, B. Philippe, X. Zhang, H. Rensmo, G. Boschloo, E. M. J. Johansson, *Adv. Mater.* **2015**, *27*, 6806.
[449] M. C. Weidman, M. Seitz, S. D. Stranks, W. A. Tisdale, *ACS Nano* **2016**, *10*, 7830.

Robert L. Z. Hoye is a lecturer (Assistant Professor) in the Department of Materials at Imperial College London. There, he also holds a Royal Academy of Engineering Research Fellowship. He completed his Ph.D. at the University of Cambridge (2012–2014), before working as a postdoctoral researcher at the Massachusetts Institute of Technology (2015–2016). He subsequently received two College Research Fellowships at Cambridge, first at Magdalene College (2016–2019), then at Downing College (2019–2020), before taking up his Lectureship at Imperial in 2020. His research focuses on defect-tolerant semiconductors, and their development into optoelectronic devices.

Juanita Hidalgo is currently a Ph.D. student and GAANN fellow at the School of Materials Science and Engineering at the Georgia Institute of Technology working in the group of Prof. Juan-Pablo Correa-Baena. She obtained her Bachelor of Science degree in Chemical Engineering in 2017 from Universidad de los Andes, Colombia. Her research interest focuses on X-ray and neutron scattering characterization techniques to understand the structure–property relationships in metal halide perovskites.

Robert A. Jagt is currently a Ph.D. student in the Department of Materials Science and Metallurgy at the University of Cambridge, where he is working with Prof. Driscoll and Dr. Hoye. He received his M.Sc. in Econometrics and Applied Physics from the University of Groningen in the Netherlands. He worked for a year with Prof. Julia Greer at the California Institute of Technology on nanolattices before pursuing a Ph.D. in the UK. His doctoral research focuses on the growth of next-generation thin films and single crystals and their applications in energy devices, including photovoltaics, photoelectrochemical cells, and radiation detectors.

Juan-Pablo Correa-Baena is an Assistant Professor and the Goizueta Junior Faculty Chair at the School of Materials Science and Engineering at Georgia Tech since January 2019. He pursued his Ph.D. in environmental engineering and materials science at the University of Connecticut, USA. He was a postdoctoral fellow at EPFL, Switzerland, and was awarded a Department of Energy postdoctoral fellowship to conduct his research at MIT, USA. His group focuses on the understanding and control of electronic dynamics at the nanoscale for low-cost semiconductors, such as halide perovskites.

Thomas Fix is a CNRS researcher in the ICube laboratory, University of Strasbourg—CNRS. His field is advanced concepts and innovative materials for optoelectronics and solar cells. He has been working on oxide perovskite thin films since 2003. Current research topics include novel oxides for photovoltaics, downconversion and downshifting for photovoltaics, and silicon clathrate films.

Judith L. MacManus-Driscoll is professor in Materials Science at the University of Cambridge, Royal Academy of Engineering Chair in Emerging Technologies, and visiting faculty at Los Alamos National Lab. She researches oxide thin film design for low energy electronics and energy materials applications.